UNIVERSITY OF SOUTHAMPTON

ENERGY TECHNOLOGY RESEARCH GROUP

School of Engineering Sciences

MULTIPHASE LATTICE BOLTZMANN SIMULATION OF MICROFLUIDICS

by

Ernesto Monaco

Thesis for the degree of Doctor of Philosophy

November 2009

A papa' ed a zia Rosa...perche' ne sareste stati felici

Ad Oli, welcome!

A Ci, e ho detto tutto...anzi no,

We can do it!

Abstract

Numerical simulation of multiphase flow often represents a challenging task for classical Computational Fluid Dynamics (CFD) schemes based on the macroscopic description of the fluid state (continuum hypothesis) leading to the Navier-Stokes equations. The reason lays in the fact that these flows are often driven by phenomena originating at meso- or micro-scales.

This dissertation concerns the lattice Boltzmann (LB) method and its applicability to multiphase liquid/liquid or liquid/gas system. This method derives from kinetic theory, which uses statistics to describe the fluid state. Although quite recently appeared, the LB method is attracting more and more attention essentially because its kinetic nature allows a simple incorporation of small scale physics without suffering from the computational penalties of Molecular Dynamics schemes. The algorithm, which consists essentially nodal relaxation (collision) and streaming along the links of a regular spaced lattice, is highly efficient and simple to parallelize; besides the LB equation does not present nonlinear convective terms. To deal with multiphase flows the Shan-Chen (SC) model has been adopted in this study. This approach is one of the most widely used because of its simplicity. The basic theory of LB as well as the description and some validation of the SC model are the main subjects of the first part of this dissertation.

The basic LB algorithm suffers of instabilities when applied to high-Reynolds flows; even the SC model is all but perfect: one of its most important defects consists in the very low density ratio achievable ($\mathcal{O}(10)$). The second part of this dissertation will therefore present an improved formulation of the basic SC model, based on some recently proposed strategies. For example the incorporation of different equations of state into the LB allows to increase the density ratio of one or two orders of magnitude, while a different formulation of the collision step (Multiple

Relaxation Times LB) allows to overcome the stability issues at low-viscous flows. This improved SC model is finally applied to simulate binary droplet collisions. The results are compared with experiments and show a very good qualitative agreement.

Acknowledgements

There are many people that deserve my deepest gratitude. First of all my supervisor, Professor Kai H. Luo, for having given me this opportunity and most of all for having been constantly supportive, available and patient with me. I will always be grateful for that. Working in the Energy Technology Group at Southampton University gave me the chance to meet many talented researchers: the discussions we have had provided me a lot of interesting ideas that I hope I will have the chance to develop in the next future. I think most of all of my second supervisor, Professor Frank Walsh and of Dr. Akeel Shah: the first also for giving me a very interesting book on Electrochemistry, while the second also for spending with me a wonderful day in Cambridge sharing ideas about fuel cells and lattice Boltzmann.

If my staying in Southampton had been so pleasant it was most of all because of some wonderful people that I now have the privilege of calling friends: Dario (you know!), Matteo and his fiancee Teresa, Giuliano, Jun and his lovely wife, Raul (my lattice Boltzmann fellow!) and Andreas. Our Fridays at the Crown Inn have been fantastic moments to relax from the stress of hard work week. I really hope wherever life will bring us we will always keep in touch. This thesis is yours as well. Cheers!

My family, from my mother Maria Luisa to my fantastic sisters Maria Giulia and Marianna has always been close to me. Father, I know you would have been proud of this. Thank you all! Now it comes the hardest part: finding the right words to express my love and gratitude to my wonderful wife, Mariafrancesca, is above my (small) literary talent. Ci, your love, patience, constant support and encouragement even in the hardest moments made all this possible. You made my life better, you still make it better everyday. Maybe it is trivial, but it is the truth. Thank you.

Finally, the practical support of EPSRC under the Grant No. EP/EO11640/1 is gratefully acknowledged.

Contents

List of Figures

List of Tables

Lyst of Symbols

Acronymus

BC Boundary condition.

CFD Computational Fluid Dynamics.

CFL Courant-Fredrick-Levy number.

CS Carnahan-Starling equation of state.

DVM Discrete Velocity Models.

ELB Entropic Lattice Boltzmann.

EOS Equation of State.

FHP-I 6-speeds two-dimensional lattice.

FHP-I Frisch-Hasslacher-Pomeau lattice (6 speeds).

LB Lattice Boltzmann Method.

LBGK Lattice Boltzmann with Bathangar-Groos-Krook collision operator.

LGCA Lattice Gas Cellular Automata.

MD Molecular Dynamics.

ModBBK Modified Bounce Back scheme.

MSL Multi-speed lattice.

NS Navier-Stokes equations.

PR Peng-Robinson equation of state.

RK Redlich-Kwong equation of state.

RKS Redlich-Kwong equation of state with correction by Soave.

SC Shan-Chen multiphase lattice Boltzmann.

TRT Two-Relaxation-Time scheme.

vdW van der Waals equation of state.

ZH BC developed by Zou and He for pressure and velocity boundaries.

Physical constants

k Thermal conductivity.

k_B Boltzmann constant.

N_A Avogadro's constant, 6.022141×10^{23} mol^{-1}.

R_0 Universal gas constant.

Greek Symbols

$\Pi^{(1)}_{\alpha\beta}$ Viscous stress tensor.

$\alpha, \beta, \gamma, \delta$ Cartesian components of vector fields.

$\boldsymbol{\varrho}$ Vector of moments.

$\boldsymbol{\xi}_i$ Speed of i-th particle.

χ^j Mass fraction of fluid j.

δ Artificial compressibility.

Δt Time step.

Δx Lattice space.

λ Characteristic collision time.

μ Shear viscosity.

ν Kinematic shear viscosity.

Ω Control Computational volume.

ω Relaxation frequency.

ω_A Acentric factor.

Ω_i Collision operator.

$\partial\Omega$ Boundary of the control/computational volume.

Φ Dissipation function.

ϕ Collisional invariant.

$\Pi^{(0)}_{\alpha\beta}$ Inviscid momentum flux tensor.

ψ Effective mass in Shan-Chen model.

ρ Fluid density.

ρ_R Reduced density.

σ Surface tension.

τ Relaxation time .

ε Perturbation parameter in Chapman-Enskog expansion.

ε_{mix} Mixing efficiency.

ζ Bulk viscosity.

Non-dimensional numbers

Kn Knudsen number.

We Weber number.

Ma Mach number.

Pe Peclet number.

Re Reynolds number.

Roman Letters

$\mathbf{u}$ Macroscopic velocity.

$\mathcal{L}$ Lattice model.

S_{ij} Scattering matrix.

$E_{\gamma\delta}$ Strain rate tensor.

$g^A_{\alpha\beta}$ Aymmetric part of velocity gradient tensor.

$g^S_{\alpha\beta}$ Symmetric part of velocity gradient tensor.

$g_{\alpha\beta}$ Velocity gradient tensor.

$L^{DkQb}_{\alpha_1\alpha_2\ldots\alpha_n}$ Lattice tensor of n-th rank.

$\bar{\mathbf{u}}, \bar{u_x}, \bar{u_y}, \bar{u_z}$ Velocity vector and components for analytical solutions.

$\mathbb{H}$ H-function.

$\mathbb{M}^b$ b-dimensional vector space based on discrete velocity moments of $\{f_i\}$.

$\mathbb{V}^b$ b-dimensional vector space based on lattice vectors.

$\mathbf{e}_i$ Lattice vectors.

$\mathbf{j}$ Macroscopic momentum.

$\mathbf{k}$ Wave vector.

$\mathbf{L}$ Evolution operator for linearized LBE in Fourier space.

$\mathbf{q}$ Thermal flux.

$\mathbf{R}_I$ Position of I-th macromolecule.

$\mathbf{r}_i$ Position of i-th particle.

$\mathbf{U_0}$ Relative speed between two colliding droplets.

$\mathbf{v}_i$ Generic base vector in the moment space $\mathbb{M}^b$.

$\mathcal{B}$ Boundary condition operator.

B Impact factor.

C Collision operator.

c Lattice speed.

c_s Lattice speed of sound.

D_c Cavity aspect ratio.

d_p Molecular diameter.

D_{12} Diffusivity for fluids 1 and 2 system.

f Single-particle distribution function.

f^{eq} Equilibrium particle distribution function.

f_i Probability distribution function on the i-th lattice direction.

f_N N-particles probability distribution function.

G Pressure gradient.

h Discrete H-function.

$J(f, f)$ Simplified collision operator.

L_m Channel length required for complete diffusive mixing.

L_{hydro} Characteristic macroscopic lenght scale.

L_{mfp} Mean molecular free path.

m_i Molecular mass.

M_I Total mass of I-th macromolecule.

N Number of particles/molecules.

n_i Occupation functions in LGCA method.

N_R Total number of macromolecules.

p Fluid pressure.

$p^\star$ Nonideal part of lattice Boltzmann EOS.

p_R Reduced pressure.

R_1, R_2 Radii of colliding droplets.

t Time .

t_C Mixing time by convection.

t_D Mixing time by diffusion.

T_R Reduced temperature.

V_{ij} Pair-wise intermolecular potential.

w_i Lattice weighting factor.

z_α Eigenvalues of evolution operator for linearized LBE in Fourier space.

D Number of space dimensions.

E Total specific energy.

Chapter 1

Introduction

This thesis is devoted to the presentation of a numerical scheme known as the Lattice Boltzmann Method (LB), and to the demonstration of its performance with special emphasis on multiphase flow problems.

The LB is quite a recent numerical approach, since it dates back to the late eighties. To properly introduce this method and, at the same time, to better underline the differences between LB and classic Computational Fluid Dynamics (CFD) solvers, it is worthwhile to remember the different possible ways to describe the state of a complex physical system. The first approach consists of expressing the state of the system by means of a number of observable, and therefore measurable, properties. According to statistical mechanics, such an approach is referred to as *coarse-grained*, *observational* or *macroscopic* [11]. Considering a fluid, it is clear that this approach corresponds to he continuum hypothesis: in this case the state of the fluid is completely specified in terms of extensive quantities like density, momentum and total energy. Treating the fluid as a continuum means these quantities can be considered as functions of spatial coordinates and time, smoothly varying on the whole extension of the system. A *conservation equation* can be written for everyone of these quantities, to describe its rate of change due to fluxes across the frontier of the domain occupied by the fluid, and due to productions inside the domain. This set of equations is universally known as *Navier-Stokes equations* (NS). The NS are second order, partial differential equations, nonlinear in the convection term, and rarely an analytic solution can be obtained: often, even finding a numerical

one may prove to be a difficult task. Many of the difficulties encountered are just caused by the nonlinearity; a linear model should be, if existing, very welcomed. But, since that nonlinearity is in turn caused by the way the convection term is modeled in the framework of the continuum hypothesis, it is clear that getting rid of the macroscopic approach must be the first step in the search for a *linear* model.

An alternative approach considers the system as a collection of N discrete elements: the state of the whole system at any time t is determined once the state of any single element is known. Adopting again the terminology of statistical mechanics, this description is referred to as *fine-grained*, *dynamical*, or *microscopic* [11]. One question immediately arises: how can the microscopic configuration of the system be evaluated? The first idea is to track the trajectory of every single molecule i of mass m_i, considered point-wise, by means of Newtonian mechanics: it is possible to assume as state variables the space coordinates and the speed components ($\mathbf{r}_i$ and $\boldsymbol{\xi}_i$), and thus it is necessary to integrate a set of fN ordinary second order differential equations (with proper initial and boundary conditions), f being the number of degrees of freedom of every molecule:

$$m_i \frac{d^2\mathbf{r}_i}{dt^2} = \mathbf{F}_i \tag{1.1a}$$

$$\mathbf{r}_i(t=0) = \mathbf{r}_{0i} \tag{1.1b}$$

$$\boldsymbol{\xi}_i(t=0) = \boldsymbol{\xi}_{0i} \tag{1.1c}$$

In (1.1a) the right-hand side represents the force acting upon the considered molecule because of intermolecular interactions. Considering a fN-dimensional space the microscopic, or "dynamic", state of the system can be expressed by a point in such space, referred to as *Phase Space*. Often, instead of this Newtonian description, an equivalent *Hamiltonian* one can be adopted, which proves to be more suitable to describe systems having complex not mono-atomic molecules that possess even rotational degrees of freedom. The main drawback of such kind of description consists in the excessive computational cost, which is above the capabilities of any available computer since even a small volume of fluid contains an enormous amount of molecules. In order to reduce that cost consists in introducing "pseudoparticles" or "macromolecules", each representing a huge number, say R, of real ones. For

such a simplified system, equation (1.1a) can be written as:

$$M_I \frac{d^2 \mathbf{R}_I}{dt^2} = \mathbf{F}_I + \mathbf{D}_I, \; I = 1, .., N_R, \tag{1.2}$$

where $\mathbf{R}_I$ represents a coarse-grained coordinate, $M_I = \sum_{i=1}^{R} m_i$ is the total mass of the I-th macromolecule, and $N_R << N_A$ is the total number of macromolecules. The term $\mathbf{D}_I$ models all the details of the underlying finer scales. A further approximation could consist in getting rid of this last term, and solve the (1.1a), applied to a limited number of molecules: this is the basic idea of *molecular dynamics* (MD). If the objective is to simulate macroscopic physics, the model is still full of unnecessary microscopic details included in the right-hand side of (1.2), making molecular dynamics a computational tool which is suitable only for very small time and length scales.

Another approach to describe the microscopic configuration of a fluid is, according to Kinetic theory, to employ probability distribution functions: the microscopic configuration is described by means of statistics. These functions evolve according to very complex "transport" equations, the most famous being the Boltzmann's equation. Kinetic theory aims to build a bridge between the molecular and the macroscopic worlds, rather than to deal with macroscopic dynamics: in fact, NS can be recovered from the aforementioned Boltzmann equation, once it is solved: unfortunately, this is a non-linear integral-differential equation, very complicated to integrate either analytically or numerically.

So far, it does not seem to be possible to find a model simpler than NS, but able to simulate macroscopic fluid dynamics. Both Newtonian and kinetic descriptions have been showed to lead to very complex models: that is essentially due to the fact they are full of microscopic details: one could wonder whether such detail is truly necessary. What if one should think of targeting the macroscopic description, by means of a *fictitious* microscopic one? Such a model should be totally unsuitable to effectively represent the real microscopic behaviour of a fluid, but nevertheless, if correctly implemented, could be suitable to represent the macroscopic one. It could be sufficient just to ask the model to ensure isotropy, conservation of mass, momentum and energy, respect the second law of thermodynamics (irreversibility), and to preserve the rheological nature (Newtonian, non-Newtonian, Bingham) of the considered fluid. Such an approach could seem quite strange, but has its foundation in

the consideration, due to Gibbs, that the same microscopic state, say A, corresponds to a *set* of microscopic configurations that it is not possible to observe, called the *dynamic image of A*, which, in turn, implies an accurate microscopic description is not necessary to obtain an accurate macroscopic one.

The Lattice Gas Cellular Automata (LGCA) can be derived from the above idea. The phase-space is completely discretized in such a method: fictitious particles stream and collide on a fixed lattice. These fictitious particles can stream with only a small number of velocities, instead of the infinite ones characterizing their real counterparts. Each velocity is associated with one direction in the lattice model considered. The name of this method reveals the fact that it belongs to a class of models, named *Cellular Automata*. These models appeared for the first time in the early fifties, thanks to S. Ulam and J. Von Neumann. Their distinctive feature is that all the state variables are discrete, and are updated by means of simple evolutionary rules, usually local: thus, they are perfect candidates for massively parallel computations. Nevertheless their simplicity, the Cellular Automata have been demonstrated to be able of modelling very complex systems. The LGCA (and LB) also belongs to the family of the so-called *Discrete Velocity Models* (DVM), because of the limited number of velocities allowed. Because of its parallel nature, the absence of round-off error, the ease in handling complicated geometries, a great enthusiasm rapidly grew up about LGCA in the mid-eighties; unfortunately, it was later frustrated by the emerging of a series of pitfalls that annihilated all its potential advantages, as it will be shown later. The LB took off just as the cure for such drawbacks, through a series of successive evolutions. After more than a decade, although many issues still needs to be addressed, it can certainly be said that LB has emerged as a valid alternative to classic CFD tools in many applications, and there are problems, including pore scale modeling or multiphase flows with sharp interfaces, where it could be defined as the best choice. Besides, its kinetic nature makes it very promising for microfluidic applications, that are often characterized by forces having their origin on a microscale like electrochemical interactions.

1.1 Outline of the thesis

Chapter 2 summarizes the continuum approach and the kinetic theory. In Chapter 3, the LB is presented, starting from its ancestor, the LGCA; the second part of the chapter deals with the linearized LB with discretized Bathangar-Gross-Krook collision operator (LBGK), currently the most used and simplest LB implementation; finally the modelling of boundaries within the LB framework is discussed. Simple two-dimensional channel flow and lid-driven cavity cases are adopted as validation. The multiphase/multicomponent Shan-Chen (SC) LB is presented in its basic form in Chapter 4, together with different test cases. In Chapter 5 the *Multiple Relaxation Times LB* (MRT-LB) is presented as solution that increases the stability of LB at high Reynolds numbers and shows its potential by extending the lid-driven cavity case. Chapter 6 is concerned with some improvements of the SC model that have been proposed in the last years; the improved SC scheme is applied in Chapter 7 to the binary droplet collision case at different geometries. Finally, conclusions and directions for future work are discussed in Chapter 8.

Chapter 2

Two Different Approaches

In this chapter the two different ways of describing the state of a fluid, according to continuum hypothesis and kinetic theory, will be presented. These two approaches lead respectively to the Navier-Stokes and the Boltzmann equation. The Navier-Stokes equation can be recovered from the Boltzmann equation via a perturbative technique referred to as the Chapman-Enskog expansion. Before presenting the details of these two approaches it is important to remark that the continuum hypothesis cannot always be applied, while the kinetic description always holds: if, and only if, the smallest macroscopic characteristic length scale, L_{hydro} (for instance the diameter of a pipe) is much greater than the largest microscopic characteristic length scale, that is the molecular mean free path, L_{mfp}, the continuum approximation is reasonable, because the measured values of intensive and extensive quantities do not depend on microscopic fluctuations.

2.1 Navier-Stokes Equations

A control volume Ω, fixed, or translating with constant velocity, in an inertial reference frame is considered; having defined $\partial\Omega$ as its boundary, dS is an elementary surface, part of the boundary, identified by the normal vector $\mathbf{n}$ pointing outside the volume. The Navier Stokes equations represent how the three observable extensive quantities specifying the fluid state (namely density, momentum and energy) vary with time because of fluxes across $\partial\Omega$ and productions inside Ω. To derive these

equations just the Gauss' theorem for a vector field $\mathbf{A}$, in a D dimensional space, and the Reynolds transport theorem for a scalar field B, are necessary:

$$\int_\Omega \nabla \cdot \mathbf{A} d\Omega = \int_{\partial\Omega} \mathbf{A} \cdot \mathbf{n} dS \tag{2.1a}$$

$$\frac{d}{dt}\int_\Omega B d\Omega = \int_{\partial\Omega} \left(\frac{\partial B}{\partial t} + \nabla \cdot (B\mathbf{u}) \right) dS \tag{2.1b}$$

in these equations, $\mathbf{u}(\mathbf{x}, t)$ is the macroscopic velocity field. Unless otherwise reported, greek letters like $\alpha, \beta, \gamma, \delta$ are used to indicate Cartesian components of vectorial fields like velocities or gradients, while $\partial_\alpha = \frac{\partial}{\partial x_\alpha}$. Here, and in what follows, the Einstein convention for summation over repeated indexes in a D-dimensional space has been applied[1]. If a fluid with no viscous dissipation is considered, the conservation equations are named *Euler equations* and can be written, in their local formulation, as:

$$\partial_t \rho + \rho \partial_\alpha u_\alpha = 0 \tag{2.2a}$$

$$\partial_t (\rho u_\alpha) = -\partial_\beta \Pi^{(0)}_{\alpha\beta} \qquad \alpha, \beta = 1 \dots D \tag{2.2b}$$

$$\rho \partial_t E + \rho u_\alpha \partial_\alpha E = -\partial_\alpha (p u_\alpha) \tag{2.2c}$$

where ρ is the density, $E = \left(e + \frac{u^2}{2} \right)$ is the total specific energy, composed by internal and kinetic contributions, and $\Pi^{(0)}_{\alpha\beta}$, represents the *inviscid momentum flux tensor*, defined by:

$$\Pi^{(0)}_{\alpha\beta} = p\delta_{\alpha\beta} + \rho u_\alpha u_\beta. \tag{2.3}$$

This tensor represents the flux of α-th component across the elementary surface having β as normal vector. Equations (2.2a)-(2.2c) are written in Eulerian form. A Lagrangian representation is also possible.

Real fluids are, of course, viscid, and thus the flux tensor has to be modified to take into account stresses due to shear and compression. Because of random molecular motion, faster molecules migrating into regions occupied by slower molecules

[1] $X_\alpha Y_\alpha = \sum_{\alpha=1}^{D} X_\alpha Y_\alpha$.

give them part of their momentum. That *diffusive* momentum flux tends to accelerate slower fluid regions and to decelerate faster ones, and, for a *Newtonian* fluid, is related to the the strain rate, by the following relation:

$$\Pi^{(1)}_{\alpha\beta} = -\widetilde{\mu}_{\alpha\beta\gamma\delta} E_{\gamma\delta}, \tag{2.4}$$

where $\Pi^{(1)}_{\alpha\beta}$ is the *viscous stress tensor*, and $E_{\gamma\delta}$ is the *strain rate tensor*. The 4-th order tensor $\widetilde{\mu}_{\alpha\beta\gamma\delta}$ relating the aforementioned quantities has to be an isotropic tensor, because (2.4) must be invariant under any rotation or translation of the reference frame. The most general form for such kind of tensors is:

$$\widetilde{\mu}_{\alpha\beta\gamma\delta} = A\delta_{\alpha\beta}\delta_{\gamma\delta} + B\delta_{\alpha\gamma}\delta_{\beta\delta} + C\delta_{\alpha\delta}\delta_{\beta\gamma}. \tag{2.5}$$

More details concerning tensor isotropy can be found in Appendix A. The strain rate tensor depends on the velocity gradient one, $g_{\alpha\beta} = \partial_\beta u_\alpha$, that can be decomposed into a symmetrical and an asymmetrical term, as follows:

$$g_{\alpha\beta} = g^S_{\alpha\beta} + g^A_{\alpha\beta} = \frac{1}{2}\left(g_{\alpha\beta} + g_{\beta\alpha}\right) + \frac{1}{2}\left(g_{\alpha\beta} - g_{\beta\alpha}\right). \tag{2.6}$$

Only the symmetric part, $g^S_{\alpha\beta}$, is responsible for deformation, while the asymmetrical part $g^A_{\alpha\beta}$ accounts for rigid rotations. The final form of strain rate tensor is, therefore:

$$E_{\alpha\beta} = 2g^S_{\alpha\beta} = \partial_\alpha u_\beta + \partial_\beta u_\alpha. \tag{2.7}$$

Inserting equations (2.7) and (2.5) into (2.4) and defining respectively the shear viscosity as $\mu = B + C$ and the bulk viscosity as $\zeta = 2A$, the so-called *viscous stress tensor* can be written as:

$$\Pi^{(1)}_{\alpha\beta} = -\mu\left(\partial_\alpha u_\beta + \partial_\beta u_\alpha\right) - \zeta\partial_\gamma u_\gamma \delta_{\alpha\beta}. \tag{2.8}$$

It is possible now to express the total momentum flux tensor for a viscous fluid:

$$\Pi_{\alpha\beta} = \Pi^{(0)}_{\alpha\beta} + \Pi^{(1)}_{\alpha\beta}, \tag{2.9}$$

and the momentum balance equation as:

$$\partial_t(\rho u_\alpha) = -\partial_\beta \Pi_{\alpha\beta}. \tag{2.10}$$

The substitution of equations (2.2b) and (2.8) into (2.10) allows to write the momentum balance equation for a *compressible* fluid as follows:

$$\partial_t \rho u_\alpha + \partial_\beta \rho u_\alpha u_\beta = -\partial_\alpha p + \mu \left(\partial_\alpha u_\beta + \partial_\beta u_\alpha\right) + \zeta \partial_\gamma u_\gamma \delta_{\alpha\beta}. \tag{2.11}$$

The conservation equation for total specific energy can be written as:

$$\rho \partial_t E + \rho u_\alpha \partial_\alpha E = -\partial_\alpha (p u_\alpha) + \partial_\alpha (k \left(\partial_\alpha T\right)) + \Phi, \tag{2.12}$$

where the linear phenomenological relation that links thermal flux $\mathbf{q}$ to temperature gradient $\boldsymbol{\nabla} T$ by means of thermal conductivity k has been employed: $q_\alpha = -k\partial_\alpha T$; the first term in the right-hand side represent the reversible work due to compression, while Φ is the so-called *dissipation function*, measuring the rate at which mechanical energy is irreversibly dissipated into thermal one:

$$\Phi = \left(\mu - \zeta \frac{2}{D}\right) \partial_\alpha^2 u_\alpha + \frac{1}{2} \mu \left(\partial_\alpha u_\beta + \partial_\beta u_\alpha\right)^2. \tag{2.13}$$

To close the system of (2.2a), (2.11) and (2.12) the particular kind of fluid has to be specified, by means of an *equations of state* (EOS) : in the case of a perfect gas, for instance, it is possible to write $p = \rho m R_0 T$, where R_0 is the universal gas constant. In (2.11) and (2.12) the transport coefficients μ, ζ and k depend on density, pressure and especially on temperature; if such dependence is negligible the coefficients can be treated as constants, allowing to simplify the NS equations. If the fluid can be considered as *incompressible*the system of equations can be written as:

$$\partial_\alpha u_\alpha = 0 \tag{2.14a}$$

$$\partial_t u_\alpha + u_\beta \partial_\beta u_\alpha = -\frac{1}{\rho} \partial_\alpha p + \nu \partial_\alpha^2 u_\alpha \tag{2.14b}$$

$$\rho \partial_t E + \rho u_\alpha \partial_\alpha E = \mu \left(\partial_\alpha u_\beta + \partial_\beta u_\alpha\right) \partial_\beta u_\alpha + \partial_\alpha q_\alpha, \tag{2.14c}$$

where $\nu = \mu/\rho$ is the *kinematic shear viscosity*. For an incompressible fluid, taking the divergence of the (2.14b), leads to the following elliptic *Poisson* equation,

which can be used to eliminate the pressure from the set of equations:

$$\partial_\alpha^2 p = -\rho \partial_\beta u_\alpha \partial_\alpha u_\beta. \tag{2.15}$$

Navier-Stokes equations have almost all the symmetries of Newtonian mechanics, thus they possess invariance under continuous spacial-temporal translations, arbitrary three-dimensional rotations (isotropy), and Galilean transformations. Because of viscous dissipation, they do not possess invariance under time reversions. Previously it has been showed that the isotropy of NS lays in the form of the viscous momentum flux tensor (see (2.7)). The requisite of Galilean invariance, instead, determines the form of the nonlinear convective term: the factor multiplying the momentum convective flux has to equal one [1].

2.2 Kinetic Theory

According to Kinetic theory, the fluid is seen as discrete, composed by a number N of molecules, each moving according to Newtonian mechanics laws. Since the number of degrees of freedom for such a system is in the order of Avogadro's constant N_A it makes no sense trying to determine the trajectory of any individual molecule. Kinetic theory is not interested in describing the evolution of single molecules, but the *collective* behaviour of the system by means of statistics. The idea is to consider a collection of identical K systems having N particles, let them start from the same initial condition and observe the outcomes, in this case the molecular configurations, of every try. Then it is possible to define a *N-particles probability distribution function* (N-PDF) as $f_N(\mathbf{x}_1, \mathbf{x}_2, \cdots, \mathbf{x}_N, \boldsymbol{\xi}_1, \boldsymbol{\xi}_2, \cdots, \boldsymbol{\xi}_N, t)$ as indicating the relative number of systems that, at time t, exhibits a configuration in which particle 1 occupies position $\mathbf{x}_1$ with microscopic velocity $\boldsymbol{\xi}_1$, particle 2 occupies position $\mathbf{x}_2$ with microscopic velocity $\boldsymbol{\xi}_2$, and so on. The f_N is said to contain the *full* statistics of the whole system [12]. For such function, applying the Liouville theorem, it is possible to write a transport equation in the form:

$$\frac{Df}{Dt} = \partial_t f + \boldsymbol{\xi} \cdot \nabla f = \Omega(f, f), \tag{2.16}$$

where $\Omega(f, f)$ is a collision operator. Said M a generic integer in the interval

$[1, N]$, it is possible to define an *M-particles probability distribution function* (M-PDF) f_M, which is related to the f_N by the following relation:

$$f_M\left(\mathbf{x}_1, \cdots, \mathbf{x}_M, \boldsymbol{\xi}_1, \cdots, \boldsymbol{\xi}_M, t\right) = \\ = \int f_N(\mathbf{x}_1, \cdots, \mathbf{x}_N, \boldsymbol{\xi}_1, \cdots, \boldsymbol{\xi}_N, t) d\mathbf{x}_{M+1} \cdots d\mathbf{x}_N d\boldsymbol{\xi}_{M+1} \cdots, d\boldsymbol{\xi}_N \quad (2.17)$$

Definition (2.17) allows to write a hierarchy of equations for f_N (*Liouville equation*, $f_{N-1} \ldots f_1$ (the Boltzmann equation). The first equation of this hierarchy, which is referred to as BBGKY after Bogoliuibov, Born, Green, Kirkwood and Yvon derived it independently (for more details, see [13]) is given by:

$$\frac{\partial f_N}{\partial t} + \sum_i^N \left[\dot{\mathbf{x}}_i \cdot \frac{\partial f_N}{\partial \mathbf{x}_i} + \dot{\mathbf{p}}_i \cdot \frac{\partial f_N}{\partial \mathbf{p}_i} \right] = 0. \quad (2.18)$$

In equation (2.19) the following substitution has been performed:

$$\dot{\mathbf{p}}_i = - \sum_{j=1, j\neq i}^N \frac{\partial V_{ij}}{\partial \mathbf{x}_i}, \quad (2.19)$$

where $V_{ij} = V_{ij}||\mathbf{x}_i - \mathbf{x}_j||$ is the pair-wise intermolecular potential. The whole hierarchy can be expressed by a general transport equation for the generic f_M:

$$\frac{\partial f_M}{\partial t} + \sum_i^M \dot{\mathbf{x}}_i \cdot \frac{\partial f_M}{\partial \mathbf{x}_i} - \sum_{i,j=1, i\neq j}^M \frac{\partial V_{ij}}{\partial \mathbf{x}_i} \cdot \frac{\partial f_M}{\partial \mathbf{p}_i} = (N-M) \int d\mathbf{x}_{M+1} d\boldsymbol{\xi}_{M+1} \frac{\partial V_{iM+1}}{\partial \mathbf{r}_i} \cdot \left(\frac{\partial f_{M+1}}{\partial \mathbf{p}_i} - \frac{\partial f_{M+1}}{\partial \mathbf{p}_{M+1}} \right). \quad (2.20)$$

Equation (2.20) corresponds to a hierarchy of integral-differential equations called the BBGKY hierarchy, after . Going down on the hierarchy it is possible to write the transport equation for a single-particle PDF f , the Boltzmann equation. This equation, which Ludwig Boltzmann derived in 1872, is particularly significant, because macroscopic quantities can be recovered as momenta of a single-particle PDF:

- Density

$$\rho(\mathbf{x},t) = m \int f(\mathbf{x},\boldsymbol{\xi},t) d\mathbf{v} \tag{2.21}$$

- Momentum

$$\rho(\mathbf{x},t)\mathbf{u}(\mathbf{x},t) = m \int \boldsymbol{\xi} f(\mathbf{x},\boldsymbol{\xi},t) d\boldsymbol{\xi} \tag{2.22}$$

- Temperature

$$T(\mathbf{x},t) = \frac{m}{3nk_B} \int (\boldsymbol{\xi} - \mathbf{u}) \cdot (\boldsymbol{\xi} - \mathbf{u})\, f(\mathbf{x},\boldsymbol{\xi},t) d\boldsymbol{\xi}. \tag{2.23}$$

2.2.1 The Boltzmann Equation and the H-Theorem

The Boltzmann equation is concerned with the one-particle distribution function f. This distribution function completely describes the state of the particle, and the only two causes for its variation are the application of an external force field and the collisions,

$$\frac{\partial f}{\partial t} + \boldsymbol{\xi} \cdot \frac{\partial f}{\partial \mathbf{x}} + \mathbf{F} \cdot \frac{\partial f}{\partial \boldsymbol{\xi}} = \Omega(f,f), \tag{2.24}$$

in which the first two terms represents the *Lagrangian derivative* of f, with the third term representing the effect of an external force term $\mathbf{F}$ inducing an acceleration $\mathbf{a}$; on the right-hand side of (2.24) appears the *Collision operator*. More details about its derivation can be found, for instance, in [13]. Here it is worth recalling that the assumptions upon which that equation is based. Molecules are considered as hard spheres. The collision term can be initially expressed by means of two-particle distribution function $f_2(\mathbf{x}_1, \mathbf{x}_2, \boldsymbol{\xi}_1, \boldsymbol{\xi}_2, t)$, expressing the probability of finding, at time t, two molecules having relative distance and velocities suitable to collide. Given N monoatomic molecules having diameter d_p the *Boltzmann-Grad limit* prescribes that $N \to \infty$ and $d_p \to 0$, so that the quantity Nd_p^2 tends to a finite value. The density is low, making acceptable the hypothesis of two-body collisions. Most importantly, the chaos assumption (*Stossanslauz*), means the state of the two molecules *going to collide* is not correlated. That last assumption implies that the two events "particle 1 in position $\mathbf{x}_1$ with velocity $\boldsymbol{\xi}_1$" and "particle 2 in position $\mathbf{x}_2$ with velocity $\boldsymbol{\xi}_2$",

are *statistically independent*: thus, f_2 can be expressed as product of single-particle distribution functions f_1:

$$f_2(\mathbf{x}_1, \mathbf{x}_2, \boldsymbol{\xi}_1, \boldsymbol{\xi}_2, t) = f_1(\mathbf{x}_1, \boldsymbol{\xi}_1, t) f_1(\mathbf{x}_2, \boldsymbol{\xi}_2, t). \tag{2.25}$$

The collision is considered as a totally elastic process. Two molecules are obviously correlated after having experienced a collision, but for an extremely limited time. The resulting final form of the collision operator is:

$$\Omega(f, f) = \int_{R^3} \int_{S^+} \mid \mathbf{V} \cdot \mathbf{n} \mid [f(\mathbf{x}_1, \xi_{\mathbf{1}}') f(\mathbf{x}_1, \xi_{\mathbf{2}}') - f(\mathbf{x}_1, \xi_{\mathbf{1}}) f(\mathbf{x}_1, \boldsymbol{\xi}_2)] d\mathbf{n} d\xi_{\mathbf{2}}, \tag{2.26}$$

having defined $\boldsymbol{\xi_1}$ and $\boldsymbol{\xi_2}$ respectively as the post-collisional velocities of two particles, and corresponding pre-collisional ones by primes, while $\mathbf{V} = \boldsymbol{\xi}_1 - \boldsymbol{\xi}_2$. The integration is taken over the whole three dimensional vectorial space of velocities and over the hemisphere S^+ including all the directions so that the particles are moving away from each other after the collision. One could be interested in searching functions ϕ so that the following equality holds:

$$\int_{R^3} \phi(\boldsymbol{\xi}) \Omega(f, f) d\boldsymbol{\xi} = 0. \tag{2.27}$$

It can be demonstrated that such a ϕ (called *collisional invariant*) can only have the following form:

$$\phi(\boldsymbol{\xi}) = a + \mathbf{b} \cdot \boldsymbol{\xi} + c \mid \boldsymbol{\xi} \mid^2. \tag{2.28}$$

Besides, the following *Boltzmann inequality* holds:

$$\int \Omega(f, f) \ln f \; d\boldsymbol{\xi} \leq 0. \tag{2.29}$$

In (2.29) the equal sign applies if $\ln f$ is a collision invariant. In that last case, it is possible to write:

$$f = \exp(a + \mathbf{b} \cdot \boldsymbol{\xi} + c \mid \boldsymbol{\xi} \mid^2) \tag{2.30}$$

which is known as a *Maxwellian distribution*, and represents an equilibrium status for density ρ_0 and temperature T_0. Probably the following form is more familiar:

$$f^{eq} = \frac{\rho}{m}\left(\frac{m}{2\pi k_B T}\right)^{3/2} exp\left(\frac{-m(\boldsymbol{\xi}-\mathbf{u})\cdot(\boldsymbol{\xi}-\mathbf{u})}{2k_B T}\right) \tag{2.31}$$

where k_B is the Boltzmann constant and m is the molecular mass. It is important to note that f^{eq} depends on the particle position $\mathbf{x}$ only implicitly via the local values of macroscopic quantities. Defining the so-called *H-function*:

$$\mathbb{H} = \int f \ln f \; d\boldsymbol{\xi}, \tag{2.32}$$

it is possible to demonstrate by using (2.27) that $\mathbb{H}$ is a monotonically decreasing function of time, $d\mathbb{H}(t)/dt \leq 0$. This is the Boltzmann's *local* H-Theorem. The H-function is bounded from below, and this bound corresponds to the value related to an equilibrium state, when f is a Maxwellian distribution. A *global* H-Theorem, for the whole system, can be derived as well. This is analog of the second law of thermodynamics, if $\mathbb{H}$ is identified with the negative of specific entropy divided by the Boltzmann's constant. Interested readers can refer to [12] to find out demonstrations of this theorem. Once solved the (2.24), macroscopic hydrodynamics equations can be recovered, together with the transport coefficients expressed as functions of microscopic quantities. The main problem is represented by the complex form of $\Omega(f, f)$ (2.26). In order to tackle this issue simplified forms of the collision operator have been proposed in the past, justified by the consideration that the large amount of details in the two-body interaction contained into (2.26) is not likely to have a significant influence on observable flow quantities. Of course there are two constraints the generic simplified collision operator $J(f, f)$ must satisfy:

- Conservation of the collisional invariants of $\Omega(f, f)$.
- Existance of an H-theorem.

Both these constraints are fulfilled by the most popular of these simplified operators, which was proposed by Bhatnagar, Gross and Krook [14] and is therefore referred to as the BGK operator. The idea behind this formulation is that each collision modified f by an amount proportional to its departure from the local Maxwellian distribution define by equation (2.31):

$$J(f,f) = -\frac{1}{\lambda}\left[f - f^{(0)}\right] \tag{2.33}$$

where λ is a characteristic collision time. The final form of the Boltzmann equation with BGK collision operator is therefore given by:

$$\frac{\partial f}{\partial t} + \boldsymbol{\xi}\cdot\frac{\partial f}{\partial \mathbf{x}} + \mathbf{F}\cdot\frac{\partial f}{\partial \boldsymbol{\xi}} = -\frac{1}{\lambda}\left[f - f^{(0)}\right]. \tag{2.34}$$

2.2.2 Recovering Macroscopic Hydrodynamics

The Chapman-Enskog expansion is a way to solve the Boltzmann equation by means of an asymptotic perturbation technique. This section is intended to give a brief summary of the procedure; the whole expansion can be found for instance in [13]. For the sake of simplicity the external force term is not considere here. Besides the BGK formulation for the collision operator is adopted. Equation (2.34) can be expressed in non-dimensional form as [1]:

$$\partial_t f + \boldsymbol{\xi}\cdot\nabla f = -\frac{1}{\varepsilon\lambda}\left[f - f^{(0)}\right], \qquad \varepsilon = Kn = \frac{L_{\text{mfp}}}{L_{\text{hydro}}}. \tag{2.35}$$

In (2.35) the perturbation parameter, ε, corresponds to the Knudsen number Kn , which represents the ratio between the characteristic lenght scale of the macroscopic flow that is being considered L_{hydro} and the mean molecular free path L_{mfp} . The normal solution of (2.35) depends on local microscopic quantities according to:

$$f(\mathbf{x},\boldsymbol{\xi},t) = f(\mathbf{x},\boldsymbol{\xi};\rho,\mathbf{u},T). \tag{2.36}$$

It is possible to write the distribution functions expanding them in terms of ε:

$$f = \sum_{n=0}^{\infty}\varepsilon^n f^{(n)}, \tag{2.37}$$

where the following constraints hold:

$$\int d\boldsymbol{\xi} f^{(0)} \begin{bmatrix} 1 \\ \boldsymbol{\xi} \\ (\boldsymbol{\xi}-\mathbf{u})^2 \end{bmatrix} = \rho \begin{bmatrix} 1 \\ \mathbf{u} \\ D\theta \end{bmatrix} \tag{2.38a}$$

$$\int d\boldsymbol{\xi} f^{(1)} \begin{bmatrix} 1 \\ \boldsymbol{\xi} \\ (\boldsymbol{\xi}-\mathbf{u})^2 \end{bmatrix} = 0, \tag{2.38b}$$

meaning that only the first order term contribute to determine the macroscopic quantities, mass, momentum and energy. The higher order terms contribute to the gradients of these quantities. The collision term can be expanded in a similar way:

$$\Omega(f, f^*) = \sum_{n=0}^{\infty} \varepsilon^n \Omega^{(n)}, \qquad \Omega^{(n)} = \sum_{k+l=n} \Omega(f^{(k)}, f_*^{(l)}). \tag{2.39}$$

The normal solution of Boltzmann equation can be obtained by solving the equations successively derived from (2.35) for the different terms of the expansion (2.37). The 0-th order solution is found out to correspond to the Maxwellian equilibrium distribution (2.31). The solution for the first order term $f^{(1)}$ is expressed by:

$$f^{(1)} = -\lambda(\partial_t f^{(0)} + \xi_\alpha \partial_\alpha f^{(0)}). \tag{2.40}$$

The macroscopic conservation equations can be finally obtained as moments of the Boltzmann equation with the normal solutions previously obtained:

$$\int d\boldsymbol{\xi}(\partial_t f + \boldsymbol{\xi} \cdot \nabla f) \begin{bmatrix} 1 \\ \boldsymbol{\xi} \\ \frac{1}{2}(\boldsymbol{\xi}-\mathbf{u})^2 \end{bmatrix} = 0. \tag{2.41}$$

Inserting in (2.41) only the 0-th order term of the expansion (2.37) leads to the Euler equations, while adding the first-order one leads to the Navier-Stokes equations.

Chapter 3

The Lattice Boltzmann Method

This chapter is dedicated to the presentation of the Lattice Boltzmann method (LB). Historically, the LB originated to cure the pitfalls of the Lattice Gas Cellular Automata (LGCA). Therefore the chapter will start with a description of this last method, underlying its merits and limitations: every of these drawbacks was addressed by successive improvements of LB, so the path leading from LGCA to the most commonly used LB, the single-relaxation time LB, will be described. The following section are devoted to introduce the different lattice models, to discuss the implementation and the accuracy of different kinds of boundary conditions, to illustrate how to scale back from lattice quantities to the corresponding physical ones. The last part of the chapter illustrates the performance of this basic LB implementation through some classical test cases.

3.1 The Lattice Gas and the birth of LB

Let us consider a discrete phase space in D dimensions defined by a regular lattice $\mathcal{L}$ univocally described by a set of b velocity vectors $\mathbf{e}_i|\{0, 1, \ldots, b-1\}$ connecting each lattice site to its neighbours. In two-dimensions an example of such a structure is given by the lattice possessing hexagonal symmetry ($b = 6$). On that lattice, termed $D2Q6$ model (meaning two-dimensional, six velocity model) or FHP-I model (after Frisch, Hasslacher and Pomeau, who first employed that model [15]), fictitious particles having identical mass $m = 1$ move according to the following set

of prescriptions:

- The particles can move only in the six prescribed directions defining the lattice, with velocity given by the corresponding $\mathbf{e}_i$.
- In a single time step all particles jump on the next neighbour node according to their speed. Either longer or shorter jumps are prohibited.
- There cannot be two particles at the same time on the same node moving toward the same node, therefore, at every time step, the single node can host a maximum of six particles having the six different speed allowed by the lattice (exclusion principle).

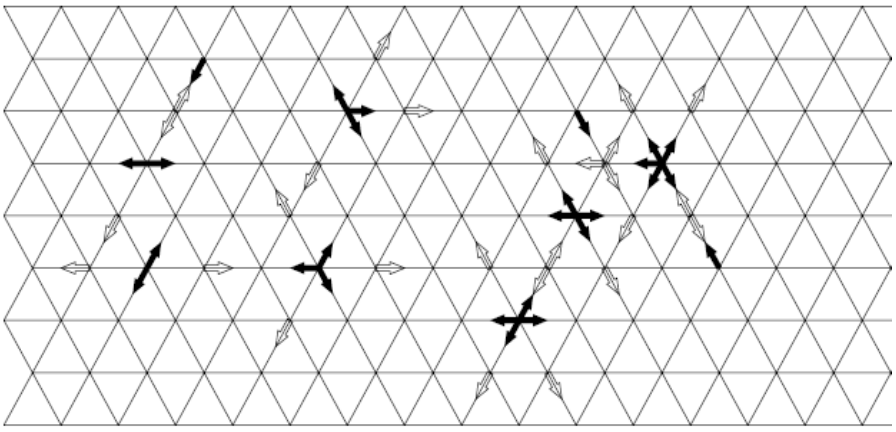

Figure 3.1: Lattice configuration for FHP-I model at two time steps: each arrow represent a particle momentum. The black arrows are related to time t, while the hollow ones to time $t+1$, after propagation and/or collision (from [1]).

Once fixed such prescriptions, the state of the system at any single lattice node can be completely specified by a sequence of zeros or ones, the values assumed by a set of six *occupation functions*, $n_i(\mathbf{x}, t)$, one for every lattice link. The i-th occupation function will be one at time t if the node hosts a particle traveling along the i-th link, and 0 otherwise: six bits are thus required to express the local state, while, with N the total number of lattice sites, expressing the global state of the

lattice requires $6N$ bits. This system is totally discrete, and belongs to the family of Cellular Automata. The evolutionary rules consist of two steps: propagation and collision, to mimic what the particles of a real fluid experience. During the propagation step, particles are synchronized in jumping to the next neighboring lattice according to their speed. The propagation operator, S, can be considered as a *shift*. Once reached their destination, particles redistribute their momentum along the different directions characterizing the lattice in the collision step. The collision operator $\Omega_i[\mathbf{n}]$ is local, and, whatever is its form, must conserve the local mass and momentum of the particles hosted on the site. To do that, considering the boolean nature of occupation functions, it is clear that this operator can just be equal to $[-1, 0, 1]$ [16]. Besides, the collision operator must satisfy the so-called *semi-detailed balance*, which simply means that one post-collisional state can correspond to a set of different pre-collisional states. This property introduces irreversibility into lattice gas dynamics. The aforementioned processes can be condensed in one equation only, the Lattice Gas Cellular Automata (LGCA) equation:

$$n_i\left(\mathbf{x} + \mathbf{e}_i\Delta t, t + \Delta t\right) - n_i\left(\mathbf{x}, t\right) = \Omega_i[\mathbf{n}], \qquad i = 0, \ldots, 5 \tag{3.1}$$

where $\mathbf{n} = (n_0(\mathbf{x}, t), \ldots, n_5(\mathbf{x}, t))^T$ is the vector of the occupation functions. In the following the index i will be referred to the different directions of $\mathcal{L}$ and the explicit reference to the extremes $0 \ldots b - 1$ will be omitted. The (3.1) can be considered as the lattice equivalent of the Boltzmann equation, (2.32), without forcing. It is clear that such an extremely simplified model fails in conveniently representing the complex dynamics of a real fluid at microscopic level: the phase-space is completely discretized meaning while real fluid particles can move freely in every direction, here they are forced to move on a fixed set of directions,and with a fixed set of speeds! Nevertheless our target is to obtain realistic *macroscopic* hydrodynamics and this representation can be adopted for that purpose, provided that $\mathcal{L}$ has enough geometric symmetries to allow the building of isotropic 4-th order tensors, as those present in NS (see (2.8)). This is not a trivial aspect, because not all the lattice models one may think of satisfy this requirement. The best example is the cross-shaped four speed termed HPP (after Hardy, Pazzis and Pomeau who defined it) for two-dimensional simulations: this was the first lattice-gas model ever developed but, as it is demonstrated in Appendix A, it failed in recovering the NS

equations. In the limit of low Mach numbers, a Chapman-Enskog expansion, similar to that presented in Chapter 2, allows to recover the NS equations. The LGCA attracted a lot of interest from the scientific community in the eighties, because of the following merits:

- The state of every single node can be described by just six bits, therefore the memory savings are consistent.
- The method works on boolean and integer quantities, therefore there is no round-off error and there is unconditional stability.
- The method is intrinsically parallel.
- Ease in dealing with complex geometries, thanks to the bounce-back boundary condition (described in a successive section).

Unfortunately, at the same time LGCA possesses severe drawbacks:

- High statistical noise, due to the Boolean nature of the occupation functions, forcing to perform averages on a big number of sites to have smooth hydrodynamic fields. That makes vain the memory savings previously mentioned.
- The collision operator is very complex, and its degree of complexity increases exponentially as more physics is added to the model (think of multiphase flows), or simply when three-dimensional problems are faced.
- The macroscopic equations obtained are not Galilean-invariant, and the pressure depends unphysically on velocity.
- The number of possible collisions allowed by the lattice is too small (see Figure 3.2), making impossible to reach high Reynolds numbers in the simulations (less collisions mean higher mean free path, which, in turns, means higher viscosity).

Despite many efforts, these defects could not be completely cured, until, in 1989 Mc Namara and Zanetti [17] solved the first of them, the high statistical noise: substituting the occupation functions with their averages, f_i , and adopting Boltzmann's chaos assumption (no particles correlation before collision) they wrote the real-value counterpart of (3.1), the first *Lattice-Boltzmann* equation:

$$f_i\left(\mathbf{x}+\mathbf{e}_i\Delta t, t+\Delta t\right) - f_i\left(\mathbf{x}, t\right) = \Omega_i[\mathbf{f}] \tag{3.2}$$

where this time $\mathbf{f} = (f_0(\mathbf{x},t), \ldots, f_5(\mathbf{x},t))$ is the vector of the averages relatedto the considered lattice node. These functions can be interpreted as the probability distribution functions (PDF) of the different particle populations moving on the lattice.

3.2 From LCGA to LBGK

The first obstacle was at the end overcome, but all the others still remained. The collision operator inherits all the properties of mass, momentum and energy conservation from its LGCA counterpart, including the semi-detailed balance. Having defined a local *discrete H-function* as $h = \sum_i f_i(\mathbf{x},t)\log(f_i(\mathbf{x},t))$, it can be demonstrated [18] that this lst property is a sufficient condition to satisfy the local (discrete) H-Theorem. As seen in the previous Chapter, this allows us to expand the distribution functions around the Maxwellian distribution. This consideration was used by Higuera and Jimenez [19], to simplify the collision operator: their idea was to use a *scattering matrix* S_{ij}, driving two-particle collisions only:

$$\Omega_i = \sum_j S_{ij}[f_j - f_j^{eq}]. \tag{3.3}$$

This simpler collision operator could be used in three-dimensional simulations. To address the final two pitfalls, it was necessary to take the idea of the lattice-gas to its extreme consequences: since that the only goal is reproducing realistic macroscopic hydrodynamics with an extremely simplified, and therefore fictitious, microscopic model, why one should depend on the "real" collisions of a model so far from being realistic? Higuera, Succi and Benzi [20] developed a new model by tuning the scattering matrix just on macroscopic hydrodynamics, getting rid of the limited collisionality of the underlying lattice. They achieved that goal relating the nonzero eigenvalues of S_{ij} to the transport coefficients (the kinematic viscosity, for instance, is directly controlled by the leading nonzero eigenvalue). The final step consisted in a further simplification, replacing the full scattering matrix with a diagonal form $S_{ij} = -\omega\delta_{ij}$ in which ω represents a *relaxation frequency* and its inverse τ a *relaxation*

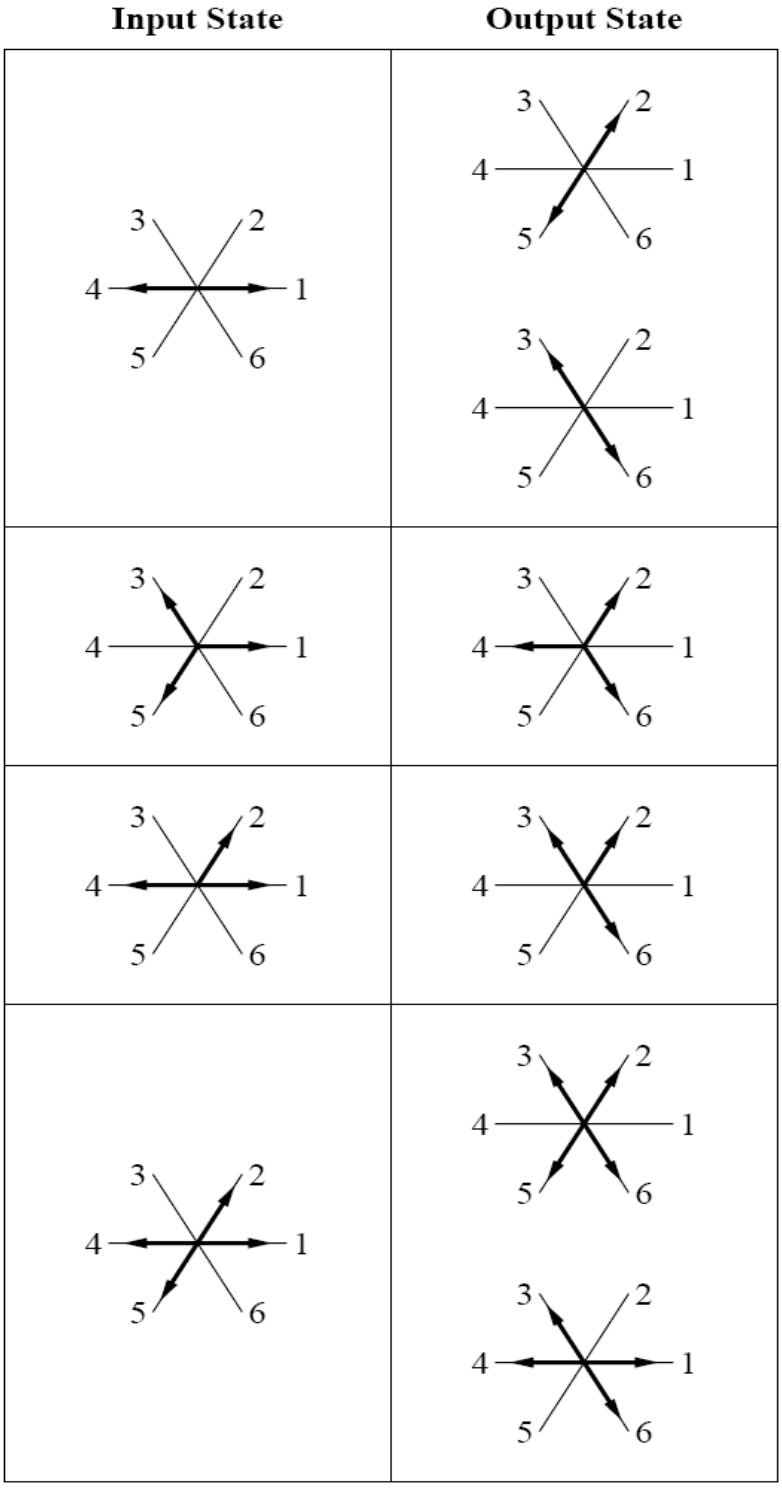

Figure 3.2: Collisions allowed by FHP-I model (From [1]). All the possible collision configurations have been reported, except for those leaving the state on the node unchanged and for those equivalent because of the lattice symmetry. The total mass and momentum have to be conserved by the collision operator. Two- and four-particles collisions are undeterministic, while three-particle ones are deterministic.

time. This formulation is therefore referred to as *Single Relaxation Time* LB (SRT). The final collision operator obtained is the lattice version of the already mentioned model proposed by Bathnagar, Gross and Krook (BGK), and the resulting Lattice Boltzmann is termed LBGK model:

$$f_i\left(\mathbf{x}+\mathbf{e}_i\Delta t, t+\Delta t\right) - f_i\left(\mathbf{x},t\right) = -\frac{1}{\tau}\left(f_i\left(\mathbf{x},t\right) - f_i^{eq}\left(\mathbf{x},t\right)\right). \tag{3.4}$$

In (3.4), Δt is the time step, expressed in physical units; $\Delta x = |\mathbf{e}_i|\Delta t$ is the distance between two consecutive lattice sites. The most general form of the equilibrium PDF, f_i^{eq}:

$$f_i^{eq} = A_i + B_i e_{i\alpha} u_\alpha + C_i u^2 + D_i e_{i\alpha} e_{i\beta} u_\alpha u_\beta + \mathcal{O}(u^3). \tag{3.5}$$

The constants A_i, B_i, C_i and D_i appearing in (3.5) are determined in order to recover the correct macroscopic fluid dynamics at inviscid level, that means the Euler equations. The constraints that the f_i^{eq} has to fulfill are:

$$\rho = \sum_i f_i^{eq} \tag{3.6a}$$

$$\rho u_\alpha = \sum_i f_i^{eq} e_{i\alpha} \tag{3.6b}$$

$$\Pi_{\alpha\beta}^{(0)} = \sum_i f_i^{eq} e_{i\alpha} e_{i\beta} = p\delta_{\alpha\beta} + \rho u_\alpha u_\beta. \tag{3.6c}$$

As stated in kinetic theory the viscous part of the stress tensor comes from the non-equilibrium part of the f_i:

$$\Pi_{\alpha\beta}^{(1)} = \sum_i f_i^{neq} e_{i\alpha} e_{i\beta} = \sum_i (f_i - f_i^{eq}) e_{i\alpha} e_{i\beta}. \tag{3.7}$$

What is obtained is the following form [21]:

$$f_i^{eq}(\rho, \mathbf{u}) = \rho w_i \left(1 + \frac{1}{c_s^2} e_{i\alpha} u_\alpha + \frac{1}{2c_s^4} \bar{e}_{i\alpha} \bar{e}_{i\beta} u_\alpha u_\beta\right). \tag{3.8}$$

where $c_s = \sqrt{RT}$ is termed the *lattice speed of sound* and is a constant depending on the lattice model, and the coefficients w_i are weighting factors that allow to build

isotropic tensors even on irregular lattice models like those described in the next section. The tensors $Q_{i\alpha\beta} = \bar{e}_{i\alpha}\bar{e}_{i\beta}$ are the traceless part of $e_{i\alpha}e_{i\beta}$ and are therefore defined as $Q_{i\alpha\beta} = e_{i\alpha}e_{i\beta} - c_s^2\delta_{\alpha\beta}$.

After having described the whole process that led to the LB from the LGCA method it is important to emphasize that the LB can be also derived directly from the Boltzmann equation, via the following steps [22]:

- Integration of equation (3.34) over a time step Δt.
- Low Mach number expansion of the equilibrium Maxwellian distribution function (2.31):

$$f^{eq} \approx \frac{\rho \ \exp\left(\frac{-\boldsymbol{\xi}^2}{2RT}\right)}{(2\pi RT)^{D/2}} \times \left[1 + \frac{(\boldsymbol{\xi}\cdot\mathbf{u})}{RT} + \frac{(\boldsymbol{\xi}\cdot\mathbf{u})^2}{2(RT)^2} - \frac{\mathbf{u}^2}{2RT}\right] + \mathcal{O}(\mathbf{u}^3). \tag{3.9}$$

- Discretizationof the velocity space $\boldsymbol{\xi}$ in order to obtain the minimum necessary $\{\mathbf{e}_i | i = 0 \dots b-1\}$ required to recover the NS equations.

Whatever is the approach adopted, the Navier-Stokes equations are recovered by means of a multi-scale expansion. The details of this process can be found for instance in [1]; here only the basic ideas are reported. The first step consists in introducing one spatial and two time scales as follows:

$$\partial_t = \varepsilon\partial_{t_1} + \varepsilon^2\partial_{t_2} \tag{3.10a}$$

$$\partial_\alpha = \varepsilon\partial_{\alpha_1}. \tag{3.10b}$$

In this way physical phenomena occurring at different time scales can be separately examined emphasizing their separated contribution to the equations of motions. The definitions (3.10a) and (3.10b) The generic distribution function is as well expressed as power series respect to the small parameter $\varepsilon \ll 1$: $f_i = \sum_{k=0}^{\infty} \varepsilon^k f_i^k$. The first two terms are sufficient to recover the NS equation, so the power series is truncated as follows:

$$f_i = f_i^{(0)} + \varepsilon f_i^{(1)} + \varepsilon^2 f_i^{(2)} + \mathcal{O}(\varepsilon^3) = f_i^{eq} + f_i^{neq} + \mathcal{O}(\varepsilon^2), \tag{3.11}$$

The second step consists in Taylor-expanding up to second order terms the left hand side of (3.4). Through some algebra the incompressible NS are obtained with a $\mathcal{O}(Ma^3)$ term, therefore the LB is said to be a *weakly compressible method*. Thermodynamic pressure and kinematic viscosity are written as:

$$p = c_s^2 \rho. \tag{3.12}$$

and

$$\nu = \frac{2\tau - 1}{6}\frac{\Delta x^2}{\Delta t} = \left(\tau - \frac{1}{2}\right) c_s^2 \Delta t \tag{3.13}$$

Pressure is therefore obtained by a state equation, rather than by solving an elliptic equation like (2.15), while (3.13) prescribes that $\tau > 0.5$. Some comments concerning the numerical implementation of LB are in order now. First of all it is important to note that the Courant-Fredrick-Levy number (CFL) is equal to 1, making LB quite inefficient for solving steady state problems. From (3.13) it is clear that the spatial and temporal discretization are related to the kinematic viscosity of the fluid to be simulated. Since c_s is determined by the chosen lattice structure $\mathcal{L}$, the temperature is frozen and the presented implementation should be referred to as *athermal LB* [23]. From kinetic theory the actual definition of sound speed is $c_s = \sqrt{\gamma RT}$ where $\gamma = c_p/c_v = 1 + (2/D)$. In the presented formulation the ratio of specific heat is therefore 1, meaning the fluid molecules that are being modelled have infinite degrees of freedom, which of course does not make any physical sense. The lattice speed of sound is therefore a numerical artifact of the LB formulation, a pseudo-compressibility parameter that allows the flow to relax to the appropiate incompressible viscous solution[1]. If the fluid to be simulated has to retain its physical

[1]The direct counterpart of LB among classical CFD schemes is the Chorin method of artificial compressibility [24], in which the isothermal NS equations (2.14a)-(2.14c) are subsituted by:

$$\partial_t \rho + \partial_\alpha \rho_0 u_\alpha = 0 \tag{3.14a}$$

$$\partial_t u_\alpha + u_\beta \partial_\beta u_\alpha = -\frac{1}{\rho_0}\partial_\alpha P + \nu \partial_\alpha^2 u_\alpha + g_\alpha \tag{3.14b}$$

$$P = \frac{\rho}{\delta} \tag{3.14c}$$

where ρ_0 is the reference density of the incompressible fluid, ρ is the *artificial density*, $\delta = 1/\sqrt{c_s}$ is the *artificial compressibilty* based on the *artificial sound speed* c_s.

speed of sound the coupling among space and time scales imposed by (3.13) can make LB just not practical at all [25]: taking water as example ($c_s \approx 1500m/s$, $\nu \approx 10^{-7}m^2/s$), a LB simulation with $\tau = 1$ would require $\Delta x = \mathcal{O}(10^{-8}m)$ and $\Delta t = \mathcal{O}(10^{-11}s)$! Concerning the stability, from (3.13) it is clear that to reach high Reynolds number with a fixed space and time discretization one needs to reduce the relaxation time. Unfortunately the LBGK formulation become unstable when $\tau \approx 0.5$ [26]. Alternatively one can increase the number of nodes reducing the lattice space, but that makes the simulation computationally expensive. A way to tackle this last issue will be described in the next chapter.

Thermal LBGK has so far proved to be less robust than its athermal couterpart; energy dynamics is accounted by increasing the number of speeds in order to match an increased number of kinetic moments, but that makes the schemes prone to instabilities because of the occurrance of high-order dispersion relations [23]; besides the Prandtl number Pr is limited to 0.5 because of the SRT formulation [27].

3.3 The Entropic lattice Boltzmann formulation

As stated in the previous section, the BGK formulation is prone to instabilities when dealing with low-viscosity flows. Instability is related to the occurrance of negative distribution functions. A LB formulation which is supported by a "lattice" equivalent of Boltzmann H-theorem (see chapter 2) should possess a higher stability. Unfortunately none of the formulations adopting an f_i^{eq} given by a polynomial velocity-dependent expression like (3.5) can obey an H-theorem [28]. It is nevertheless possible to build alternative formulations of the equilibrium distributions fulfilling this requirement. That is the idea on which the *Entropic lattice Boltzmann* schemes (ELB) [29, 30, 31] are based. The first element characterizing these schemes is the definition of a convex discrete H-function, that can be obtained evaluating the Boltzmann H-function (2.32) via the Gauss-Hermite quadrature [31]:

$$H = \sum_{i=0}^{b-1} f_i \ln\left(\frac{f_i}{w_i}\right). \tag{3.15}$$

The local equilibrium distribution has to minimize the H-function, as well as to fulfill the constraints (3.6a)-(3.6c). The most general expression in D-dimensional

space is given by [29]:

$$f_i^M = \rho w_i \prod_{\alpha=1}^{D} \left(2 - \sqrt{1-u_\alpha'^2}\right) \left(\frac{\frac{2}{\sqrt{3}} u'_\alpha + \sqrt{1-u_\alpha'^2}}{1 - u'_\alpha/\sqrt{3}} \right)^{e_{i\alpha}/\sqrt{3}c_s}, \tag{3.16}$$

where the M reminds that equation (3.16) is analogous to the ordinary Maxwellian distribution given by equation (2.31). The ELB equation is given by:

$$f_i\left(\mathbf{x} + \mathbf{e}_i \Delta t, t + \Delta t\right) - f_i\left(\mathbf{x}, t\right) = -\alpha^\star \beta \left(f_i\left(\mathbf{x}, t\right) - f_i^M\left(\mathbf{x}, t\right) \right). \tag{3.17}$$

Equation (3.17) is characterized by a variable collisional frequency $\theta = \alpha^\star \beta$; β is related to the kinematic viscotiy as follows:

$$\beta = \frac{\Delta t}{2\tau + \Delta t}, \tag{3.18}$$

while $\alpha^\star$ is derived by solving the following nonlinear equation:

$$H(\mathbf{f}) = H(\mathbf{f} + \alpha(\mathbf{f} - \mathbf{f}^{eq})). \tag{3.19}$$

Further details about the resolution of equation (3.19) can be found for instance in [31]. This formulation achieved unconditional numerical stability. Another alternative formulation to tackle the stability issue, the Multiple-Relaxation-Times LB (MRT-LB), will be presented in chapter 5.

3.4 Lattice Models

The FHP-I model was the first $\mathcal{L}$ which it was possible to build isotropic fourth-order tensors. In the successive years, other models were developed, like the FHP-II, having a rest particle permanently laying on the site. This last feature was introduced in LGCA to increase the number of collisions allowed by the lattice in order to reach higher *Re* numbers, and was kept in LB too. A lattice model is uniquely identified by the number of dimensions D and by the number of speeds Q: therefore the FHP-I is referred to as $D2Q6$ model, while the FHP-II is the D2Q7 one. Currently, the most employed model for two dimensional simulations is the $D2Q9$,

while for three dimensional ones, models with 15, 19 and 27 velocities are available. All these last models are termed non-regular lattices or *multi-speed lattices* (MSL) and , as demonstrated in Appendix A, it was necessary to introduce weighting factors w_i in order to preserve isotropy of the lattice tensors up to fourth order. Each lattice structure has at least three types of w_i, corresponding respectively to the particle at rest, $\mathbf{e}_0$, and to "slow" and "fast" speeds. $D3Q27$ has got a further class of vectors, indicated as "fastest" speeds. All these coefficients are reported in Table 3.1, together with the corresponding value of c_s, while the vectors defining each lattice model are listed below; finally, Figure 3.3 illustrates all these $\mathcal{L}$ structures.

Model	Rest	Slow	Fast	Fastest	c_s^2
D2Q7	1/2	1/4	NE	NE	1/4
D2Q9	4/9	1/9	1/36	NE	1/3
D3Q15	2/9	1/9	1/72	NE	1/3
D3Q19	1/3	1/18	1/36	NE	1/3
D3Q27	8/27	2/27	1/54	1/216	1/3

Table 3.1: Parameters characterizing different lattice models. NE means not existing: infact only D3Q27 model has three kinds of speeds, while D2Q7 has just two kinds of speeds.

$$\mathbf{e}_i^{D2Q7} = \begin{cases} (0,0), & i = 0 \\ (\pm 1, 0), & i = 1 \ \dots \ 2 \\ (\pm \cos\frac{\pi}{3}, \pm \sin\frac{\pi}{3}), & i = 3 \ \dots \ 6 \end{cases} \tag{3.20}$$

$$\mathbf{e}_i^{D2Q9} = \begin{cases} (0,0), & i = 0, \\ (\pm 1, 0), \quad (0, \pm 1), & i = 1 \ \dots \ 4 \\ (\pm 1, \pm 1), & i = 5 \ \dots \ 8 \end{cases} \tag{3.21}$$

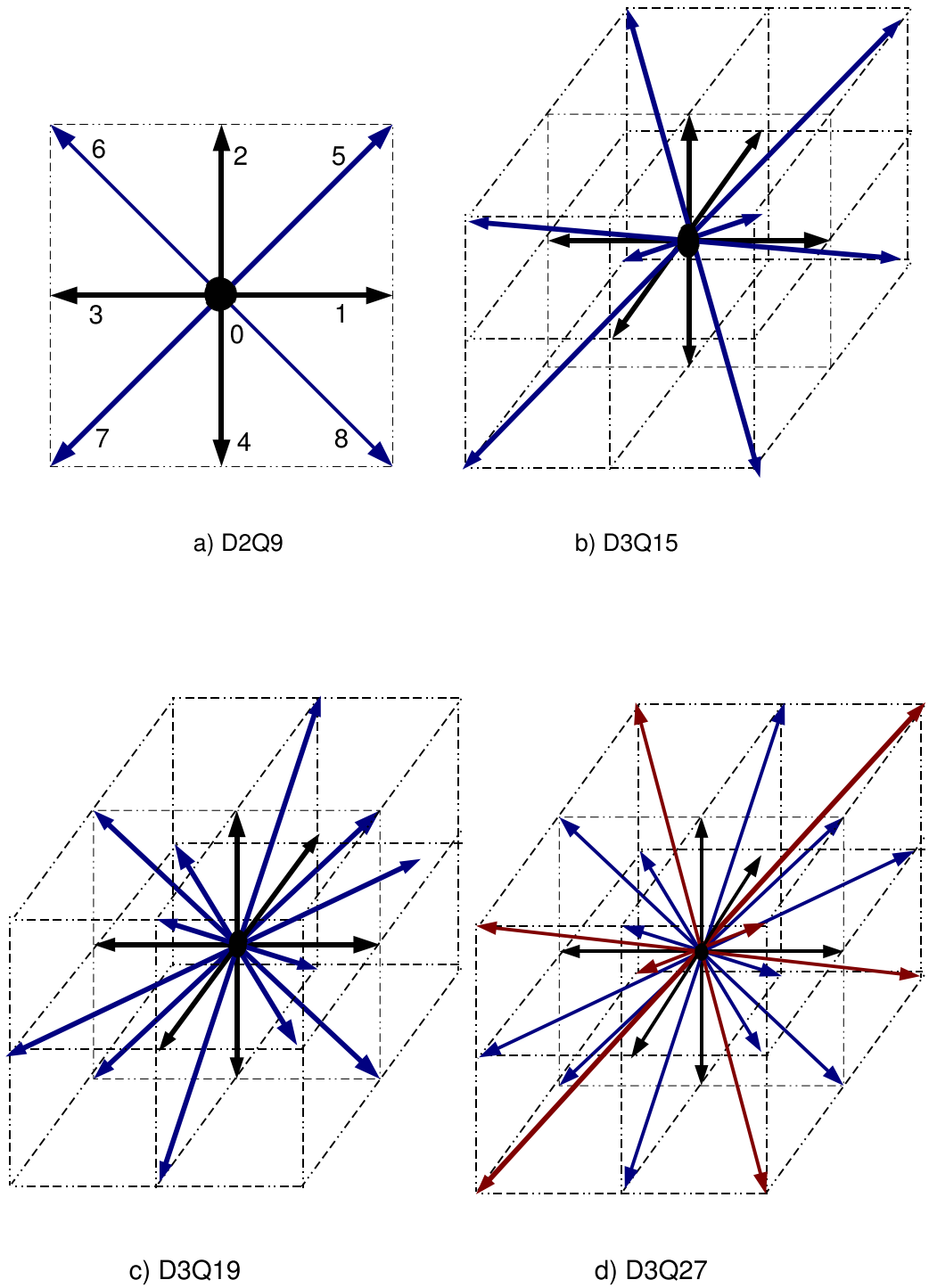

Figure 3.3: Different lattice models for two- and three-dimensional simulations: the zero speed vector is indicated by a circle, while the slow, fast and fastest speed vectors are respectively represented by black, blue and red arrows.

$$\mathbf{e}_i^{D3Q15} = \begin{cases} (0,0), & i = 0, \\ (\pm 1, 0), \quad (0, \pm 1), & i = 1 \ \dots \ 4 \\ (\pm 1, \pm 1), & i = 5 \ \dots \ 8 \end{cases} \tag{3.22}$$

$$\mathbf{e}_i^{D3Q19} = \begin{cases} (0,0,0), & i = 0, \\ (\pm 1,0,0), \quad (0,\pm 1,0), \quad (0,0,\pm 1), & i = 1 \ \dots \ 6 \\ (\pm 1,\pm 1,0), \quad (0,\pm 1,\pm 1), \quad (\pm 1,0,\pm 1), & i = 7 \ \dots \ 18 \end{cases} \tag{3.23}$$

$$\mathbf{e}_i^{D3Q27} = \begin{cases} (0,0,0), & i = 0, \\ (\pm 1,0,0), \quad (0,\pm 1,0), \quad (0,0,\pm 1), & i = 1 \ \dots \ 6 \\ (\pm 1,\pm 1,0), \quad (0,\pm 1,\pm 1), \quad (\pm 1,0,\pm 1), & i = 7 \ \dots \ 18 \\ (\pm 1,\pm 1,\pm 1), & i = 19 \ \dots \ 26 \end{cases} \tag{3.24}$$

3.5 Inserting a body force

In many applications the flow is driven or influenced by a body force $\mathbf{F}$. Many different ways to incorporate the effects of body forces into the LB framework have been proposed: this section is dedicated to a brief description of the most common methods. It is worth to underline that all of them led to the corresponding Navier-Stokes equation via the Chapman-Enskog expansion.

3.5.1 Calculating the equilibrium distribution via an altered velocity (Method I)

This method consists in modifying the equilibrium speed appearing in (3.8) to take into account the momentum change occurring at each time step because of the force $\mathbf{F}$. We have $f_i^{eq} = f_i^{eq}(\mathbf{u}^{eq}, t)$ where:

$$\mathbf{u}^{eq} = \mathbf{u} + \frac{\tau}{\rho}\mathbf{F}. \tag{3.25}$$

In (3.25) $\mathbf{u} = \sum_i f_i \mathbf{e}_i / \rho$. The macroscopic fluid momentum $\mathbf{j}$ is the average of the momentum before and after the collision:

$$\mathbf{j} = \rho\mathbf{u} + \frac{1}{2}\mathbf{F} \tag{3.26}$$

This method is first-order accurate in $\boldsymbol{\Delta}\mathbf{u}$, and it is part of the original formulation of the so-called Shan-Chen model for multiphase flows, which will be described in Chapter 4.

3.5.2 Adding an addictional term to the Boltzmann equation (Method II)

The Boltzmann equation incorporating the effect of a body force is given by (2.24). It is very difficult to evaluate the term $\partial_{\boldsymbol{\xi}} f$. Nevertheless, because of the H-theorem it is reasonable to consider the distribution function to be always quite close to its equilibrium value, making it possible to write:

$$\partial_{\boldsymbol{\xi}} f \approx \partial_{\boldsymbol{\xi}} f^{eq} = -\frac{\boldsymbol{\xi} - \mathbf{u}}{RT} f^{eq} \tag{3.27}$$

This idea can be applied also into a LB scheme: the collision operator of (3.4) is modified by adding a new term related to the body force, according to the expression:

$$\Omega_i = -\frac{1}{\tau}\left(f_i\left(\mathbf{x}, t\right) - f_i^{eq}\left(\mathbf{x}, t\right)\right) + \frac{\left(\mathbf{e}_i - \mathbf{u}\right)\cdot\mathbf{F}}{c_s^2} f_i^{eq}. \tag{3.28}$$

The equilibrium distribution function is left unchanged, and the macroscopic momentum is obtained by (3.20). This method is applied for instance in the multiphase model proposed in [32].

3.5.3 Exact Difference Method (EDM)

Both methods I and II lead to NS equations characterized by an unphysical term given by $\partial_\beta(n\tau - 1/2)\left(u_\alpha F_\beta + u_\beta F_\alpha\right)$ [33]. This method was proposed in [34] and [35].

In order to introduce it, let us consider a uniform flow with density ρ and velocity $\mathbf{u}$. In this case the distribution function is the Maxwell-Boltzmann one (2.39). If a short uniform pulse force $\mathbf{F}$ along the flow direction is applied, the distribution functions persist in the equilibrium form but at a shifted velocity $\mathbf{u} + \boldsymbol{\Delta}\mathbf{u}$. For the LB that means $f_i(\mathbf{x}, t + \Delta t) = f_i^{eq}(\mathbf{u} + \boldsymbol{\Delta}\mathbf{u})$ if initially the relation $f_i(\mathbf{x}, t) = f_i^{eq}(\mathbf{u})$ holds. In the EDM the body force effect is accounted by adding a new term to the collision operator like in Method II:

$$f_i\left(\mathbf{x} + \mathbf{e}_i\Delta t, t + \Delta t\right) - f_i\left(\mathbf{x}, t\right) = -\frac{1}{\tau}\left(f_i\left(\mathbf{x}, t\right) - f_i^{eq}\left(\mathbf{u}, t\right)\right) + \Delta f_i^{eq}, \tag{3.29}$$

where

$$\Delta f_i^{eq} = f_i^{eq}\left(\mathbf{u} + \boldsymbol{\Delta}\mathbf{u}, t\right) - f_i^{eq}\left(\mathbf{u}, t\right) \quad \text{with} \quad \Delta\mathbf{u} = \frac{\mathbf{F}\Delta t}{\rho}. \tag{3.30}$$

With this new method it is possible to achieve $f_i(\mathbf{x}, t + \Delta t) = f_i^{eq}(\mathbf{u} + \boldsymbol{\Delta}\mathbf{u})$ if initially $f_i(\mathbf{x}, t) = f_i^{eq}(\mathbf{u})$. The distribution function are therefore just shifted in the velocity space, but remain in equilibrium. The velocity change is not dependant on the τ like it happens in Methods I and II. The action of the body force is computed exactly, although the LB is a discrete method, therefore this method is called the *Exact Difference Method* (EDM). Moreover, the EDM is fully consistant with the most general formulation of the Boltzmann equation in presence of a body force (2.24), it is easy to implement and determines a modest increment of computational load, because it requires only a further calculation of f_i^{eq}. Besides, it can be coupled to whatever form of the collision operator Ω, as it will be demonstrated in Chapter 6. Finally the Chapman-Enskog expansion of equation (3.29) shows that no any addictional incorrect terms related to $\mathbf{F}$ appear in the NS equations [34].

3.6 Boundary Conditions

In this section some of the different kinds of boundary conditions (BCs) developed for LB are reviewed. As for every CFD method, even in LB a fundamental role in determining the accuracy is played by the BCs, which, of course, have to be expressed

in terms of the probability distribution functions. Considering a computational domain enclosed by a boundary $\partial\Omega$ and a lattice node $\mathbf{x}$ which in the most general case has one or more of its links cut by $\partial\Omega$. After the streaming step some of the $f_i(\mathbf{x}, t)$ are unknown. The formulation of the BCs in the framework of LB consists in the determination of these unknown distribution functions *incoming* from a fictitious layer of points outside the computatinal domain, f_i^{in}, in terms of the known ones f_j [16] in order to recover the macroscopic quantities or the macroscopic gradients prescribed at that boundary: .

$$f_i^{\text{in}}(\mathbf{x}) = \sum_y \sum_j \mathcal{B}(\mathbf{x} - \mathbf{y}) f_j^{\text{out}}(\mathbf{x}). \tag{3.31}$$

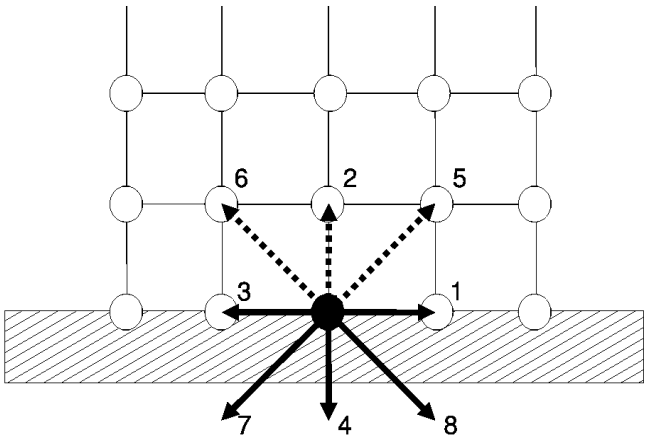

Figure 3.4: General framework for Boundary conditions.

In (3.31) $\mathcal{B}$ is the BC operator, depending on $\mathbf{x}$ but even of the neighbouring nodes $\mathbf{y}$. Figure 3.4 explains the point: for the sake of simplicity, a two-dimensional flow dealt with the D2Q9 model is considered; besides the node $\mathbf{x}$ lays exactly on a straight boundary. After the propagation phase in $\mathbf{x}$ there are 6 known distribution functions, namely f_0, f_1, f_3, f_4, f_7 and f_8, while f_2, f_5 and f_6 have to be determined. It is important to underline that some boundary conditions schemes like those presented in [36] and [37] are based on the substitution of the *whole* set of distribution functions. In these schemes the vision of a fictitious layer outside the computational domain is abandoned. The boundary condition scheme should account for the physical modelling of the interaction occurring on the boundary, for

instance between a fluid and a solid surface. Since it has to respect the constraints imposed by the mass and momentum conservation, it can happen that the number of unknown overtakes the number of constraints, leaving some "degrees of freedom" to insert physical models. Therefore, when developing a new BC, the challenge is to include as much relevant interface physics as possible without making too hard the problem from a mathematical point of view. Keeping in mind the recovery of macroscopic quantities like density and speed one might think of simply assigning to the unknown f_i the corresponding equilibrium values: this strategy has been followed for instance in works like [38], [39] or [4], concerning the simulation of the flow in a lid-driven cavity in order to model the moving wall. This approach is intuitive but not correct, because it ignores the nonequilibrium part of the distribution function which, as seen in (3.7), is responsible for the viscous part of the stress tensor [40] and is directly related to the velocity gradients. Therefore this approach has not been considered in this study. In what follows the implementation of some typical boundary conditions like periodic and solid boundaries into the LB framework will be discussed, while two of the different schemes proposed in the literature for pressure (which should be termed *density boundary conditions* because of (3.12)) and velocity BC are reviewed in this section, namely the one proposed by Zou and He [41] (ZH) and the extrapolation scheme proposed by Guo *et al.* [42] and [43].

3.6.1 Periodic boundaries

After this brief introduction, let us start with periodic boundaries: dealing with such boundaries is very simple in LB, because all that has to be done is copying the outgoing PDFs from a boundary as the incoming PDFs of the opposite boundary.

3.6.2 Dealing with solid walls

Much work has been devoted to search for accurate BCs for solid walls: the simplest model available for such purpose comes from LGCA, and is called *full-way bounce back scheme*(BBK). According to this scheme, depicted in Figure 3.5, when a particle distribution streams to a wall node it scatters back in the opposite direction, toward the originating node, reached in two time steps. The BBK is very easy to implement, and can be employed to represent even complex geometries like

curvilinear surfaces that are approximated as stairs. Adopting this scheme means no collision process occurs at the boundary because not all the f_i are known. If the velocity is measured after the application of the boundary condition, but before the application of successive propagation step, a non zero *slip velocity* can be measured on the boundary: in [44] an expression of such velocity was given for the Poiseuille flow case, from which it is clear the BBK is first-order accurate only:

$$u_s = \frac{2u_c}{3n^2}\left[(2\tau - 1)(4\tau - 3) - 3n\right] \tag{3.32}$$

In (3.32) n is the channel width in lattice units. A first improvement is given by the so-called *modified bounce-back scheme*: it consists in mirroring the unknown PDFs with the corresponding opposite distributions streaming out from the computational domain:

$$f_i^{\text{in}} = f_{\bar{i}}^{\text{out}}, \tag{3.33}$$

where f_i^{in} is the unknown, incoming PDF on the i-th direction, while $f_{\bar{i}}^{\text{out}}$ is the outgoing PDF along the opposite direction $\bar{i}$. This time, collision occurs on the node, because all the distributions are known. This scheme has the advantage of not requiring a special treatment for corner nodes and most importantly achieves a second-order accuracy [44], as confirmed by the expression of the slip velocity:

$$u_s = \frac{u_c}{3(n-1)^2}\left[4\tau(4\tau - 5) + 3\right]. \tag{3.34}$$

Another variant consists in applying the BBK scheme, but placing the wall between the bounce-back and the first fluid raw: this scheme, termed *halfway bounce-back* (HWBBK), is second order accurate [44]. It is worth to underline that these orders of accuracy were obtained for a simple case like the Poiseuille flow. Further investigation is necessary for more complicated flows, like the driven cavity problem.

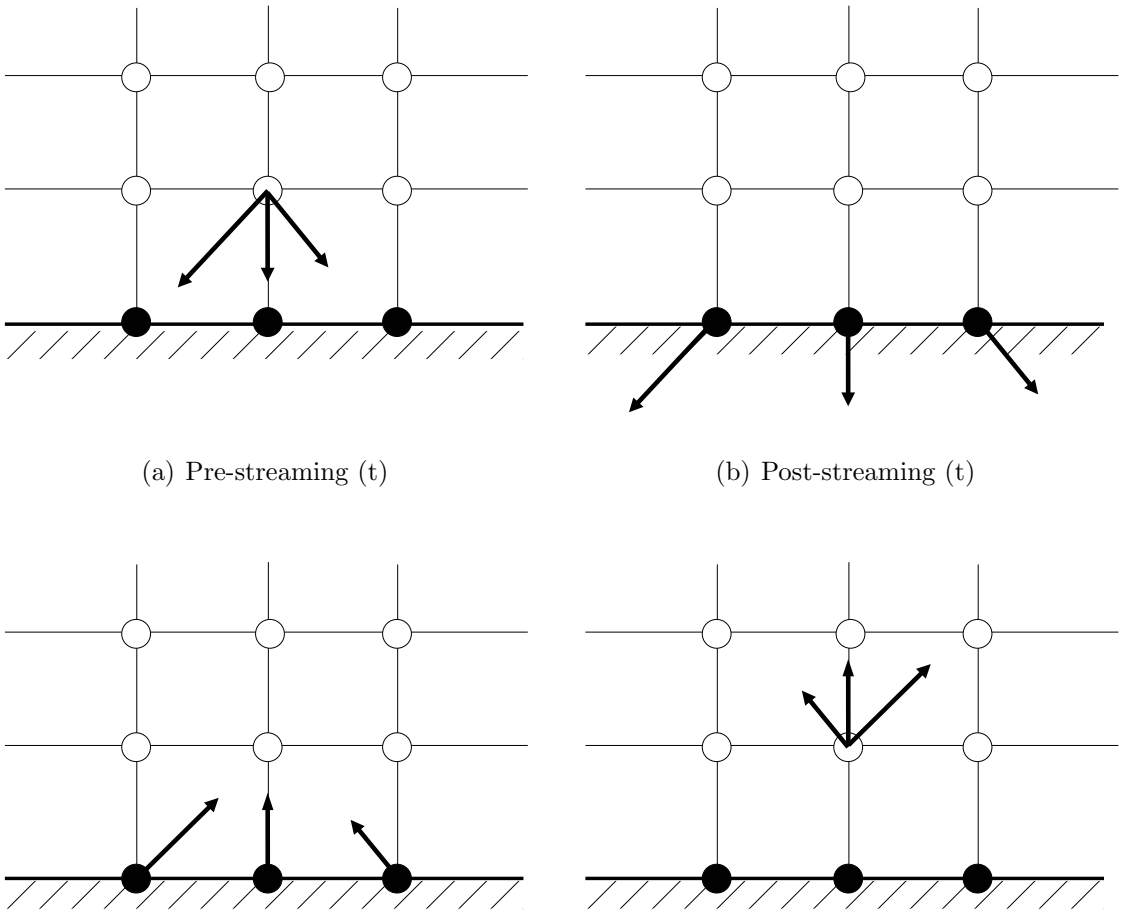

(a) Pre-streaming (t)

(b) Post-streaming (t)

(c) Bounce Back (t)

(d) Post-streaming (t+1)

Figure 3.5: BBK scheme on a D2Q9 lattice. Bounce-back nodes are depicted in black.

3.6.3 Zou and He scheme

This scheme can be applied to both velocity and pressure boundaries. Considering again Figure 3.4, in both cases the unknowns are f_2, f_5, and f_6, plus respectively the density ρ and the speed component normal to the boundary. Four equations are therefore necessary: the first three come from (3.6a) and (3.6b); the remaining equa-

tion is obtained assuming extending the bounce-back rule to the non-equilibrium part of the $f_{i,n}$ normal to the considered boundary:

$$f_{i,n}^{(1)} = f_{i,nopp}^{(1)} \tag{3.35}$$

where $\mathbf{e}_{i,nopp} = -\mathbf{e}_i$ (in the particular case of Figure 3.4 equation (3.35) means $f_2 - f_2^{eq} = f_4 - f_4^{eq}$). Considering for instance Figure 3.4 as representing a velocity boundary it is possible to write after some algebra:

$$\rho = \frac{1}{1-u_y}\left[f_0 + f_1 + f_3 + 2(f_4 + f_7 + f_8)\right] \tag{3.36a}$$

$$f_2 = f_4 + \frac{2}{3}\rho u_y \tag{3.36b}$$

$$f_5 = f_7 - \frac{1}{2}(f_1 - f_3) + \frac{1}{2}\rho u_x + \frac{1}{6}\rho u_y \tag{3.36c}$$

$$f_6 = f_8 + \frac{1}{2}(f_1 - f_3) - \frac{1}{2}\rho u_x + \frac{1}{6}\rho u_y. \tag{3.36d}$$

The collision step is applied even on boundary nodes. Special treatment is required on corner nodes, where the previously seen constraints are not enough to match the number of unknown distributions. An example is reported in Figure 3.6: supposing to deal with top node of a channel inlet the unknowns relative to the black node are ρ, f_1, f_4, f_5, f_7 and f_8.

The idea is to use the same constraints seen before, plus another non-equilibrium bounce-back rule because there are two couples of distribution functions normal to the boundaries: in this case that means $f_2 - f_2^{eq} = f_4 - f_4^{eq}$ and $f_1 - f_1^{eq} = f_3 - f_3^{eq}$. The density is extrapolated by the closest node where it is known (the red node in Figure 3.6). The final outcome is given by:

$$f_1 = f_3 \tag{3.37a}$$

$$f_4 = f_2 \tag{3.37b}$$

$$f_5 = f_7 = \frac{1}{2}(\rho - f_0) - (f_2 + f_3 + f_6) \tag{3.37c}$$

$$f_8 = f_6 \tag{3.37d}$$

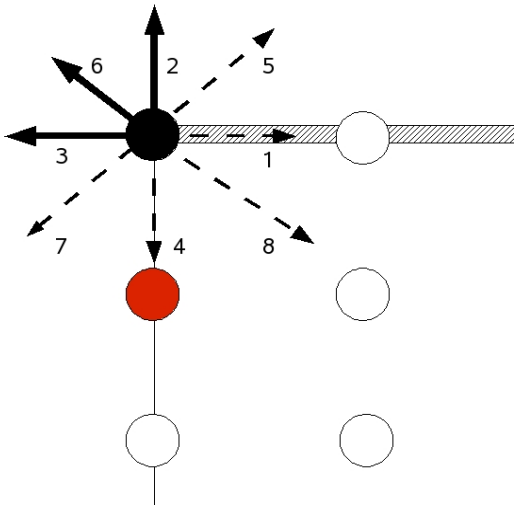

Figure 3.6: Sketch of distribution functions at a corner node (indicated in black). The unknowns are depicted by dashed arrows.

A similar procedure can be followed on the other corner nodes. It is important to notice that this BC can model a general velocity boundary, therefore it is possible to impose a velocity profile at an inflow, or even to deal with moving walls (as will be shown in the next chapter). This BC enforces the velocity value explicitly, but nothing is specified about the stress tensor. Nevertheless it can be demonstrated that the stress tensor is correctly recovered. For three-dimensional problems the algorithm needs to be modified, because from (3.6a) and (3.6b) come four equations, which do not match the five ($\mathcal{L} = D3Q15$) or nine ($\mathcal{L} = D3Q19$) unknowns. The procedure suggested in [41] is quite complex: considering again a velocity boundary, first of all (3.35) is applied to *all* the unknown populations, recovering the normal macroscopic velocity u_n; subsequently the excess of momentum in the remaining directions β is evaluated as:

$$\delta_\beta = \sum_{i \neq n} f_i^{(1)} e_{i\beta} \qquad \text{for} \beta \neq n. \tag{3.38}$$

The last step of this procedure consists in the redistribution of δ_β over the unknown distributions in order to obtain the final non-equilibrium part consistent with (3.6b), which is here termed $g_i^{(1)}$:

$$g_i^{(1)} = f_i^{(1)} - \sum_{\beta \neq n} \frac{1}{n_\beta} e_{i\beta}\delta_\beta \quad \text{for all unknown } f_i, \tag{3.39}$$

where n_β is the number of unknown particle populations having $e_{i\beta} \neq 0$. The complexity of this process makes the ZH scheme not the best choice for 3D simulations. This scheme cannot be applied to curved boundaries.

3.6.3.1 Extrapolation BC

Considering the boundary node depicted in Figure 3.7 and the unknown $f_2(B,t)$ distribution, it can be written as the summation of an equilibrium and non-equilibrium part $f_2(B,t) = f^{eq}(B,t)_2 + f^{neq}(B,t)_2$. This BC consists in computing both these terms with an extrapolation from the corresponding distribution in the neighbour fluid node E (indicated in red in Figure 3.7). Starting from f_2^{neq}, from (3.11) comes that $f_2^{neq} = \varepsilon f_2^{(1)}$. Since node B is neighbour of node E and $\Delta x = \varepsilon c$ f_2^{neq} can be extrapolated from node E, as $f_2^{neq}(B,t) = \varepsilon(f^1(E,t)_2 + \mathcal{O}(\varepsilon) = f_2^{neq}(E,t) + \mathcal{O}(\varepsilon)^2$. The next step is to determine the equilibrium part. Considering for instance a velocity boundary, the unknown on node B is the density ρ_E. Adopting the f_i^{eq} form proposed in [45] for reduce compressibility effects it is possible to approximate the equilibrium distribution using the density in node E:

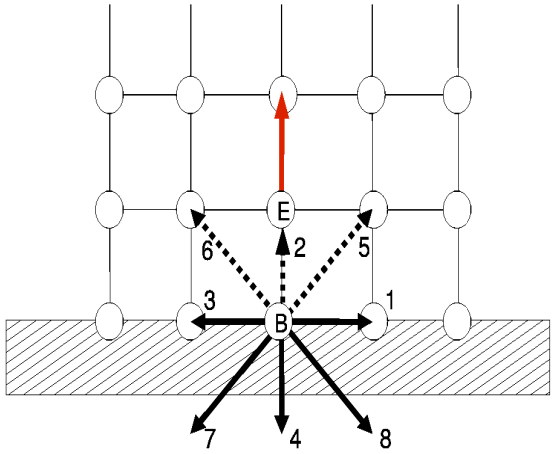

Figure 3.7: Sketch of extrapolation boundary condition.

$$f_2^{\bar{eq}} = \rho_E w_i + \rho_0 w_i \left(\frac{1}{c_s^2} e_{i\alpha} u_{B\alpha} + \frac{1}{2c_s^4} \bar{e}_{i\alpha} \bar{e}_{i\beta} u_{B\alpha} u_{B\beta} \right). \tag{3.40}$$

Since $\rho_E - \rho_B = (\mathbf{e}_2 \cdot \nabla\rho)\Delta x = \mathcal{O}(Ma^2\varepsilon)$ it is possible to write:

$$f_2^{eq}(B,t) = f_2^{\bar{eq}} + \mathcal{O}(Ma^2\varepsilon). \tag{3.41}$$

From (3.13) the Ma number can be related to the Re as follows:

$$Ma = U_c/c_s = \left(\tau - \frac{1}{2}\right) \frac{Re}{3L} \Delta x. \tag{3.42}$$

Chosing τ to have $\left(\tau - \frac{1}{2}\right) \frac{Re}{L} = \mathcal{O}(1)$ will lead to $Ma = \mathcal{O}(\varepsilon)$, thus from (3.41) second order accuracy follows. Pressure boundaries can be modelled in a similar way, obtaining the same order of accuracy.

3.7 Rescaling to physical quantities

Table 3.2 summarizes the relations occurring between the most important fluid properties expressed in lattice units (LU) and the corresponding physical ones: in the formulas reported, m represents the molecular weight of the considered fluid, while $c = \Delta x/\Delta t$ is referred to as the *lattice speed* .

3.8 Test Cases

In this section the accuracy of the different BC schemes for solid walls modelling will be discussed by considering two classical test cases, namely the Poiseuille flow and the lid-driven cavity. These cases are both 2D so the $\mathcal{L}$ is the D2Q9 model defined by (3.21).

3.8.1 Poiseuille Flow

It is interesting to discuss the relation between the body force and the flow one wants to simulate. For some simple cases it is easy to relate $\mathbf{F}$ to the flow characteristics.

Quantity	LB	Real
Density	$\rho = \sum_i f_i$	ρ^{real}=$m\rho$
Macroscopic speed	$\mathbf{u} = \frac{1}{\rho}\sum_i f_i \mathbf{e}_i$	$\mathbf{u}^{real}$=$c\mathbf{u}$
Speed of sound	c_s	c_s^{real}=$c_s c$
Pressure	$p = c_s^2 \rho$	p^{real}=$\left(\frac{\Delta x}{\Delta t}\right)^2 mp$
Relaxation time	τ	τ^{real}=$\tau \Delta t$
Kinematic viscosity	$\nu = (2\tau - 1)/6$	ν^{real}=$\nu \frac{\Delta x^2}{\Delta t}$

Table 3.2: Relations between lattice and physical quantities.

The two-dimensional Poiseuille flow is such an example: for $Re \leq 2000$ the regime is laminar and both the time derivative and the nonlinear advection terms are null. Given x, y and u respectively to represent the main flow direction, the crossflow direction and the x-velocity component, the incompressible NS (2.14b) reduces to a balance between the pressure and the viscous term:

$$\partial_x p = -\nu \partial_{yy} u. \tag{3.43}$$

The flow is pressure driven; it was shown before that pressure and density are related by a state equation in the LB framework, and that the term c_s is related to the temperature: for an isothermal, and incompressible flow like this one the question is obvious: where does the pressure gradient come from? This is the drawback of avoiding to solve a Poisson equation: since that the speed of sound has to be of $\mathcal{O}(1)$ in lattice units, pressure and density fluctuation are of the same order. The solution, if one wants to keep density constant (apart from the small variations due to the aforementioned weakly compressible nature of the method), is to *mimic* the effect of the pressure gradient by means of a constant body force. Equation (3.43) can be analytically solved, giving a parabolic velocity profile depending only on the y coordinate:

$$\bar{u_x} = \frac{4U_c}{H}\left(1 - \frac{y}{H}\right) \tag{3.44a}$$

$$\bar{u_y} = 0 \tag{3.44b}$$

where U_c is the maximum speed, reached in the centre of the channel cross section, and H is half of the height of the channel itself. The pressure gradient G driving the flow can be related to this velocity:

$$\frac{p_{in} - p_{out}}{L} = \frac{8\rho\nu U_c}{H^2}. \tag{3.45}$$

Where p_{in} and p_{out} are respectively the constant pressures at inflow and outflow sections. It is now sufficient to put into (3.45) $G = \frac{p_{in}-p_{out}}{L}$ and to apply periodic BC at inflow/outflow sections of the channel to observe the expected parabolic profile. This flow case was studied here with the LBGK model. The full-way bounce-back (BBK), the modified bounce-back (ModBBK), and the ZH scheme were employed and their accuracy evaluated at two Re numbers, 6 and 30. In all the simulations the following conditions were used:

- The tube length is twice its height.
- The initial density is $\rho_0 = 1.0$.
- A parabolic velocity profile with maximum speed U_{max} is imposed at the inflow, while a constant density (pressure) $\rho_{out} = 1.0$ is imposed at the outflow. Both these boundary conditions are realized employing the scheme proposed by Zou and He, explained in the previous section.
- Relative error is measured by means of the expression:

$$E = \frac{\sum_{i,j} \left(|u_x(i,j) - \bar{u_x}(i,j)| + |u_y(i,j) - \bar{u_y}(i,j)| \right)}{\sum_{i,j} \left(|\bar{u_x}(i,j)| + |\bar{u_y}(i,j)| \right)}, \tag{3.46}$$

  where all the sums are defined on the whole computational domain, while $\bar{u_x}(i,j)$ and $\bar{u_y}(i,j)$ are the analytical solution values as defined by equations (3.44a) and (3.44b) .
- Convergence is evaluated every $\Delta t = 1000$ steps, and is considered achieved when the 2 velocity fields fulfil the following condition:

$$\frac{\sum_{\mathbf{x}} \sqrt{\left(u_x(\mathbf{x},t) - u_x(\mathbf{x},t-\Delta t)\right)^2 + \left(u_y(\mathbf{x},t) - u_y(\mathbf{x},t-\Delta t)\right)^2}}{\sum_{\mathbf{x}} \sqrt{(u_x(\mathbf{x},t-\Delta t)^2 + u_y(\mathbf{x},t-\Delta t)^2)}} \leq 10^{-8} \tag{3.47}$$

3.8.1.1 Re=6

The relaxation time equals 1.0, so that kinematic viscosity is, in lattice units, $\nu = 1/6$ in every simulations. Different grids have been considered, namely 20×11, 40×21, 80×41 and 160×81: the centreline velocity is chosen respectively equal to $u_{max} = 0.1,\ 0.05,\ 0.025,\ 0.0125$, according to the desired Re. Figure 3.8 summarizes the results obtained: as it is possible to see from the left picture, related to the 160×81 case, the u-component velocity profile along the cross-section of the channel matches the analytic solution almost perfectly, especially employing ModBBK and Zou-He BCs; the simple BBK exhibits a slight discrepancy, especially in the centre of the channel, where velocities laying above the analytic ones are produced. More interesting is the picture on the right, showing the trend of relative error (3.46) as the grid resolution is increased. From the computed values, the slopes of the curves related to BBK, ModBBK and Zou-He BCs are, respectively, -1 and -2 confirming the less accuracy achieved by BBK. In this case, the ModBBK proves to be the best BC among those tested.

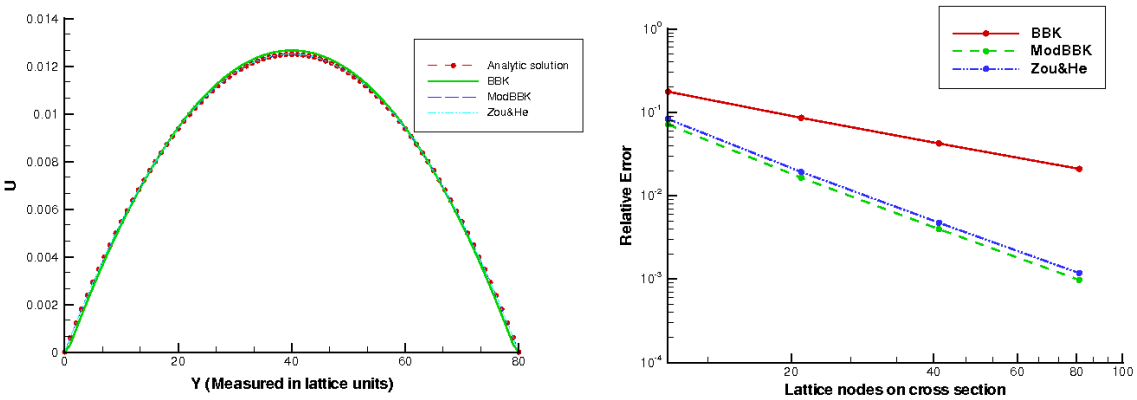

(a) (b)

Figure 3.8: Summary of results for Re=6 case: (a) Comparison between analytic and computed solutions employing different kinds of BCs for the 160x81 case. (b) Comparison of the accuracies of the tested BCs.

3.8.1.2 Re=30

The relaxation time equals 0.6, so that kinematic viscosity is, in lattice units, $\nu = 1/30$ in every simulations. The same grids of the previous case have been considered: the centreline velocity is chosen, once again, respectively equal to $u_{max} = 0.1,\ 0.05,\ 0.025,\ 0.0125$, so to always get the desired Re. As Figure 3.9 shows, the results obtained are qualitatively similar to the previous case. Once again the analytic solution is matched almost perfectly, and once again the BBK demonstrates to be the less accurate BC.

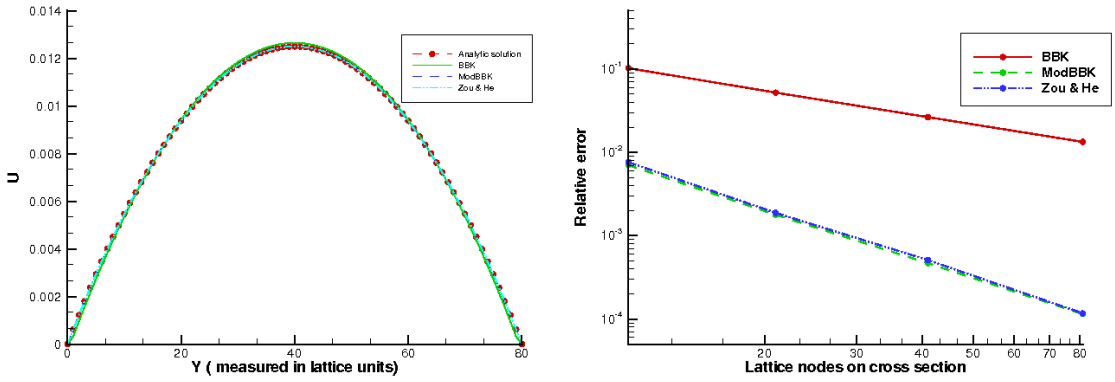

(a) (b)

Figure 3.9: Summary of results for Re=30 case: (a) Comparison between analytic and computed solutions employing different kinds of BCs for the 160x81 case. (b) Comparison of the accuracies of the tested BCs.

3.8.2 The Lid-Driven Cavity

So far, the numerical experiments related to the Poiseuille flow confirmed what was expected: the BBK is first-order accurate only, while BCs like modified bounce-back or the one proposed by Zou and He achieve a second-order accuracy. But is that always true? To answer that question, it is worth to consider a more complicated flow: the two-dimensional lid-driven cavity problem constitutes such an example. Many important phenomena like longitudinal and corner vortices, Taylor-Görter vortices, transition and turbulence can be observed in this closed geometry. That made this flow the object of a high number of either experimental or numerical

studies. A complete review of the literature concerning this case is given in [46]. Given a rectangular cavity with depth $\bar{H}$, width $\bar{W}$ and aspect ratio $D_c = \bar{H}/\bar{W}$, the fluid flow is driven by the top wall moving at speed U_0. The resulting Reynolds number is $Re = \bar{W}U_0/\nu$. In this section the most widely studied case of $D_r = 1$ is examined. Table 3.1 summarizes the simulation parameters for some of the different cases studied. Since there is no analytical solution for this flow the benchmark is given by the performance reported in other CFD and LB works.

Re	U_0	$\nu(\Delta x^2/\Delta t)$	τ	Grid Size
100	0.01	0.0256	0.5768	257×257
200	0.1	0.128	0.884	257×257
400	0.1	0.064	0.692	257×257
1000	0.1	0.0256	0.5768	257×257

Table 3.3: Simulation parameters for the lid-driven cavity flow.

The kinetic viscosity, in lattice units, is obtained from the Reynolds number; then, the relaxation time is computed by using equation (3.13). Each case is studied applying, for the three solid walls, the same three boundary conditions considered for the Poiseuille flow and the ZH scheme for the moving wall. Figure 3.10 shows the streamlines for the four cases. The streamlines have been calculated using TECPLOT ™: the result was similar to what found by integrating with trapezoidal rule the velocity field as done in [38]. These pictures are relative to the usage of ModBBK as BC for solid walls; anyway, all the simulations show a good behaviour of simple BBK, while applying the scheme of Zou and He to all the walls does not give satisfying results. It is clearly visible the movement of the centre of the primary vortex, as the Reynolds number increases, toward the bottom of the cavity. The good performance of BBK scheme is evident from Figure 3.10, where the non-dimensional velocity components computed along the horizontal symmetry lines are compared to the benchmark solutions of Hou et *al.* The results are compared, in each case, to those obtained in [38]. The plots reported show a very good performance achieved by the BBK scheme, which corresponds to a solution almost indistinguishable from the benchmark one. That is not surprising, since in [38], the same scheme is employed

at solid walls, while the moving wall is modelled giving the distribution functions their equilibrium value, as previously stated. It is important, anyway, to underline that the ModBBK scheme does not produce significantly better profiles. Table 3.4 reports the coordinate of the centres of the vortex formed in the cavity. The computed values are compared again with [38] and to those obtained by Ghia [47]. In this last work, a multigrid solver related to a vorticity-stream function formulation is employed. In LB, since that the primary variables are the PDFs, the stream function can be obtained by integrating the velocity component. Once again, the agreement is encouraging and the performance of BBK is very close to that of ModBBK scheme. To evaluate the accuracy of the different boundary conditions, a series of tests with $Re = 1000$ and three different meshes have been conducted: *coarse* (65×65), *medium* (129×129) and *fine* (257×257); the accuracy is evaluated using the formula [48]:

$$n \approx \frac{\log\left[\left(\sum \mid \phi_{2h} - \phi_{4h} \mid /N\right)\left(\sum \mid \phi_{h} - \phi_{2h} \mid /N\right)\right]}{\log(2)} \tag{3.48}$$

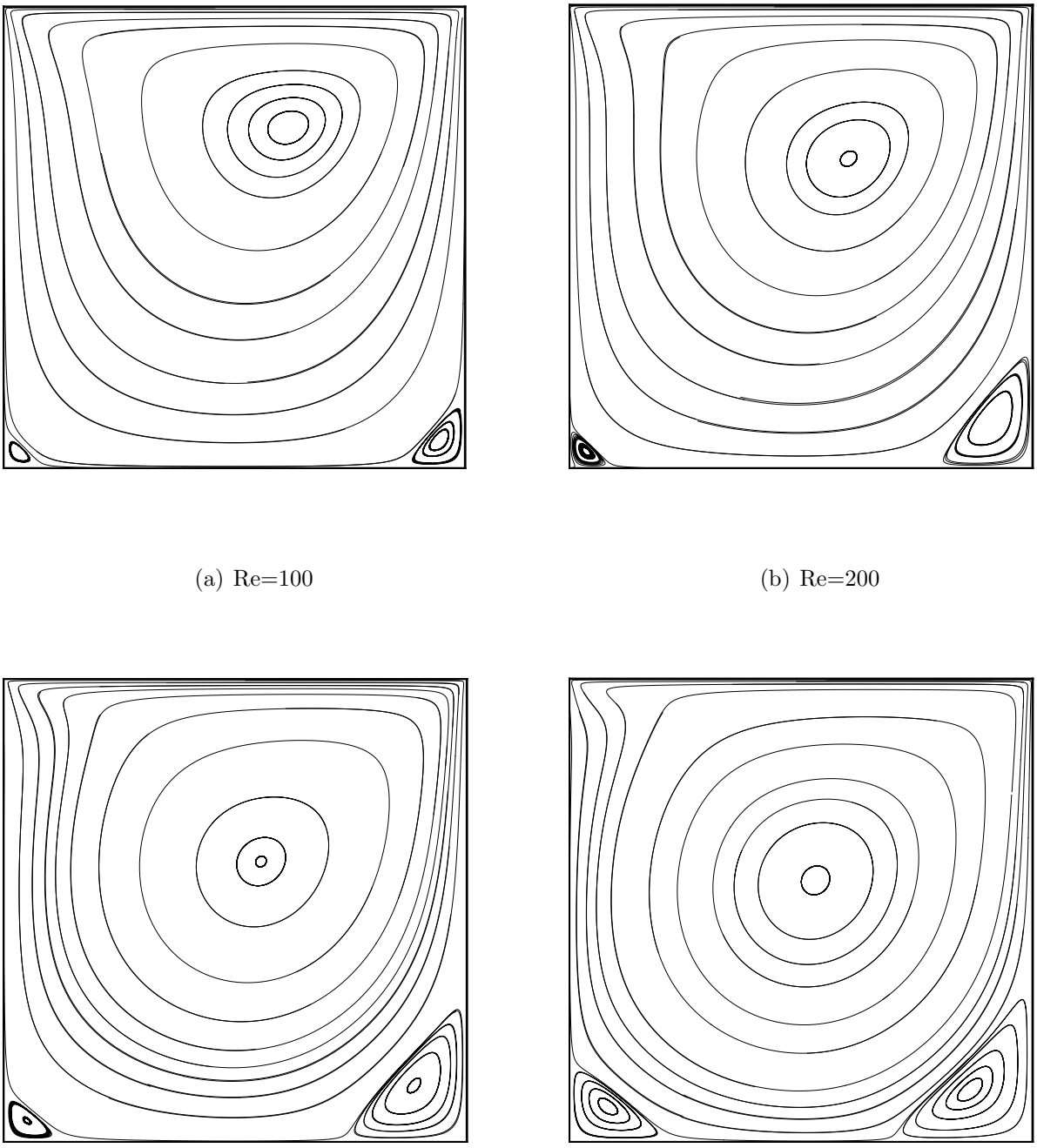

(a) Re=100

(b) Re=200

(c) Re=400

(d) Re=1000

Figure 3.10: Streamlines computed for the different cases.

Re		Ψ_c	x_c	y_c	$\Psi_l(\times 10^4)$	x_l	y_l	$\Psi_r(\times 10^3)$	x_r	y_r
100	a	0.1034	0.6172	0.7344	-0.0175	0.0313	0.0391	-0.0125	0.9453	0.0625
	b	0.1030	0.6196	0.7373	-0.0172	0.0392	0.0353	-0.0122	0.9451	0.0627
	c	0.1031	0.6192	0.7370	-0.0173	0.0390	0.0355	-0.0124	0.9451	0.0626
	d	0.1036	0.6180	0.7365	-0.0183	0.0365	0.0397	-0.0120	0.9448	0.0625
400	a	0.1139	0.5547	0.6055	-0.142	0.0508	0.0469	-0.645	0.8875	0.1188
	b	0.1121	0.5608	0.6078	-0.130	0.0549	0.0510	-0.619	0.8902	0.1255
	c	0.1122	0.6192	0.6078	-0.132	0.0547	0.0511	-0.621	0.8902	0.1257
	d	0.1144	0.6180	0.6060	-0.140	0.0503	0.0478	-0.624	0.8870	0.1199
1000	a	0.1179	0.5313	0.5625	-2.31	0.0859	0.0781	-1.75	0.8594	0.1094
	b	0.1178	0.5333	0.5647	-2.22	0.0902	0.0784	-1.69	0.8667	0.1137
	c	0.1178	0.5334	0.5645	-2.22	0.0900	0.0784	-1.66	0.8664	0.1135
	d	0.1176	0.5320	0.5630	-2.28	0.0870	0.0777	-1.80	0.8603	0.1115

Table 3.4: Vortex centres: values of stream function and coordinates for respectively primary central vortex (c), lower left (l) and lower right ones (r) . a) Ghia. b) Hou et *al.*. c) Present study with BBK. d) Present study with ModBBK

In equation (3.48), ϕ represents the quantity considered to test the accuracy, in this case the u-component of velocity; ϕ_h, ϕ_{2h} and ϕ_{4h} are respectively the value of u on fine, medium and coarse grids, with lattice space doubled each time. An accuracy of 1.8 has been found for ModBBK scheme, while the simple BBK achieves 1.40. That result is consistent to what was found by Lai et *al.* [49]. Here the same test to verify the accuracy was performed, but the BBK scheme was compared to that developed by Mei, Luo and Shyy [50] for curved boundaries. As previously observed, the first-order accuracy for BBK scheme was analytically demonstrated just for fully developed channel flows. What is found here suggests BBK can still be a good compromise between accuracy and ease in implementation and versatility. Besides, this last series of tests demonstrates that it is not necessary to use too finer

a grid to accurately describe the flow field.

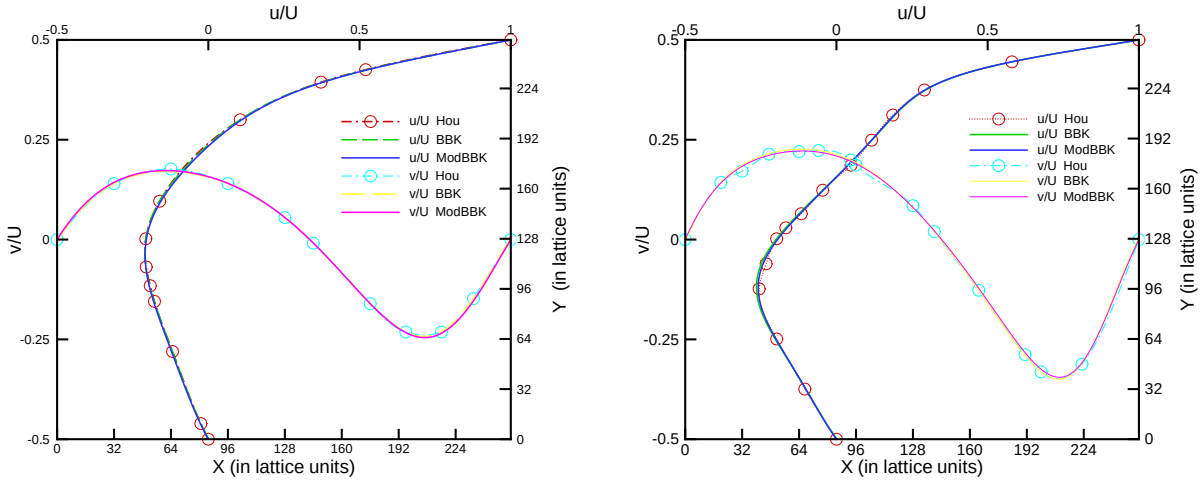

(a) Re=100

(b) Re=200

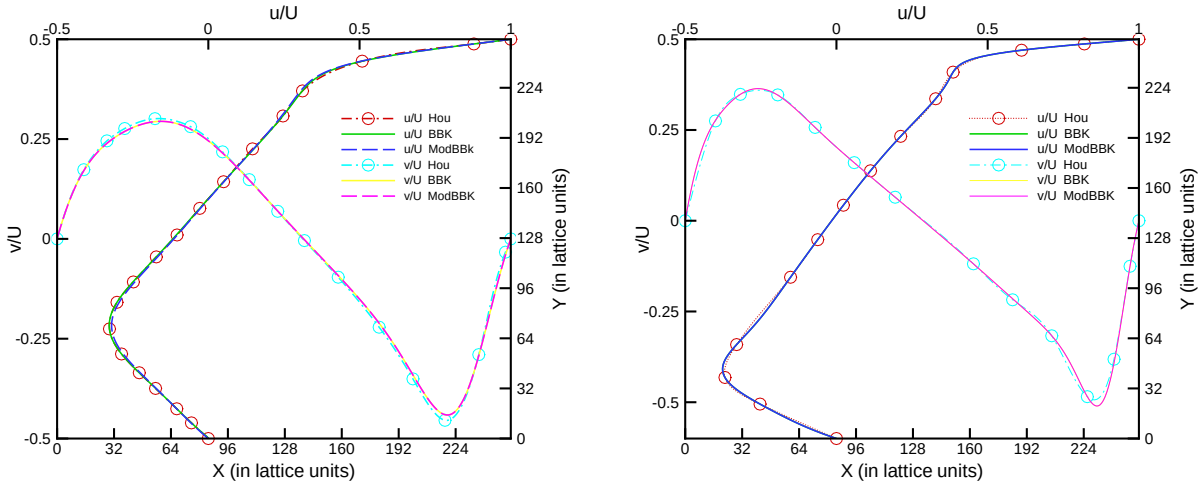

(c) Re=400

(d) Re=1000

Figure 3.11: Non-dimensional profiles of velocity components along the symmetry planes of the cavity, for the different cases, computed using BBK and ModBBk for solid walls, and compared to benchmark test by Hou et *al.*.

In the previous sections the LB was shown to be a weakly compressible method. This compressibility error has been evaluated conducting a series of dedicated tests

with Reynolds number constantly equal to 100. To represent the compressibility, the *mean variation of density*, defined as:

$$\bar{\rho} = \frac{\sum_i \rho(\mathbf{x}_i, t)}{N}, \tag{3.49}$$

is computed, with N representing the total number of lattice nodes. The average variation of density across the lattice is given by:

$$\Delta = \frac{1}{\bar{\rho}} \sqrt{\sum (\rho - \bar{\rho})^2 / N}. \tag{3.50}$$

This quantity is evaluated with three different speeds of the moving wall, namely $U_0 = 0.1, 0.05$ and 0.01, and its values are listed in Table 3.5, along with the Mach number . The table shows that:

U	0.1	0.05	0.01
Ma	0.173	0.0867	0.0173
$\Delta(\times 10^3)$	2.0	0.74	0.056

Table 3.5: Density fluctuation (Re=100).

$$\Delta(U_c = 0.05) \approx \frac{1}{4}\Delta(U_c = 0.1) \tag{3.51a}$$

$$\Delta(U_c = 0.01) \approx \frac{1}{25}\Delta(U_c = 0.05). \tag{3.51b}$$

The values found are in agreement with those stated in [51].

Chapter 4

Multi-Phase lattice Boltzmann

So far, this thesis has only dealt with single-phase, single component LB. Nevertheless, it is just in simulating multiphase/multicomponent flows that LB shows its true potential. Multiphase flows are ubiquitous in nature and are fundamental in many industrial applications. Gas-liquid flows as well as particle flows are characterized by surface forces developing at the molecular level. The accuracy of a numerical scheme in simulating such flows depend on how these interfacial interactions are incorporated into it. For classic CFD solvers it may prove very difficult to deal with applications involving sharp interfaces (which means the interface tickness is negligible when compared with the characteristic length scale associated to the motion of the bulk fluids) often changing topologically in time or characterized by high density or concentration gradients. Additional averaged terms have to be inserted in NS equations, increasing the complexity, while for a method originating from a microscopic description of fluids, like LB, the task can be definitively easier. Molecular dynamics can be a valid alternative, only on extremely small time and length scales because of computational cost.

Since the appearance of LB, twenty years ago, many multiphase models have been proposed. This chapter is concerned with one of the oldest, but nevertheless still one of the most used of these schemes: the Shan-Chen (SC) multiphase model [52] for liquid/gas flows. This chapter opens with some remarks on the behavior of nonideal fluids, followed by the description of the SC model; then some results related to two cases, the single droplet under microconfined shear flow and he T-

shaped micromixer are presented. Since these flows are both multicomponent, the extension defined in [53] will be also reviewed briefly. In both cases, the theory presented is related to the original formulation of the model, adapted to nonregular lattice structures $\mathcal{L}$. The limitations of this implementation are listed in the last part of the chapter, together with a review of other multiphase LB models.

4.1 Non-ideal fluids

An ideal gas is a theoretical gas composed of a set of randomly-moving, non-interacting point particles. The ideal gas concept is useful because it obeys the ideal gas law, a simplified equation of state, and is amenable to analysis under statistical mechanics. At normal ambient conditions such as standard temperature and pressure, most real gases behave qualitatively like an ideal gas. Generally, deviation from an ideal gas tends to decrease with higher temperature and lower density, as the work performed by intermolecular forces becomes less significant compared with the particles' kinetic energy, and the size of the molecules becomes less significant compared to the empty space between them.

The ideal gas model tends to fail at lower temperatures or higher pressures, when intermolecular forces and molecular size become important. At some point of low temperature and high pressure, real gases undergo a phase transition, such as to a liquid or a solid. The model of an ideal gas, however, does not describe or allow phase transitions. These must be modeled by more complex equations of state, although it is important to remember that presently there is no single equation of state that accurately predicts the properties of all substances under all conditions. Probably the most famous equation of state is the van der Waals (vdW) :

$$p = \frac{\rho RT}{1 - b\rho} - a\rho^2. \tag{4.1}$$

Equation (4.1) is an example of cubic EOS, which means when expanded has volume terms raised to the first, second, and third power. Most commonly encountered phase equilibrium calculations, such as vapour-liquid equilibria, involve only two phases for which a cubic equation is suitable. Cubic equations have the advantage that the three values of volume can be obtained analytically without the need for an iterative solution procedure. The parameters a and b measures respec-

tively the attractive forces between the molecules and the repulsive effect due to the molecular size. For a given EOS it is interesting to plot the isotherms at different temperatures. It can be seen that there exists a temperature $T_c = (8a/27Rb)$ above which the isotherms do not look much different from those for the ideal gas. However, at T = Tc the isotherm develops an inflection point at ($p_c = a/27b^2$, $\rho_c = 1/3b$). Finally, for $T < T_c$ the $p(\rho)$ curve becomes non-monotonic. The point (p_c, ρ_c, T_c) defines the *critical point* of the liquid gas transition. Above the critical point liquid and gas phases cannot be distinguished. It is useful at this point to introduce the so-called *reduced variables* $\rho_R = \rho/\rho_c$, $p_R = p/p_c$ and $T_R = T/T_c$ so that all liquid gas systems should look the same in these reduced variables. Figure 4.1 reports the isotherms $p_R(\rho_R)$ of the vdW EOS at different reduced temperatures. Other EOS possess isotherms with similar shapes.

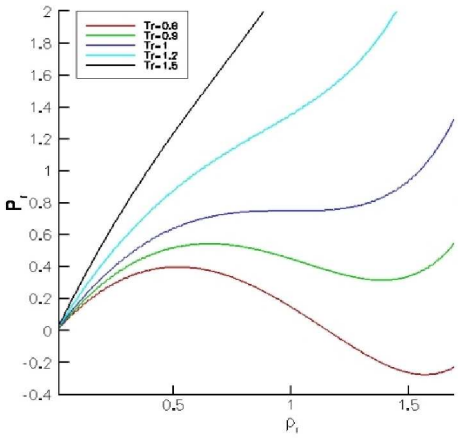

Figure 4.1: Isotherms related to the vdW EOS at different reduced temperatures.

The isotherm for $T_R = 0.9$ is evidenced in Figure 4.2b. It is clear that the red portion of the curve is linearly unstable since $(\partial p/\partial \rho) < 0$. That means a this portion of the isotherm must be unphysical [54]. It is interesting to plot the dependance of the molar Gibbs potential on the pressure at constant T. This potential can be computed from the Gibbs-Duhem relation, here rewritten in terms of the specific density:

$$d\mu = -sdT + \rho^{-1}dp, \tag{4.2}$$

where s is the specific entropy. Integrating equation (4.2) at constant temperature and knowing the value of the potential in a point A of the curve it is possible to compute the value of μ in every other point:

$$\mu_B - \mu_A = \int_A^B \rho^{-1}\, dp. \tag{4.3}$$

Equation (4.3) is represented in Figure 4.2b. Examining these figures it is possible to see that for $p < p_B$ and $p > p_H$ the density of the system is unique at a given pressure, while for $p_B < p < p_H$ there are potentially three states corresponding to the same pressure: of course the system cannot stay in the unphysical region, while among the two remaining states the system takes the one characterized by the minimum μ. Points C and G possess the same value of the potential as it can be seen in Figure 4.2b: *only at this pressure two states of the system (liquid and gas phases) can coexist.*

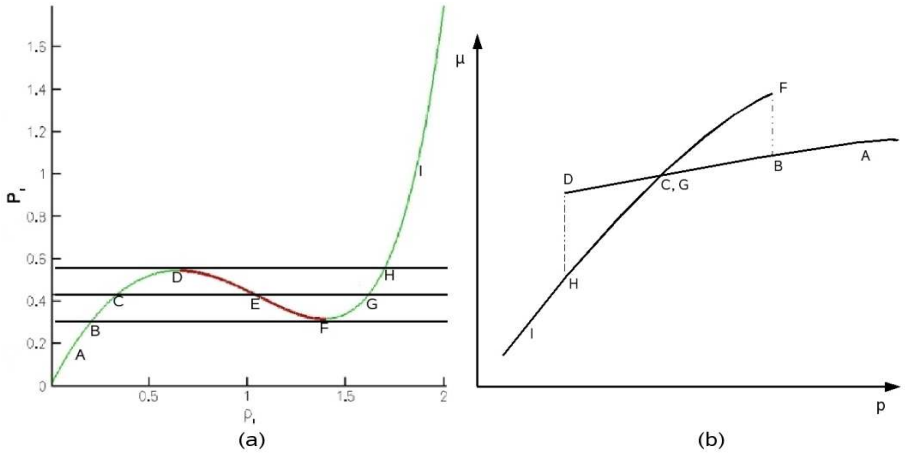

Figure 4.2: (a) vdW isotherm at $T_R = 0.9$. (b) Isothermal dependence of the molar Gibbs potential on pressure at $T_R = 0.9$.

At every temperature is therefore possible to determine this unique pressure and the corresponding densities, obtaining the so-called *coexistance curve*. Below p_C the system takes the densities indicated by the branch AC of the isotherm (gas phase), while above p_C the system takes the densities related to the branch CI (liquid phase). Since $\mu_C = \mu_G$ from equation (4.3) it follows that areas indicated by closed regions CDE and EFG are equal. The physical isotherm is therefore

obtained after this *equal area* (or Maxwell) construction is applied to the original curve and is represented in Figure 4.3.

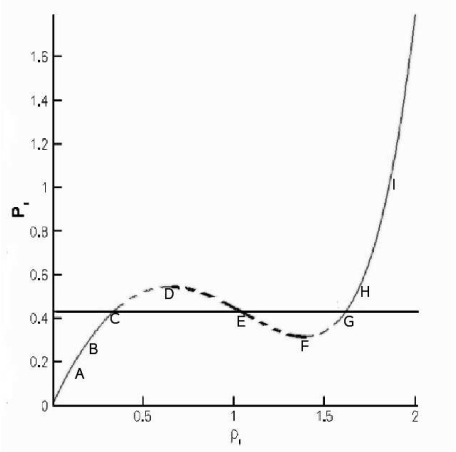

Figure 4.3: Physical vdW isotherm at $T_R = 0.9$ after the equal-area construction.

4.2 The Shan-Chen Model

In chapter 3 it has been shown that the standard LB formulation simulates incompressible NS with an ideal EOS (3.12). In order to study multiphase flows nonideal effects have to be considered. The SC model consists in expressing the interparticle interactions via a specific force computed as the gradient of a scalar potential:

$$\mathbf{F} \approx c_s^2 \psi \mathcal{G} \boldsymbol{\nabla} \psi(\mathbf{x}, t). \tag{4.4}$$

The SC model depends substantially on three elements: the scalar ψ, the constant $\mathcal{G}$ and the way in which its gradient is computed on $\mathcal{L}$. The first element, ψ is referred to as the *effective mass* and depends on the local value of macroscopic density, $\psi(\mathbf{x}, t) = \psi(\rho(\mathbf{x}, t))$. A typical choice ([52], [55] or [56]) is :

$$\psi = \rho_0 \left[1 - exp(-\rho/\rho_0)\right], \tag{4.5}$$

where ρ_0 is a normalization constant usually set equal to unity. This form of the effective mass reduces to the density ρ in the limit $\rho \ll 1$, whereas at high density ($\rho \gg 1$), it shows a saturation. This latter is crucial to prevent density

collapse of the high-density phases: infact the SC potential is purely attractive, so that a mechanism stabilizing the high-density phase is mandatory to prevent density collapse. This form is therefore quite empirical and will be shown later not able to achieve high density ratios. This issue will be addressed in chapter 6. The constant $\mathcal{G}$ is termed the *coupling constant* and, as it will be shown in subsequent sections, it plays the role of temperature. Concerning the numerical evaluation of the gradient appearing in (4.4) many different finite difference schemes are possible in principle. Generally speaking one has to choose a certain number N of lattice nodes $\mathbf{y}_i|\{i = 1 \dots N\}$ surrounding $\mathbf{x}$; say $\mathbf{c}_i = \mathbf{x} - \mathbf{y}_i|\{i = 1 \dots N\}$, the next step is to define a set of coefficients $w(|\mathbf{c}_i^2|)$ weighting the contributions of the different nodes, bearing in mind some constraints:

- To preserve isotropy the sites must be symmetrical about all the axis.
- Closer sites must have a bigger influence than far ones.
- The weighting factors $w(|\mathbf{c}_i^2|)$ must be chosen so to build *at least* 4-th order isotropic lattice tensors.

The scheme most commonly adopted allows the computation of the gradient of a generic scalar ϕ considering only the nearest and next-nearest sites to $\mathbf{x}$ [57]:

$$\partial_\alpha \phi(\mathbf{x}, t) = \sum_{i \neq 0} \frac{w_i \mathbf{e}_i \cdot \hat{\boldsymbol{\alpha}} \left[\phi(\mathbf{x} + \mathbf{e}_i) - \phi(\mathbf{x} - \mathbf{e}_i)\right]}{2c_s^2}. \tag{4.6}$$

The most general form of (4.4) is therefore given by:

$$F_\alpha(\mathbf{x}, t) = -c_s^2 \psi(\mathbf{x}, t) \sum_i w(|\mathbf{c}_i^2|) \mathcal{G} \psi(\mathbf{x} + \mathbf{c}_i, t) \, c_{i\alpha}. \tag{4.7}$$

The standard way of incorporating the effect of F into the LB is to alter the macroscopic speed appearing in (3.8) via method I explained in the previous chapter ((3.25)):

$$\mathbf{u}^{eq} = \mathbf{u} + \frac{\tau}{\rho} \mathbf{F} \tag{4.8}$$

The macroscopic momentum is computed via (3.20). It is important to observe that while the mass is always conserved by the collision operator, local momentum

is not preserved anymore, and that this momentum variation between pre- and post-collisional states is just given by the interparticle force:

$$\sum_i \Omega_i e_{i\alpha} = \sum_j F_\alpha. \tag{4.9}$$

Total momentum is still conserved. The EOS associated to the SC model is:

$$p = \rho c_s^2 + \frac{c_s^2}{2}\mathcal{G}\left[\psi^2(\rho)\right]. \tag{4.10}$$

To model wettability phenomena or multiphase flows in porous media it is necessary to incorporate fluid/surface interactions. That can easily be done in the SC framework [58], introducing another force term similar to what defined in equation (4.7):

$$\mathbf{F}_w(\mathbf{x}) = -\psi(\mathbf{x})\sum_i w(|\mathbf{c}|_i^2)\mathcal{G}_w\psi_w(\mathbf{x}+\mathbf{c}_i)\mathbf{c}_i, \tag{4.11}$$

where $\mathcal{G}_w$ is another coupling constant allowing this time to control the contact angle, while ψ_w is just a switch being one if $\mathbf{y}_i = \mathbf{x} + \mathbf{c}_i$ belongs to a solid surface. With this scheme either wetting (setting $\mathcal{G}_w < 0$) or unwetting (setting $\mathcal{G}_w > 0$) fluids can be modelled. Analytical expressions of the contact angle determined by SC model can be found in [59] or [60].

4.3 Meaning of the Coupling Constant

The performance of a multiphase model can be evaluated examining how the model reproduces the interface evolution in time. Ideally, the model should produce isotropic interfaces; concerning the thickness, it is certainly not possible to obtain the values in the order of Angstroms typical of physical interfaces, but nevertheless the principle is that smaller is better. Most of all the model should be able to attain phase separation at temperatures below the critical level. Besides, the pressure difference computed at interfaces should be consistent with the Laplace law. In this section the SC model is demonstrated to fulfil such requirements.

In what follows, equation (4.5) with $\rho_0 = 1.0$ is chosen as effective mass; by plotting $p - \rho$ curves at different values of $\mathcal{G}$ the temperature-like behaviour of the

coupling constant can be clearly seen [61]. Given $\mathcal{G}$ below a certain "critical" value $\mathcal{G}_c$ there coexists two densities at the same pressure. The determination of the critical values for density and coupling constant proceeds exactly as for any other EOS: by solving the system $\partial_\rho p|_{T=T_c} = \partial^2_{\rho^2} p|_{T=T_c} = 0$ one finds that $\rho_c = \ln 2$ and $\mathcal{G}_c = -2/9$, making evident that $T = -1/\mathcal{G}$. By measuring the liquid-gas densities on the opposite sites of a flat interface at a given $\mathcal{G} < \mathcal{G}_c$ it is possible to build the coexistence curve related to the SC-EOS [62]. The equilibrium densities ρ_g and ρ_l are reported in Figure 4.4 together with the corresponding density ratio, which

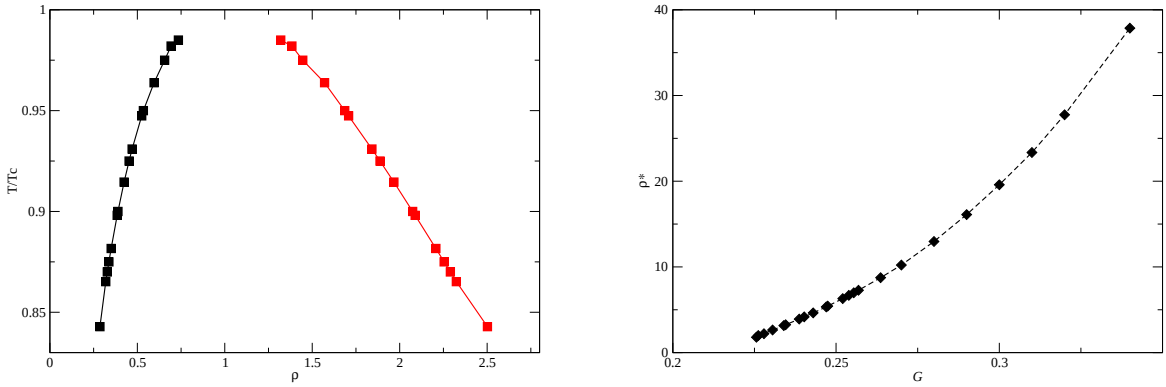

(a) (b)

Figure 4.4: Coexistence curve and density ratios for SC with EOS given by (4.10).

A 100×100 fully periodical domain is filled by a fluid modelled with equation (4.10) with the adding of a small amount of fluctuating noise [10]: $\psi(\rho) = \psi(\sum_i f_i + \nu\xi)$, where ν is a random value in $[-1, 1]$ and $\xi = 0.001$ is the noise. The "temperature" is $\mathcal{G} = -5.5$ with uniform initial density $\rho_g < \bar{\rho} < \rho_l$. The relaxation time is $\tau = 1.0$. Letting the simulation run for about 1200 time steps a complete phase separation can be observed, as reported in Figure 4.5. Here liquid and gaseous phases are reported respectively in red and blue. The system finally reaches a minimum energy configuration with the remaining of only one rounded bubble surrounded by liquid. Different tests have been conducted at different noise levels, resulting in phase separation even at $\xi = 1E^{-6}$ (of course reducing the noise level increased the time necessary to observe separation), while the flow was unstable for $\xi > 0.01$.

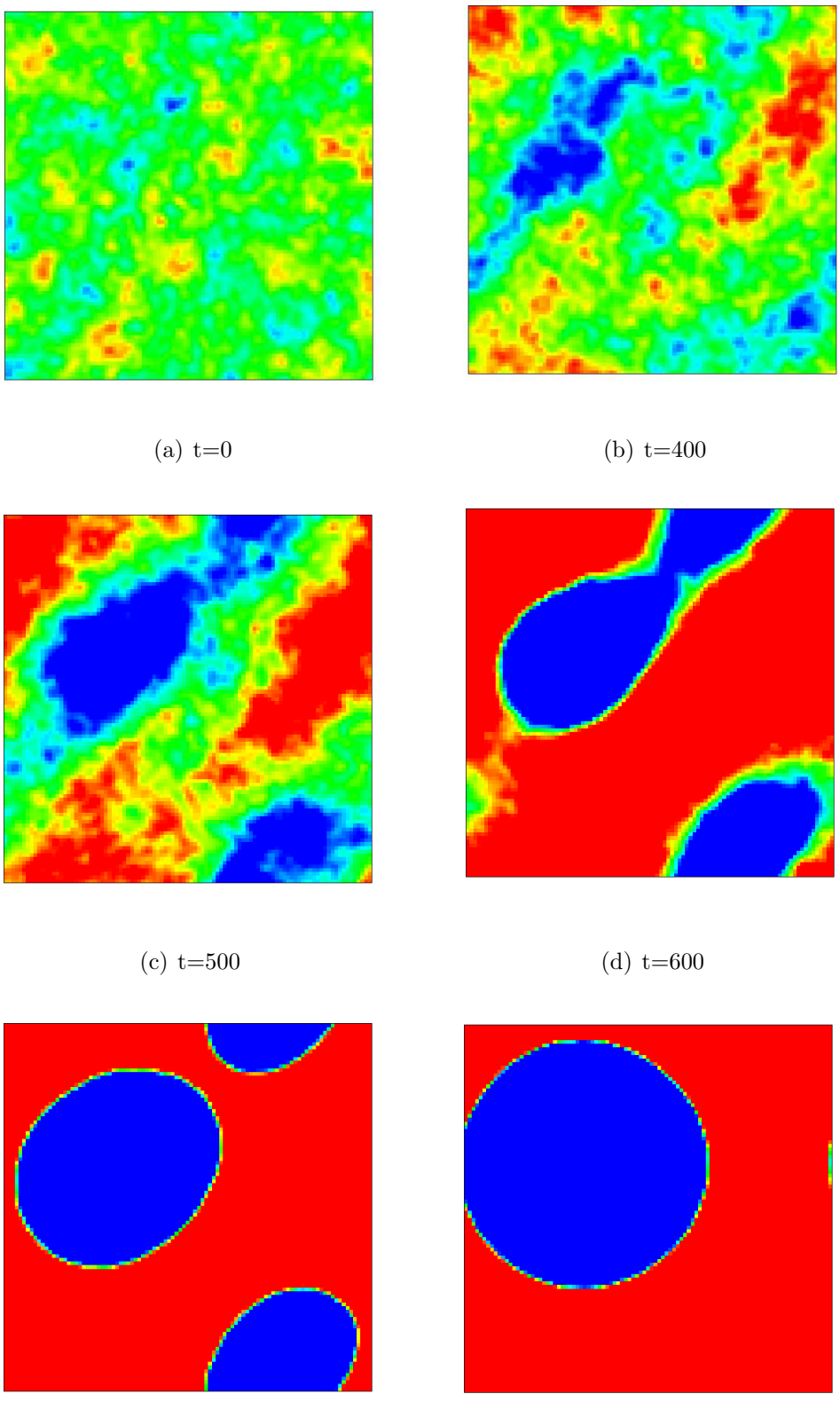

(a) t=0 (b) t=400

(c) t=500 (d) t=600

(e) t=700 (f) t=1200

Figure 4.5: Time evolution of phase separation process. $\mathcal{G} = -5.5$.

The next case considered concerns a single static liquid droplet surrounded by vapour. The grid is 51×51×51 and periodic BC are again employed. D3Q19 model is adopted. The droplet has initial radius $R_i = 12$ and is placed at the centre of the domain. The test run till a 3D equivalent of the convergence condition (3.40) was satsfied. The coupling constant and the relaxation time takes the same values seen before, while the droplet and vapour are initialized with the equilibrium densities obtained by the coexistence curve. The final configuration of the bubble can be viewed in Figure 4.6, where the small interdiffusion region close to the interface can be appreciated. The velocity field should ideally be zero everywhere. The simulation instead produces not-negligible velocities in the interfacial region, which are referred to as *spurious currents*. These unphysical currents increase with the density ratio till they cause the simulation to blow up: their reduction is therefore crucial in order to achieve high density ratios like those encountered in real gas-liquid flows. Besides, when considering moving objects like for instance colliding droplets it is important that the measured velocity field is not "polluted" by spurious currents: since the characteristic speed has always to respect the low-Mach constraint, it can be really hard to distinguish between physical and unphysical velocities. The maximum values of spurious currents module will be indicated here and in what follows as $|\mathbf{u}|_s$. In this particular case, with $\mathcal{G} = -5.9$ a value of $|\mathbf{u}|_s = 0.025$ was measured. Further tests conducted at $G = -5$, $G = -6.5$ and $G = -7$ resulted in $u|_s$ respectively equal to 0.0063, 0.04 and 0.0915, while the case $G = -7.5$ was unstable.

Evaluating the pressure values far from the interface and the corresponding density gradients, it is possible to determine the surface tension from Laplace's law:

$$p_i - p_o = \frac{\sigma}{2R_f}. \tag{4.12}$$

Different initial radii have been tested $(10, 12, 14, 16, 18)$, and the pressure jump has been computed, together with the final radius, for every test. As it is possible to see in Figure 4.7 the computed points fit a straight line quite well, therefore the Laplace's law is correctly approximated.

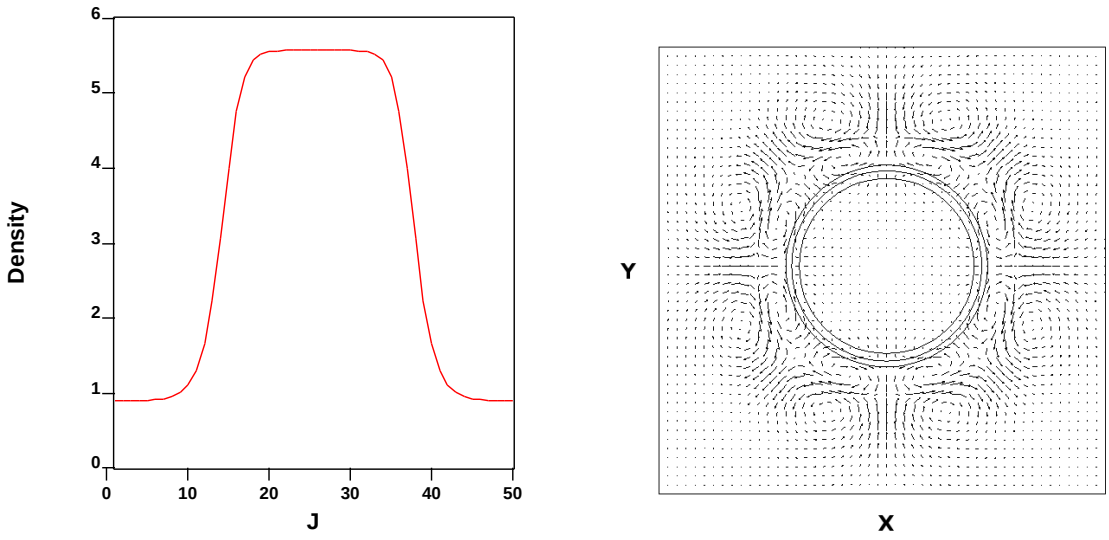

(a) (b)

Figure 4.6: a) Density profile on x=25 and z=25. b) Velocity vectors and density conturs in the xy plane at z=25.

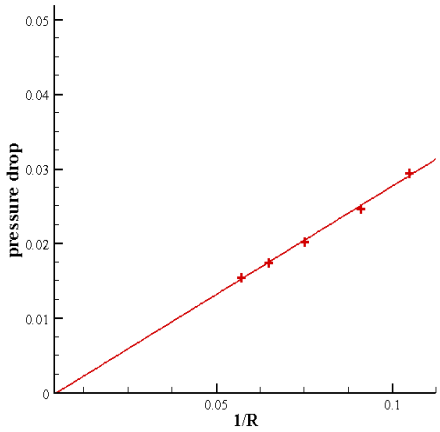

Figure 4.7: Test of Laplace's law

4.4 Extension to multicomponent flows

In a multicomponent flow different sets of f_i^j and $f_i^{j,eq}$ have to be defined for each species $j|\{0 \dots N_s - 1\}$, as well as different SRT "stream and collide" equations like (3.4):

$$f_i^j\left(\mathbf{x} + \mathbf{e}_i \Delta t, t + \Delta t\right) - f_i^j\left(\mathbf{x}, t\right) = -\frac{1}{\tau^j}\left(f_i^j\left(\mathbf{x}, t\right) - f_i^{j,eq}\left(\mathbf{x}, t\right)\right). \tag{4.13}$$

In equation (4.13) τ^j represents the relaxation time characterizing the j-th species. The interparticle force this time has also to take into account interactions among different components:

$$\mathbf{F}_\alpha^j(\mathbf{x}) = -c_s^2 \psi^j(\mathbf{x}) \sum_i \sum_{\bar{j}} w(|\mathbf{c}|_i^2) \mathcal{G}_{j\bar{j}} \psi^{\bar{j}}(\mathbf{x} + \mathbf{c}_i) \mathbf{c}_{i\alpha}, \tag{4.14}$$

The coupling constant turns out to be a *coupling matrix* this time, with $\mathcal{G}_{j\bar{j}} = \mathcal{G}_{\bar{j}j}$. The interaction strength between species j and $\bar{j}$ is controlled by $\mathcal{G}_{j\bar{j}}$, which has to be positive in order to enforce separation between them. A common choice of the effective mass for multicomponent flows is $\psi^j = \rho^j$ [63]. For each species it is possible to evaluate the momentum change produced by the corresponding force computed by equation (4.14) like for the single fluid case:

$$\mathbf{u}^{j,eq} = \mathbf{u}' + \frac{\tau^j}{\rho}\mathbf{F}, \tag{4.15}$$

where $\mathbf{u}'$ represents an *average speed* :

$$\mathbf{u}' = \frac{\sum_j \frac{m^j}{\tau_j} \sum_i f_i^j \mathbf{e}_i}{\sum_j \frac{m^j}{\tau_j} \sum_i f_i^j}. \tag{4.16}$$

The total density at any lattice site is intuitively computed adding the densities of the single species. The macroscopic momentum is computed by making the average between the pre- and post-collisional states:

$$\rho u_\alpha = \sum_i f_i^j e_{i\alpha} + \frac{1}{2}\sum_j F_\alpha^j, \tag{4.17}$$

Finally, the kinematic viscosity computed by the SC model with multiple component is given by:

$$\nu = c_s^2 \sum_j \chi^j \left(\tau^j - \frac{1}{2} \right), \tag{4.18}$$

where $\chi^j = \rho^j / \sum_j \rho^j$ represents the local value of the mass fraction for j-th species.

4.5 Droplet deformation in microconfined shear

The deformation and breakup of a droplet immersed in a liquid matrix and confined in a microscopical geometry are fundamental in many microfluidic applications [64]. Despite that the this kind of flow has received less attention than the unbounded case, where the moving walls are far enough from the droplet to consider the flow as characterized by only one length scale, the radius of the undeformed droplet R. This assumption, together with the Newtonian nature of continuous and drop phases, is the basis of the theory of Taylor, according to which the flow regime is completely governed by two nondimensional quantities: the capillary number Ca, which represents the ratio between shear and interfacial stresses, and the viscosity ratio λ between the droplet and the continuous phase. Given $\dot{\gamma}$, μ, ρ and σ respectively the shear rate, the continuous phase viscosity, density and the surface tension, it is possible to define the capillary number and the Reynolds number respectively as $Ca = R\mu\dot{\gamma}/\sigma$ and $Re = \rho R^2\dot{\gamma}/\mu$. To consider wall effects one more nondimensional quantity has to be defined, the gap R/H where H is half of channel height in the velocity gradient direction. In [65] a systematic study of this flow is reported: the two higly viscous Newtonian liquids (polybutene for the continuous phase and a mixture of silicone oils for the dispersed phase) have $\lambda \approx 1$ and nearly the same density, so that buoyancy effects can be neglected. The deformation of the droplet is observed at different shear rates and gaps, observing an increased deformation as the gap is reduced. The wall influence is here studied with the LB and the multicomponent SC model. In order to conveniently reproduce the experiments in [65], the two fluids the have same densities $\rho_1 = \rho_2 = 0.3$ and viscosities $\tau_1 = \tau_2 = 1.5$, while the coupling matrix is given by $\mathcal{G}_{11} = \mathcal{G}_{22} = 0$ and $\mathcal{G}_{12} = \mathcal{G}_{21} = 10$. The effective mass

for each species is chosen as the density: $\psi^j = \rho^j$. By means of a static droplet test the surface tension σ was computed. Three dimensional simulations were conducted using the $D3Q19$ model, and the ZH boundary condition for the moving walls. The Ca and R/H were varied in the range $0.1 - 0.2$ and $0.16 - 0.4$, and the droplet radius R correspondingly varied from 8 to 20 in lattice units. For each configuration the deformation was evaluated as $D = \frac{L-B}{L+B}$, where L and B are respectively twice the maximum and minimum distancies occurring from the droplet centre to its border. Figure 4.8 illustrates the effect of reducing the gap R/H at constant Ca. The droplet is more elongated in because of the increased velocity gradient at the extremes. Comparing the velocity flow field inside the droplet it is possible to observe one vortical swirl occupying the whole droplet in case (a), while in (b) the top and bottom are interested by two swirls because of increased inertial effects.

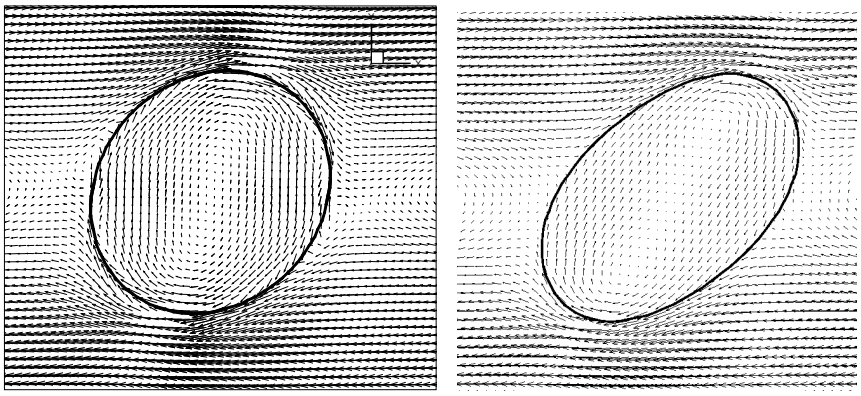

(a) (b)

Figure 4.8: Drop under microconfined shear flow at Ca=0.1 and (a) R/H=0.18; (b) R/H=0.18.

Figure 4.9 compares the LB simulations with the predictions from the analytical model developed in [2] for all the studied cases. The deformation D was measured once the steady state had been reached. Oscillations were reported at high Reynolds numbers [66], but that is not the case here, because $Re \ll 1$. For both $Ca = 0.1$ and $Ca = 0.2$ the average difference is 3%, demonstrating the validity of the LB. A further reduction of the gap causes the droplet to assume extremely elongated shapes, more oriented on the flow direction. An unstable case is summarized by Figure 4.10, corresponding to $Ca = 0.46$ and $R/H = 0.7$. It is possible to observe the the double pinch-off at the ends of the neck region. The comparison with Figure

3 from [65] demonstrates the LB correctly reproduces the process. As reported in the experiments, the daughter droplets have almost the same size, suggesting the microconfined shear flow can be used to generate monodisperse emulsions.

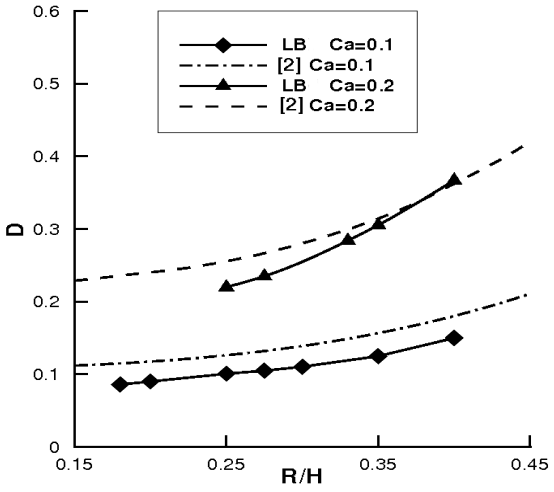

Figure 4.9: Comparison of droplet deformation at different confinements between LB and the predictions of [2] at $Ca = 0.1$ and $Ca = 0.2$.

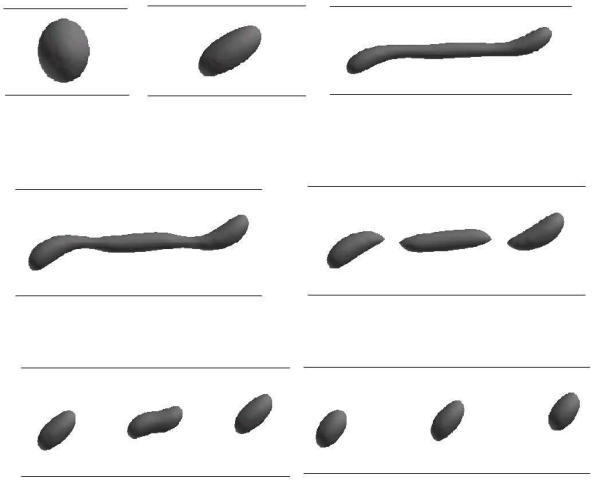

Figure 4.10: Drop breakup at $Ca = 0.46$ and $R/H = 0.7$. For the sake of clarity the walls are depicted too.

4.6 The T-shaped Micromixer

The mixing of two fluids is an essential process in many microfluidic devices employed in biomedical and biochemical processes like DNA purification, polymerase chain reaction (PCR), protein folding and enzyme reaction. The performance of these processes relies on rapid (order of milliseconds) and effective mixing of samples and reagent flowing in microchannels. The design of such a device has to take into account the limitations induced by the particular flow regimes occurring at microscales. Since typically $Re < 1$, microflows are laminar. The NS equation is reduced to (3.31). Turbulence cannot be used to promote mixing, which instead relies on intermolecular diffusion and convection, both characterized by a specific time scale. If l is the length characterizing the mixing process, $\bar{U}$ the mean speed in the microchannel and D_{12} the mutual diffusion coefficient of the couple of fluids considered, the time scales for diffusive and convective mixing t_D and t_C, are respectively [67] [68]:

$$t_D = \frac{l^2}{2D_{12}} \tag{4.19a}$$

$$t_C \approx \frac{l}{\bar{U}}. \tag{4.19b}$$

The ratio between t_C and t_D is expressed by the Peclet number Pe:

$$Pe = \frac{l\bar{U}}{D_{12}}. \tag{4.20}$$

Finally, the channel length L_m is given by:

$$L_m = \bar{U} \times t_D = Pe \times l \tag{4.21}$$

The evaluation of these quantities for real problems shows the difficulties in the design of a micromixer: diffusion in fact is quite a slow process, and a time for complete mixing in the order of milliseconds can be achieved only if l amounts to a few microns; if $l > 10\mu m$ diffusion is not efficient, cause L_m would get unacceptable, even because longer channels mean higher pressure gradient, with consequent problems in the design of the micropump. In other words, $l \geq 100\mu m$ and $Pe > 100$

define a field of operative conditions that necessitates some form of speed up of the mixing process that does not involve a great increase of pressure drop driving the flow, which would complicate the design of the micropump. Micromixers are commonly classified as *active* or *passive*. Active mixing is based on the supply of energy external to the device, while in passive mixing the flow energy due to pumping or hydrodynamic potential is used to restructure the flow in a way which results in faster mixing. The interested reader can find a complete review of the many different solutions proposed in the last years in [69]. In this section the focus will be on passive micromixers, and precisely on probably the simplest type: the *T-shaped micromixer*. This device is simply constituted by two inlet channels leading 2 fluid streams into a main microchannel where they flow parallel. A variant is the *Y-shaped micromixer*, in which the inlets are inclined. In order to increase the mixing efficiency of such a device, in [3] was proposed to place obstacles in the main channel of a Y-micromixer. Obstacles do not generate turbulence in the low Re flow regime characterizing the flow, but their effect is to stir the fluid creating transversal mass transport. The obstacles can be easily realized by excimer laser or silicon machining. In [3] the effect of eight diffeferent obstacle layouts on the mixing efficiency of an Y-sensor was determined by two-dimensional numerical simulations employing the commercial code MemCFD by CoventorWave ™. This approximation is acceptable when, say W and H respectively the width and the height of the main channel cross section, $W \gg H$. The fluids considered were water and ethanol at $Pe = 200$. Table 4.1 reports the main properties of these two substancies.

Fluid	Viscosity ($kg\,\mu m^{-1}s^{-1}$)	D_{12} ($\mu m^2 s^{-1}$)	Density ($kg\,\mu m^{-3}$)
Water	9.0×10^{-10}	1.2×10^{3}	9.998×10^{-16}
Ethanol	1.2×10^{-9}	1.2×10^{3}	$7.89\ \times10^{-16}$

Table 4.1: Properties of water and ethanol at 20° C.

The mixing efficiency ε_{mix} was evaluated for each configuration as in [70]:

$$\varepsilon_{mix} = \left(1 - \frac{\int_0^{2l} |\chi - \chi_\infty| dy}{\int_0^{2l} |\chi_0 - \chi_\infty| dy}\right) \times 100\%, \tag{4.22}$$

where χ is the mass concentration distribution at the outflow section, χ_∞ is the concentration corresponding to a complete mixing and χ_0 is the initial concentration

distribution. The LB with the multicomponent SC model has been tested on the same eight configurations in this study. Two-dimensional simulations where performed for all the configurations listed in Table 4.2 using D2Q9 model. To have all the boundaries perfectly aligned on the grid, the T-shaped geometry was chosen: this choice was justifid by what is reported in [71], where it was demonstrated that the inclination of the inlets has not a significant effect on the mixing efficiency. The T-sensor is depicted in Figure 4.11, in which one of the obstacle layouts fabricated and tested in [3] is also reported, while the different obstacle layouts listed in Table 4.2 are sketched in Figure 4.12. Some configurations (indicated here and in the following as "C") are *included* in others with bigger number of obstacles, and therefore are represented in red.

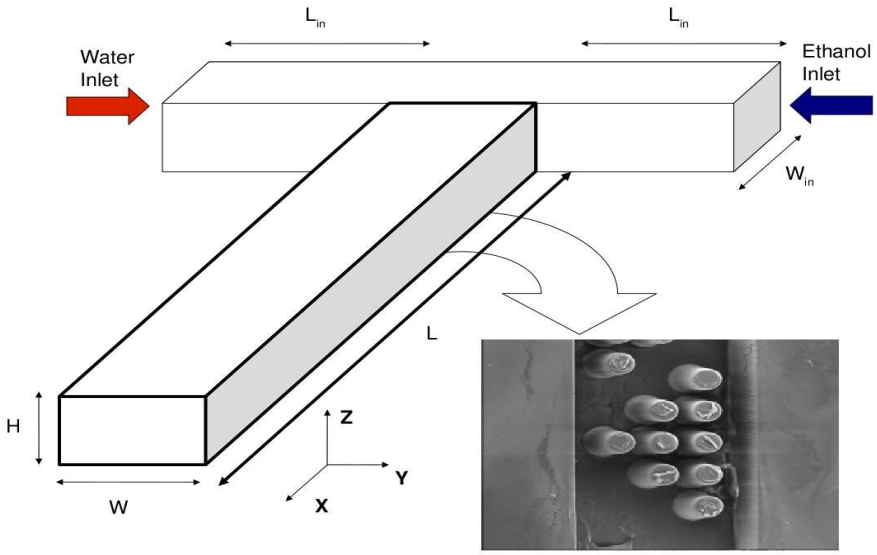

Figure 4.11: T-sensor geometry with obstacle layouts. The photographic image from [3] refers to part of one of the obstacle layouts considered in the experiments.

Configuration number	1	2	3	4	5	6	7	8
Number of obstacles	0	1	1	2	3	9	9	18

Table 4.2: Different configurations tested in [3] and in the present study.

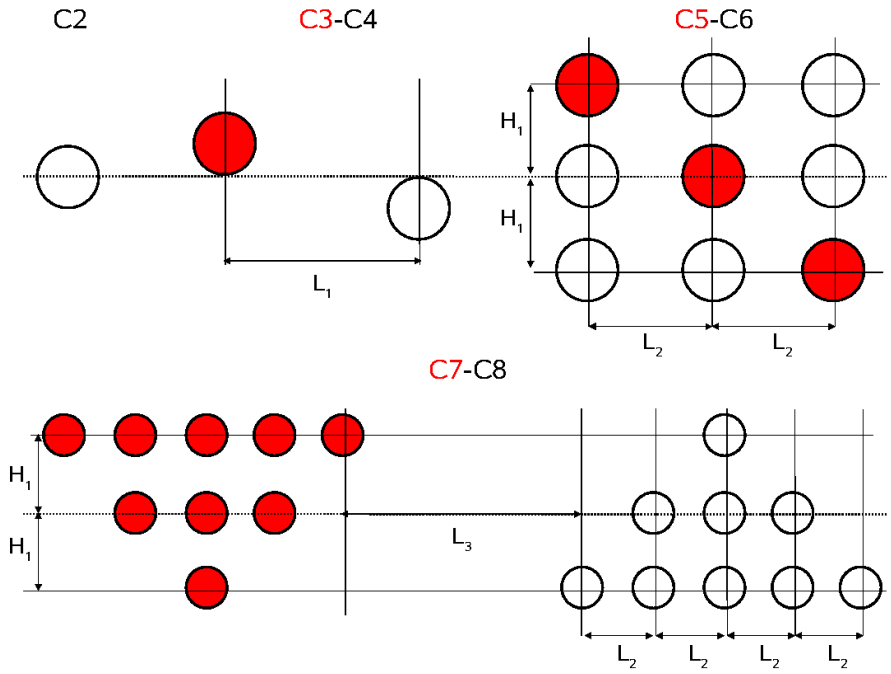

Figure 4.12: Geometry of the different configurations tested.

	L	H	W	W_{in}	L_{in}	D_{obst}	L_1	L_2	L_3	H_1
[3](μm)	1200 (2000)	100	300	200	-	60	-	100	300	90
LU	700 (1000)	-	150	100	300	30	100	50	150	45

Table 4.3: Micromixer geometrical parameters in [3] (expressed in μm) and in the present study (expressed in lattice units).

Table 4.3 compares the most relevant geometrical quantities indicated in Figures 4.11-4.12 between LB simulations and [3]; the main channel is 2mm and 1000 grid nodes long respectively in [3] and in the present study. The resulting lattice space Δx is therefore $2\mu m$, while the 2 fluids have density and viscosity ratios consistent with the properties of real fluids reported in Table 4.1. Like in the previous case, the effective mass for each species is chosen as the density: $\psi^j = \rho^j$. Once ψ and the coupling matrix elements are fixed, the diffusivity is determined by measuring the decay of a concentration wave like what was done in [55] and [72]. In order to get the desired Peclet number of 200, the coupling matrix for this case is given by $\mathcal{G}_{11} = \mathcal{G}_{22} = 0$ and $\mathcal{G}_{12} = \mathcal{G}_{21} = 1$. The BC were BBK on all obstacle surfaces and

channel walls, ZH scheme for inlet sections and extrapolation scheme described in section 3.7.2 for the outflow section. In order to evaluate the gradient in equation (4.13) with the usual isotropic scheme a "ghost" layer of nodes is placed immediately outside the outflow section: i and j are the indexes on x and y directions, the abscissas of a ghost node, outflow section node and inside node at constant j will be indicated by i, i_o and i_{o-1} respectively. The density on each node i_{o-1} is therefore extrapolated according to $\rho_i = \frac{4}{3}\rho_o - \frac{1}{3}\rho_{i-1}$. The first test intends to evaluate the dependance of the mixer efficiency on the flow rate. No obstacles are considered here. Figure 4.13 illustrates the effect of increasing fluid 1 (water) inflow speed U from 0.1 to 0.5 by showing fluid 1 (water) concentration contours. Both fluids have the same flow rate, so the inlet velocity of fluid 2 (ethanol) is adjusted accordingly. The concentration profiles for fluid 1 in the middle and at the outflow sections of the main channel(indicated with a red and a black line in Figure 4.13) can be seen in Figure 4.14 a and b. Slow flows do not need any obstacle to exibit a high degree of mixing. In what follows the inlet velocity of water is fixed to 0.5. Figures 4.15-4.19 illustrate the performance of the different configurations. The obstacles brake the symmetry of parabolic velocity profile (here with a small discontinuity because of the small viscosity difference between the 2 fluids) giving diffusion more time to act. This is evident in Figure 4.20 where the streamlines and velocity vectors are showed for configurations 4 and 8. The efficiencies are listed in Table 4.4, evidencing how to increase the performance it is not sufficient simply to put more obstacles; the layout makes the difference, as can be deducted by the huge increase when passing from C2 to C3 which both possess one obstacle only. C8 proves to be the most efficient configuration, because it forces the fluid to migrate laterally more than any other configuration tested. Table 4.4 also reports the corresponding efficiencies computed in [3], evidencing a close agreement with the performance of a commercial code. The only exception was configuration C3, which was found to be less efficient than C2, while in [3] it achieves twice the efficiency of C2. This discrepancy is probably due to a different vertical position of the obstacle in this study wth respect to what is simulated in [3], as confirmed by the very close match for the other seven configurations.

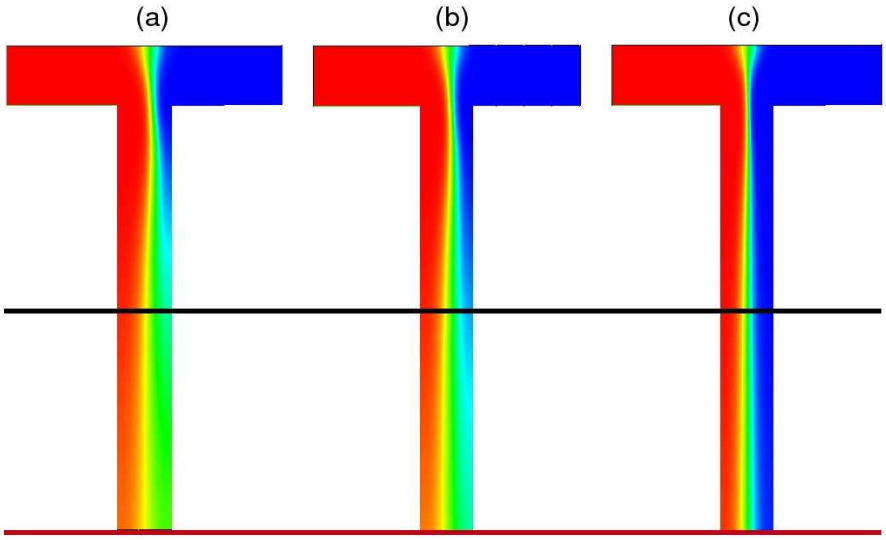

Figure 4.13: Fluid 1 concentration contours at different U: (a) 0.1, (b) 0.15, (c) 0.5.

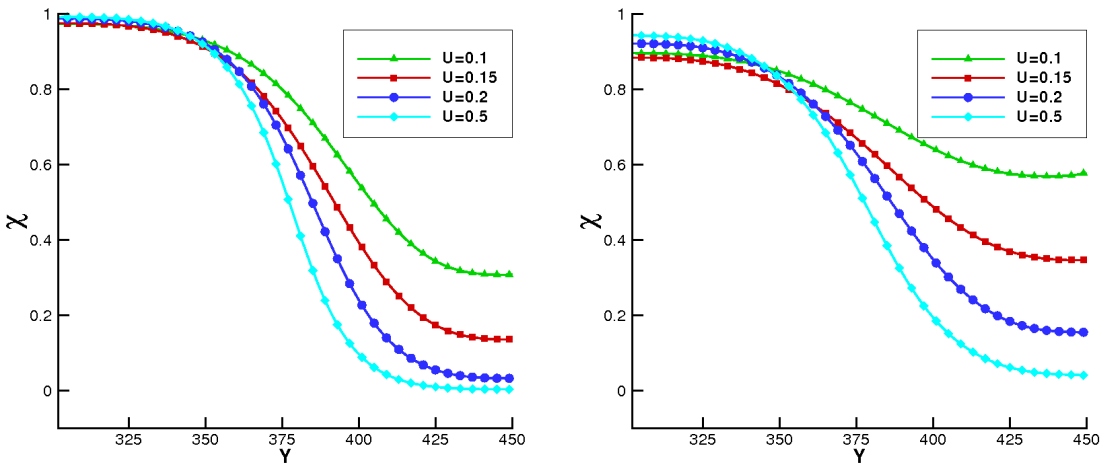

(a) (b)

Figure 4.14: Concentration profiles for fluid 1 (water) at main channel mid-section (a) and outflow sections (b).

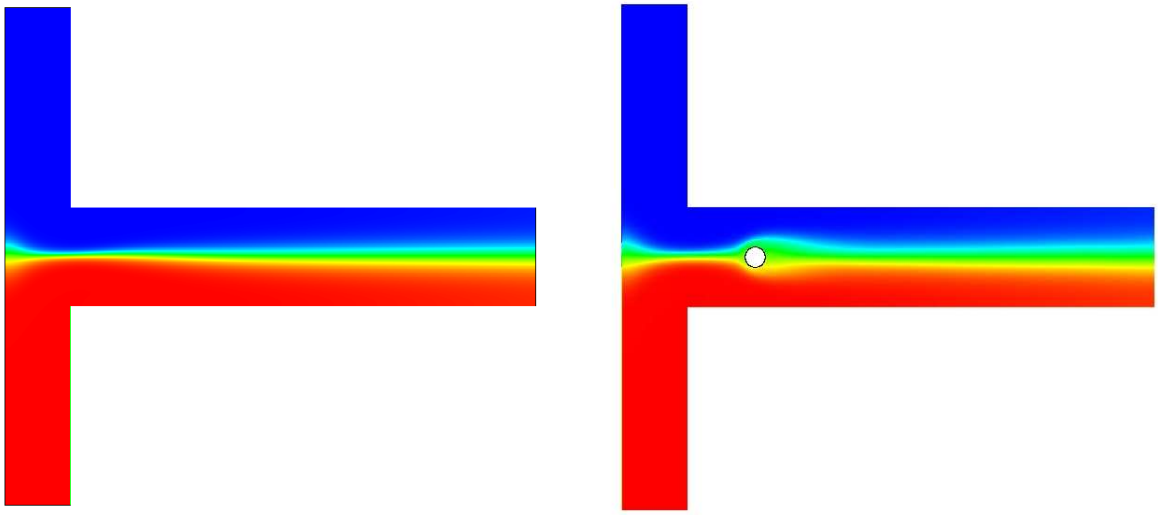

(a) C1 (b) C2

Figure 4.15: LB simulation of T-micromixer for configurations 1 and 2 as proposed in [3].

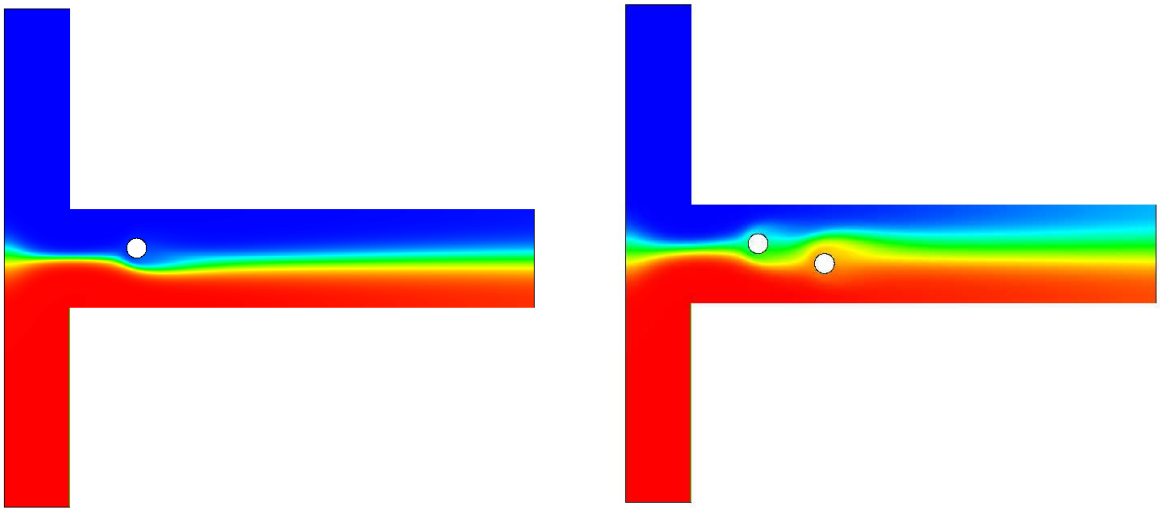

(a) C3 (b) C4

Figure 4.16: LB simulation of T-micromixer for configurations 3 and 4 as proposed in [3].

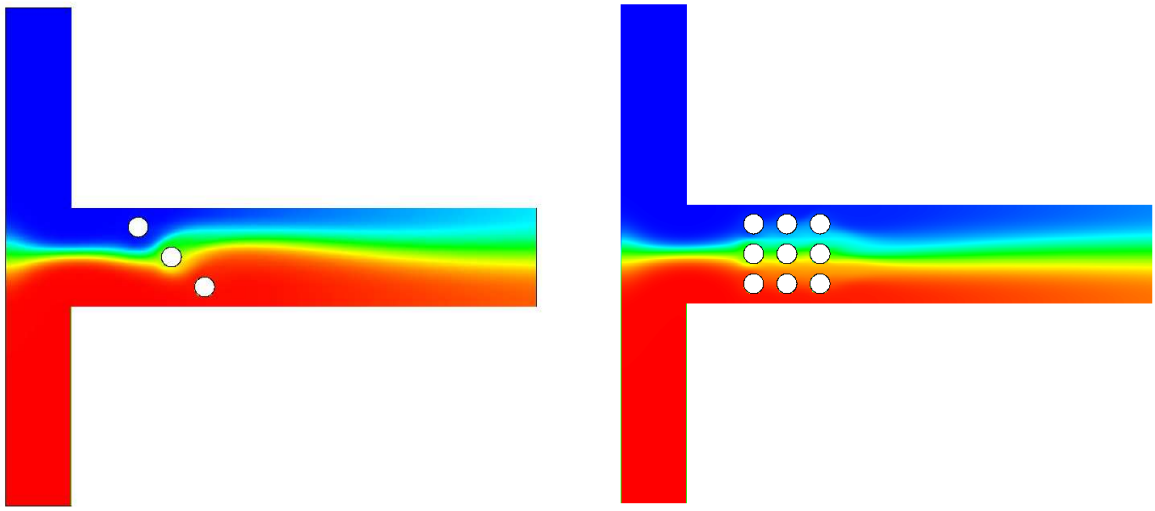

(a) C5 (b) C6

Figure 4.17: LB simulation of T-micromixer for configurations 5 and 6 as proposed in [3].

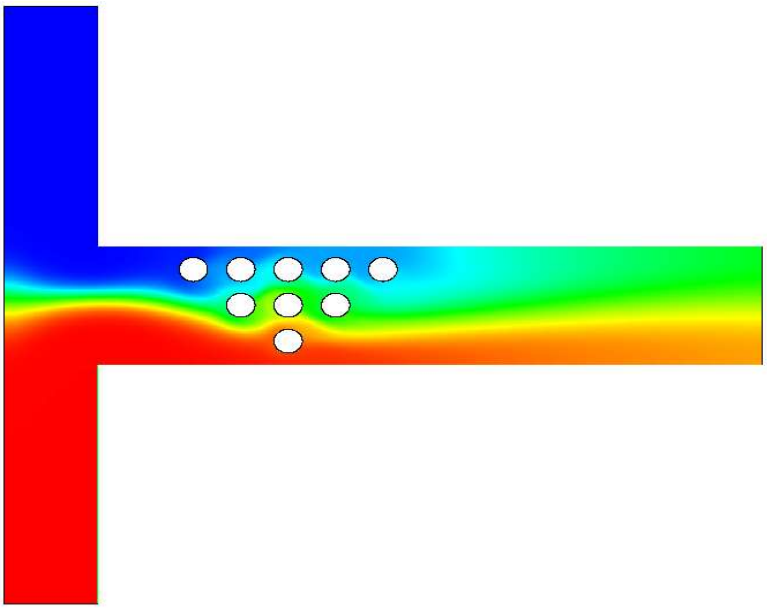

Figure 4.18: LB simulation of T-micromixer for configuration 7 as proposed in [3].

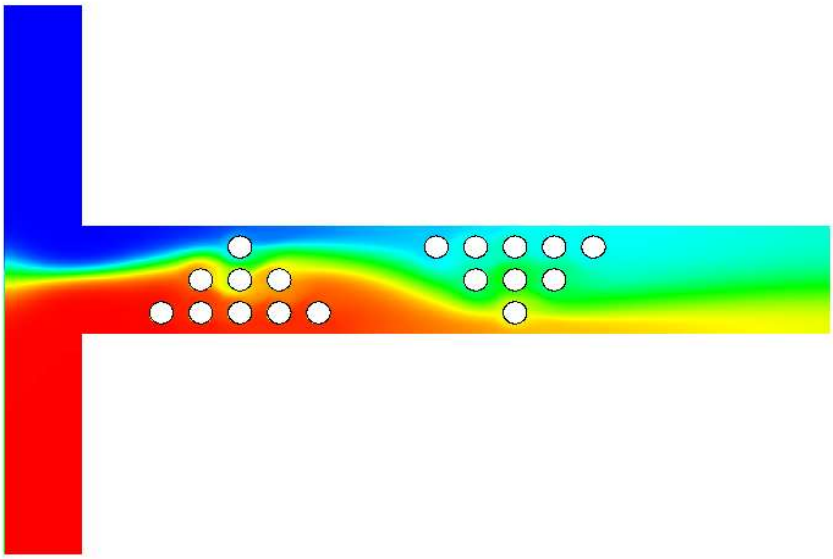

Figure 4.19: LB simulation of T-micromixer for configuration 8 as proposed in [3].

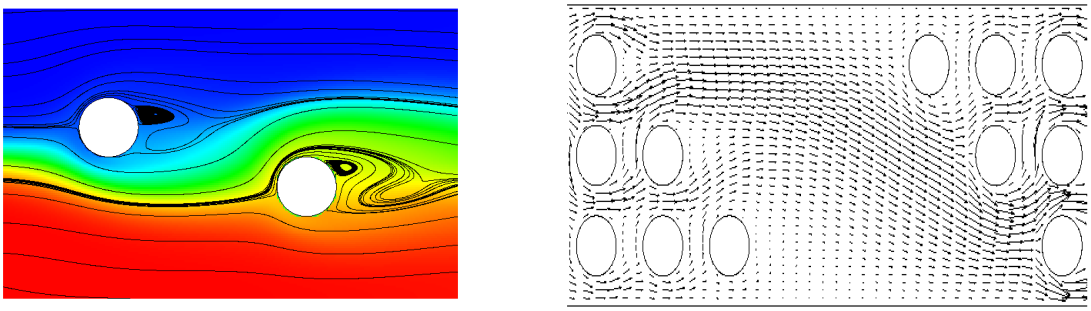

(a) C4 (b) C8

Figure 4.20: Particular of streamlines (a) and velocity vectors (b)for C4 and C8.

	Efficiency (%)	
Configuration	[3]	LB
1	18.0	17.2
2	21.0	22.
3	42.0	20.2
4	44.0	43.8
5	46.0	46.2
6	32.0	31.4
7	53.0	51.3
8	61.0	60.7

Table 4.4: Comparison between the mixing efficiency in [3] and those computed in the present study with LB for all the different configurations.

4.7 Limitations of the SC model

The different cases presented in this chapter demonstrated how a model like the SC, developed almost twenty years ago, might still be applicable to a variety of problems with success. Nevertheless the SC model presents some important limitations, which opened a lot of room for improvement or for developing new multiphase models. These defects are listed below:

- Low density ratio achievable: $\mathcal{O}(10)$
- Thermodynamic inconsistency: the thermodynamic temperature is not explicitly defined; besides the Maxwell construction is satisfied only if $\psi = \rho$. Unfortunately this is the form of effective mass most prone to instabilities.
- Surface tension coupled to the density ratio: once chosen the coupling constant $\mathcal{G}$ or matrix $\mathcal{G}_{j\bar{j}}$ and the effective mass ψ the surface tension is fixed. If for instance a flat interface it is possible to show [73] that:

$$\sigma = \int_{-\infty}^{+\infty} (P_{yy} - P_{xx})\, dy = -\frac{\mathcal{G}c_s^4}{2} \int_{-\infty}^{+\infty} |\partial_y \psi|^2 dy \tag{4.23}$$

  which makes evident the dependance of σ on $\mathcal{G}$ and ψ.

4.8 Other multiphase LB schemes

Historically, the first multiphase model was developed for LGCA by Rothman and Keller in 1988 [18]. This approach, referred to as *colour* model, consisted in identifying the two phases with different colours (red and blue). The collision operator is modified in order to enforce surface tension among the 2 fluids by sending particles of a certain colour prefrebly to neighbour sites where that colour is dominant. An interparticle force depending on colour gradient acts in order to recover interfacial phenomena like Laplace equation: in this way particles of the same colour are encouraged to aggregate. Of course this approach suffered of all the defects of LGCA that have been pointed out in chapter 3. Thanks to the work of Gunstensen et. *al* [74] and Grunau *et al* [75]the colour model was finally integrated into the LBGK framework. Another class of multiphase/multicomponent models is given by the so-called *free-energy-based models* [76]. Their basic idea is to incorporate phenomenological models of interface dynamics like Cahn-Hilliard or Ginzburg-Landau by means of a free energy functional, that attains the minimum value in the equilibrium state. The pressure tensor is defined using the Cahn-Hilliard's approach for non-equilibrium thermodynamics. Multicomponent implementations of this approach can be found in [77] or [78] can be described as "top-down", because macroscopic parameters like surface tension can be directly supplied to the model, by choosing an appropriate form of the free energy. The main limitation of this model consists in the occurrance of Galilean non-invariant terms in the hydrodynamic equations. He, Shan and Doolen [32] proposed a model which is based on a discretization of Boltzmann equation with specific force applied $\mathbf{F}(2.24)$. The specific force includes gravity but most importantly an itermolecular interaction term which accounts for either a term expressed as gradient of a scalar potential, representing mean-field approximation, or Enskog's correction to consider the effect of *exclusion molecular volume*. This model, which will be referred to in what follows as HSD LB, employs two sets of PDFs, one for the velocity field and the second to reconstruct an index function that is used to track the interface, as it happens in volume of fluid or level set methods. Finally it is worth to remember that multiphase means even particle flows: the LB has been applied with success also to these kinds of flows, which pose issues in the implementation of BC as well as in the updating of particle positions. All these problems were addressed for instance in [79] [80] and [81].

Chapter 5

The Multiple-Relaxation-Time LBE

5.1 Introduction

In the previous chapter the basic theory of the lattice Boltzmann method has been presented. The approach followed was to emphasize the continuity of this method with its boolean ancestor, the LGCA, the defects of which were addressed by the successive implementations of the LB. In [22] was demonstrated that LB can be viewed as a special finite difference discretization of the Boltzmann equation (2.24). Whatever the approach adopted, the passage from kinetic theory described in chapter 2 to a feasible numerical scheme involves the following formal discretization:

- $\boldsymbol{\xi} \Rightarrow \mathbf{e}_i$
- $f \Rightarrow f_i$
- $f^{eq} \Rightarrow f_i^{eq}$

As seen in the previous chapter, these approximations allow the writing of a linear evolution equation:

$$\mathbf{f}\left(\mathbf{x}+\mathbf{e}_i, t+1\right) - \mathbf{f}\left(\mathbf{x}, t\right) = \mathbf{S}\left(\mathbf{f} - \mathbf{f}^{eq}\right) \tag{5.1}$$

Here and in what follows the LBE is written in lattice units, so that $\Delta x = \Delta t = 1$. Obviously passing from infinite possible speeds to a discrete velocity space$\mathbb{R}^b$ creates truncation errors and numerical artifacts in the transport coefficients that can influence significantly the macroscopic hydrodynamics and the stability of LB. A Fourier analysis is helpful to stress this point. Given a two dimensional flow characterized by a uniform and steady density ρ and velocity $\mathbf{u} = (u_x, u_y)$ with a small imposed fluctuation, so that $f_i = f_i^{eq} + \delta f$, the LBE with linearized collision operator can be written in vector form as [1]:

$$\delta \mathbf{f}\left(\mathbf{x} + \mathbf{e}_i, t + 1\right) - \delta \mathbf{f}\left(\mathbf{x}, t\right) = \mathbf{S}(\delta \mathbf{f}). \tag{5.2}$$

In Fourier space (5.2) takes the form:

$$\delta \mathbf{f}(\mathbf{k}, t + 1) = \mathbf{A}^{-1}\left[\mathbf{I} + \mathbf{S}\right] \delta \mathbf{f}(\mathbf{k}, t + 1). \tag{5.3}$$

In (5.3) $\mathbf{k} = (k_x, k_y)$ is the wave vector and $A_{\alpha\beta} = \exp\left(i\mathbf{e}_\alpha \cdot \mathbf{k}\right)\delta_{\alpha\beta}$ is the displacement operator. If $\mathbf{L} = \mathbf{A}^{-1}\left[\mathbf{I} + \mathbf{S}\right]$, the solution of (5.3) is equivalent to an eigenvalue problem:

$$\det[\mathbf{L} - z\mathbf{I}] = 0. \tag{5.4}$$

HydrodynamicTransport coefficients, as well as the hydrodynamic modes are determined by the eigenvalues z_α of $\mathbf{L}$ [82]:

$$\nu(\mathbf{k}) = \frac{1}{k^2}\mathrm{Re}[\ln z_T(\mathbf{k})] \tag{5.5a}$$

$$g(\mathbf{k})Vcos\phi = \frac{1}{k}\mathrm{Im}[\ln z_T(\mathbf{k})] \tag{5.5b}$$

$$\frac{1}{2}\nu(\mathbf{k}) + \zeta(\mathbf{k}) = -\frac{1}{k^2}\mathrm{Re}[\ln z_\pm(\mathbf{k})] \tag{5.5c}$$

$$c_s(\mathbf{k}) \pm g(\mathbf{k})Vcos\phi = \mp\frac{1}{k}\mathrm{Im}[\ln z_\pm(\mathbf{k})], \tag{5.5d}$$

where z_T and $z_\pm$ are respectively related to the transverse (shear) and the two longitudinal (sound) hydrodynamic (conserved) modes. Taylor-expanding equations (5.5) in $\mathbf{k}$ it is possible to write:

$$\nu(\mathbf{k}) = \nu_0 + \nu_1 k^2 + \ldots + (-1)^n \nu_n k^{2n} + \ldots \tag{5.6a}$$

$$\zeta(\mathbf{k}) = \zeta_0 + \zeta_1 k^2 + \ldots + (-1)^n \zeta_n k^{2n} + \ldots \tag{5.6b}$$

$$c_s(\mathbf{k}) = c_{s0} + c_{s1} k^2 + \ldots + (-1)^n c_{sn} k^{2n} + \ldots \tag{5.6c}$$

$$g(\mathbf{k}) = g_0 + g_1 k^2 + \ldots + (-1)^n g_n k^{2n} + \ldots \tag{5.6d}$$

The coefficient g indicates the Galilean invariancy of the model (ideally it should be equal to 1). It is important to observe that the usual Chapman-Enskog process leads just to the transport coefficients in the limit $\mathbf{k} = 0$, which are all isotropic. Unfortunately anisotropies and violations of Galilean invariance appear already at second order in k when $\mathbf{u} \neq 0$ [82]. Ideally one would like an LB implementation that could be optimized in order to minimize these effects but that is impossible in the LBGK scheme seen so far, because the only parameter which is possible to tune is the relaxation time related to kinematic viscosity ν. Nevertheless, equation (5.6b) reminds that there is also a bulk viscosity ζ appearing because of the weak compressible nature of LB. If there were the way of controlling ζ indipendently on ν, or in other words of supplying the LB with some *hyperviscosity*, the stability of the scheme could be enhanced.

So far the LB implementation presented was related to the vector space defined by the velocity vectors characterizing $\mathcal{L}$, $\mathbb{V}^b$. Another *stream and collide* linearized representation is possible, in the b-dimensional vector space $\mathbb{M}^b$ based on the b velocity moments of the distribution functions, $\varrho_i | \{i = 0, 1, \ldots, b-1\}$:

$$\boldsymbol{\varrho}(\mathbf{x} + \mathbf{e}_i, t+1) - \boldsymbol{\varrho}(\mathbf{x}, t) = -\hat{\mathbf{S}}(\boldsymbol{\varrho} - \boldsymbol{\varrho}^{eq}) \tag{5.7}$$

Using this representation is justified considering that from kinetic theory it is well known that many hydrodynamic processes depends on coupling between different modes of collision operator of (2.32). These modes are directly related to moments, making this last representation quite convenient in order to incorporate physics into the LB. Besides, the physical significance of the moments makes the corresponding relaxation times directly linked with transport coefficients. The two representations have to be related by a linear transformation, so that:

$$\boldsymbol{\varrho} = \mathbf{M}\,\mathbf{f} \tag{5.8a}$$

$$\mathbf{f} = \mathbf{M}^{-1}\boldsymbol{\varrho} \tag{5.8b}$$

where $\mathbf{M} = (\mathbf{v}_0, \mathbf{v}_1, \ldots, \mathbf{v}_{b-1})^T$. To constuct this $b \times b$ matrix is necessary to define from $\mathbf{e}_i | \{i = 0, 1, \ldots, b-1\}$ a new set of linearly indipendent vectors $\mathbf{v}_i | \{i = 0, 1, \ldots, b-1\}$ representing an orthogonal basis for the new space. The guideline followed is to have a diagonal collision matrix $\hat{\mathbf{S}}$ in (5.7) so to have the simplest possible collision operator even in $\mathbb{M}^b$. This goal can be accomplished via a Gram-Schmidt procedure in order to diagonalize the collision matrix $\mathbf{S}$ of (5.1). The resulting $\mathbf{v}_i$ are the eigenvectors of matrix $\mathbf{S}$:

$$\hat{\mathbf{S}} = \mathbf{M} \cdot \mathbf{S} \cdot \mathbf{M}^{-1} = \mathrm{diag}\,(s_0, s_1, \ldots, s_{b-1}) \tag{5.9}$$

Finally, combining equations (5.1),(5.7), (5.8)-(5.8b) and finally (5.9) it is possible to write the *Multiple-Relaxation-Times lattice Boltzmann* (MRT-LB) equation as [83]:

$$\mathbf{f}\,(\mathbf{x} + \mathbf{e}_i, t+1) - \mathbf{f}\,(\mathbf{x}, t) = -\mathbf{M}^{-1}\hat{\mathbf{S}}\,(\boldsymbol{\varrho} - \boldsymbol{\varrho}^{eq}) \tag{5.10}$$

The moments can be distinguished into conserved (hydrodynamic) and non-conserved (kinetic), depending on whether they are conserved by the collision process. For athermal flows the first group is composed by density and momentum components. The $\varrho_i^{eq} | \{i = 0, 1, \ldots, b-1\}$ are functions of the conserved moments and inherits the symmetries of the underlying $\mathcal{L}$. As will be shown in the next section, their expressions provides a first set of parameters that can be tuned in order to reduce the effects of numerical artifacts of the scheme. Other parameters are naturally given by the relaxation times: in this case the relaxation of each moment can be controlled separately [82]. By the definition of conserved moments follows that the corresponding relaxation times can take whatever value. Special care has to be followed when body forces are modelled via method I described by (3.18), as pointed out in [84]. The algorithm behind (5.9) involves some additional steps when compared to LBGK schemes; it is infact firstly necessary to switch from $\mathbb{V}^b$

to $\mathbb{M}^b$ via (5.8), in order to perform collision in this space using diagonal matrix $\hat{\mathbf{S}}$; finally the post-collisional moments are projected back into the $\mathbb{V}^b$ via (5.8b) and the obtained distribution functions undergo the streaming step in order to complete the update for that time step. The additional computational cost can be reduced by optimizing the matrix-vector products as specified for instance in [85].

5.1.1 D2Q9 Model

After having described the most general implementation of MRT-LB a specific insight on the implementation related to $D2Q9$ lattice will be given in this section. The moments for this model are given by:

$$\boldsymbol{\varrho} = (\rho, e, \varepsilon, j_x, q_x, j_y, q_y, p_{xx}, p_{xy})^T . \tag{5.11}$$

they are the density ρ, the momentum $\mathbf{j}$ and heat $\mathbf{q}$ flux components, the energy e and its square ε and finally the diagonal and off-diagonal terms of the stress tensor p_{xx} and p_{xy}. The most general form of the equilibrium moments is [82]:

$$\varrho_1^{eq} = e^{eq} = \frac{1}{4}\alpha_2\rho + \frac{1}{6}\gamma_2 (\mathbf{j}\cdot\mathbf{j}) \tag{5.12a}$$

$$\varrho_2^{eq} = \varepsilon^{eq} = \frac{1}{4}\alpha_3\rho + \frac{1}{6}\gamma_4 (\mathbf{j}\cdot\mathbf{j}) \tag{5.12b}$$

$$\varrho_{4,6}^{eq} = q_{x,y}^{eq} = -\frac{1}{2\rho}c_1 j_{x,y} \tag{5.12c}$$

$$\varrho_7^{eq} = p_{xx}^{eq} = \frac{1}{2\rho}\gamma_1 \left(j_x^2 - j_y^2\right) \tag{5.12d}$$

$$\varrho_8^{eq} = p_{xy}^{eq} = \frac{1}{2\rho^2}\gamma_3 j_x j_y \tag{5.12e}$$

The free parameters are α_2, α_3, $\gamma_{1\ldots4}$ and c_1. Their values can be calculated optimizing the scheme according to the guidelines previously mentioned. The optimization process involves the analysis of different simple flow cases. The first example is the flow without streaming velocity: in the $\mathbf{k} = \mathbf{0}$ limit the speed of sound, the shear and the bulk viscosities are given by:

$$c_s^2 = \frac{1}{3}\left(2 + \frac{\alpha_2}{8}\right) \tag{5.13a}$$

$$\nu_0 = \frac{2 - c_1}{12}\left(\frac{1}{s_8} - \frac{1}{2}\right) \tag{5.13b}$$

$$\zeta_0 = \frac{c_1 + 10 - 12c_s^2}{24}\left(\frac{1}{s_2} - \frac{1}{2}\right). \tag{5.13c}$$

Since the transport coefficient have to be positive the following bounds for the parameters of the equilibriummomenta and the relaxation times can be defined:

$$\alpha_2 > -16 \tag{5.14a}$$

$$-4 < c_1 < 2 \tag{5.14b}$$

$$0 < s_2 < 8 \tag{5.14c}$$

$$0 < s_8 < 8 \tag{5.14d}$$

Considering instead a flow with constant streaming velocity $\mathbf{U} = (U_x, U_y)$ which forms an angle ϕ with the wave vector $\mathbf{k}$; equations (5.5) indicates that to the first order in $\mathbf{k}$ the eigenvalues z_T and $z_\pm$ give the phase $gU\cos\phi$ and the sound speed c_s. In order to have $g_0 = 1$ one has to set $\gamma_1 = \gamma_4 = 2/3$, while $\gamma_2 = 18$. In order to eliminate the anisotropy in the $\mathbf{U}$-dependence of the shear wave attenuation one must chose $c_1 = -2$. All those values lead to the following expression for the shear viscosity in the limit $\mathbf{k} = 0$:

$$\begin{aligned}\nu_0 = \left[s_2(2 - s_8)\left[c_s^2 + (1 - 3c_s^2)U^2\cos^2\phi\right] + 3\left[2(s_8 - s_2) + \right.\right. \\ \left.\left. s_8(s_2 - 2)\cos^2\phi\right]U^4\cos^2\phi\right]\left[6s_2s_8(U^2\cos^2\phi + c_s^2)\right].\end{aligned} \tag{5.15}$$

In the same limit the bulk viscosity has the following expression:

$$\zeta_0 = \Big(U\cos\phi\sqrt{U^2\cos^2\phi + {c^2}_s}\left\{12U^2\left[(s_2 - s_8) + s_2(s_8-2)\cos^2\phi\right] + (2s_2 - 3s_2s_8 + 4s_8)\left(1 - 3{c^2}_s\right)\right\} + 3U^4\cos^2\phi\left[\cos^2\phi\left(2s_2 - 3s_2s_8 - 8s_8\right) + 6(s_2 - s_8)\right] + 2U^2\cos^2\phi\left[6\left(s_2s_8 - s_2 - s_8\right)c_s^2 + s_8(2 - s_2)\right] + c_s^2\left[6U^2(s_2 - s_8) + s_8(2 - s_2)(2 - 3c_s^2)\right]\Big) / \left\{12s_2s_8(U^2\cos^2\phi + c_s^2)\right\}. \tag{5.16}$$

The streaming velocity $\mathbf{U}$ has therefore got a second order effect on ν_0, which can be eliminated by using a 13-speeds lattice, together with a first-order effect on ζ_0 that can be tackled by setting $\alpha_2 = -8$. Finally, in order to obtain the SRT-LB formulation when all the relaxation times are equal to $1/\tau$ the remaining parameters α_3 and γ_4 have respectively to be given the values of 4 and -18. Further details can be found in [82]. Here it is sufficient to write the final expressions of the equilibrium moments:

$$\varrho_1^{eq} = e^{eq} = -2\rho + 3\left(\mathbf{j}\cdot\mathbf{j}\right) \tag{5.17a}$$

$$\varrho_2^{eq} = \varepsilon^{eq} = \rho - 3\left(\mathbf{j}\cdot\mathbf{j}\right) \tag{5.17b}$$

$$\varrho_{4,6}^{eq} = q_{x,y}^{eq} = -\frac{1}{\rho}j_{x,y} \tag{5.17c}$$

$$\varrho_7^{eq} = p_{xx}^{eq} = \frac{1}{\rho}\left(j_x^2 - j_y^2\right) \tag{5.17d}$$

$$\varrho_8^{eq} = p_{xy}^{eq} = \frac{1}{\rho^2}j_xj_y \tag{5.17e}$$

The collision matrix in moment space has the following form:

$$\hat{\mathbf{S}} = \mathrm{diag}\left(0, s_2, s_3, 0, s_5, 0, s_7, 0, s_8, s_9\right), \tag{5.18}$$

where the zero terms are related to conserved moments and $s_8 = s_9$ are related to the kinematic viscosity; from equations (5.13) and (5.14) it follows that:

$$\nu = \frac{1}{3}\left(\frac{1}{s_8} - \frac{1}{2}\right) = \frac{1}{3}\left(\frac{1}{s_9} - \frac{1}{2}\right). \tag{5.19}$$

The other relaxation times are usually set equal to 1. In [82] a local stability analysis for a system with fully periodic boundaries led to $s_2 = 1.63$, $s_3 = 1.14$ and $s_5 = s_7 = 1.92$. The influence of boundary conditions, that can completely change the stability behaviour, was not discussed. Finally, The matrix relating the velocity and momentum spaces is:

$$\begin{bmatrix} 1 & 1 & 1 & 1 & 1 & 1 & 1 & 1 & 1 \\ -4 & -1 & -1 & -1 & -1 & 2 & 2 & 2 & 2 \\ 4 & -2 & -2 & -2 & -2 & 1 & 1 & 1 & 1 \\ 0 & 1 & 0 & -1 & 0 & 1 & -1 & -1 & 1 \\ 0 & -2 & 0 & 2 & 0 & 1 & -1 & -1 & 1 \\ 0 & 0 & 1 & 0 & -1 & 1 & 1 & -1 & -1 \\ 0 & 0 & -2 & 0 & 2 & 1 & 1 & -1 & -1 \\ 0 & 1 & -1 & 1 & -1 & 0 & 0 & 0 & 0 \\ 0 & 0 & 0 & 0 & 0 & 1 & -1 & 1 & -1 \end{bmatrix}$$

5.2 Application: the lid-driven cavity

In order to verify the increased stability of the MRT-LB over the SRT scheme at high Re numbers the driven cavity is reconsidered as a test case in this section. In the previous chapter some results have been presented related to the simplest case with $D_c = 1$ at relatively low Re. The first part of this section will therefore extend the results reported in [4], while in the second part the square cavity will be again considered, but at exceptionally high Re. These last cases are an extension of what is reported in [86]. All these flows were simulated here with the previously seen implementation of MRT-LB for $D2Q9$ model. For each geometry the flow is described by plotting the streamlines and the vorticity contours. The values of the relaxation frequencies relative to non-conserved modes were set respectively to $s_2 = 1.1$, $s_3 = 1.0$ and $s_5 = s_7 = 1.2$, since the values reported at the end of the last section were found to cause instabilities in many configurations. The remaining two frequencies were set to $s_8 = s_9 = 1/\tau$. The f_i^{eq} are in the form proposed in [45] to limit density fluctuations around the initial density $\rho_0 = 1.0$. Finally, the boundary conditions adopted are BBK for all walls but for the moving, which is modelled with the extrapolation scheme described in the previous chapter. That

choice of BC marks a difference with both the LB works considered in this section as benchmark: infact, in [4] the BC for the moving wall consists in simply assigning to the unknown distributions their equilibrium value, $f_i = f_i^{eq}|\{U_0, 0\}$, while in [86] the extrapolation scheme is applied to model the entire cavity walls.

5.2.1 Rectangular cavity

In [4] LB simulations of flows in cavities with $D_c \in [0.1, 7]$ and $Re \in [0.01, 5000]$ are considered. The standard LB algorithm relies on a regular $\mathcal{L}$. This approach results in a huge number of points in cavities with high aspect ratios; in order to tackle this problem, an interpolated LB (interested reader can refer for instance to [87] or [88]) scheme is adopted. Here the standard approach has been followed, but the cases where $D_c > 1$ where run parallel. In all the simulations the moving wall is resolved with 256 nodes, and $U_0 = 0.1$ in lattice units. The first case studied is $D_c = 0.1$. In [4] this simulation is conducted at $Re = 5000$, while here $Re = 7500$, $Re = 10000$ and $Re = 20000$ where considered. The streamlines for all these Re are reported in Figure 5.1, including the case at $Re = 5000$ from [4]. When compared to $Re = 5000$, the third vortex which in the top of the cavity is more intense, together with the vortex close to the lower wall at $(\bar{x}, \bar{y}) = (0.81, 0.026)$. Besides a new vortical structure centered in $(0.65, 0.0242)$ appears. Increasing Re to 10000 lead most notably to the developement of this last vortical structure, the center of which moves leftwards, together with the left corner vortex. Finally at $Re = 20000$ a succession of uniform vortex stuctures occupying the whole cavity is visible. In respect to $Re = 5000$ case the number of vortical structures increased almost 4 times for $Re = 20000$. Vorticity contours are instead represented in Figure 5.2 The next case considered is related to $D_c = 0.5$. This case was widely treated in [4]: Figure 3 from this reference shows the evolution of the vortical structures when Re changes from 0.01 to 5000. In the first case there is just one big central vortex plus two at the corners. As Re is increased the cavity is occupied principally by two counterrotating structures: the original vortex moved towards the right wall of the cavity, while a less intense structure occupies almost the whole left part of the cavity. This regime can be observed in Figure 5.3 (a).

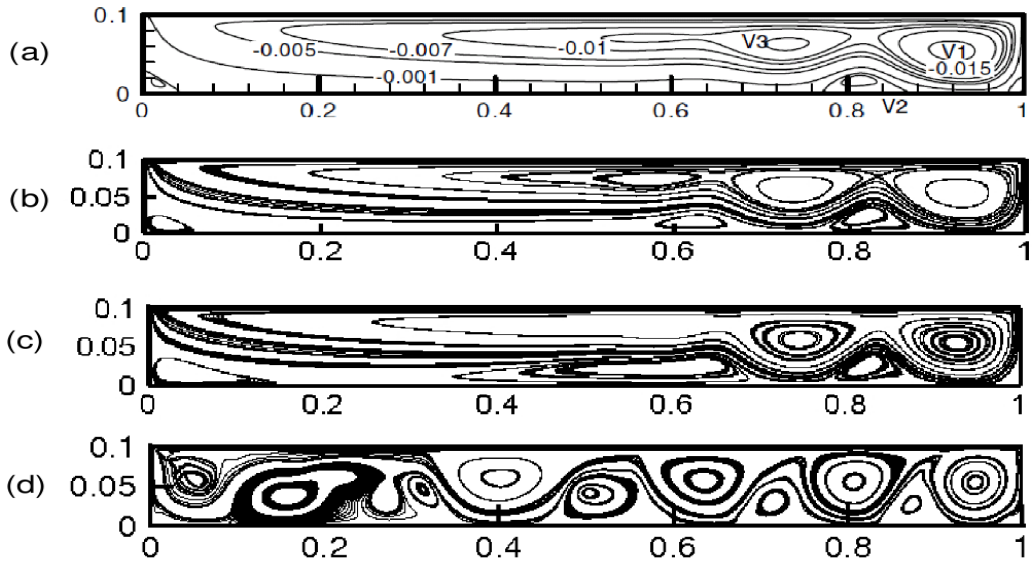

Figure 5.1: Streamlines for $D_c = 0.1$ and (a) $Re = 5000$ (from [4]), (b) $Re = 7500$, (c) $Re = 10000$, (d) $Re = 20000$.

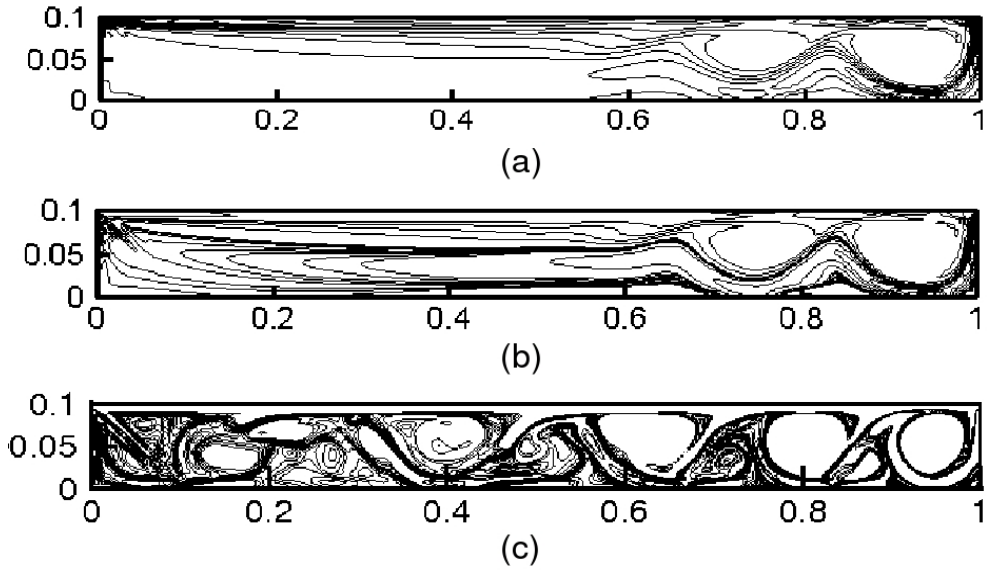

Figure 5.2: Vorticity contours Streamlines for $D_c = 0.1$ and (a) $Re = 7500$, (b) $Re = 10000$ and (c) $Re = 20000$.

This configuration substantially holds also at $Re = 7500$, as showed in Figure 5.3(b), but a new vortical structure is apperaring on the lower wall. Finally Figure 5.3 (c) is related to $Re = 10000$ and shows that the separation between the two main structures is more and more pronounced; the part of the left vortex that laid in the right half of the cavity is now an independent vortical structure; the corner vortices have increased as well.

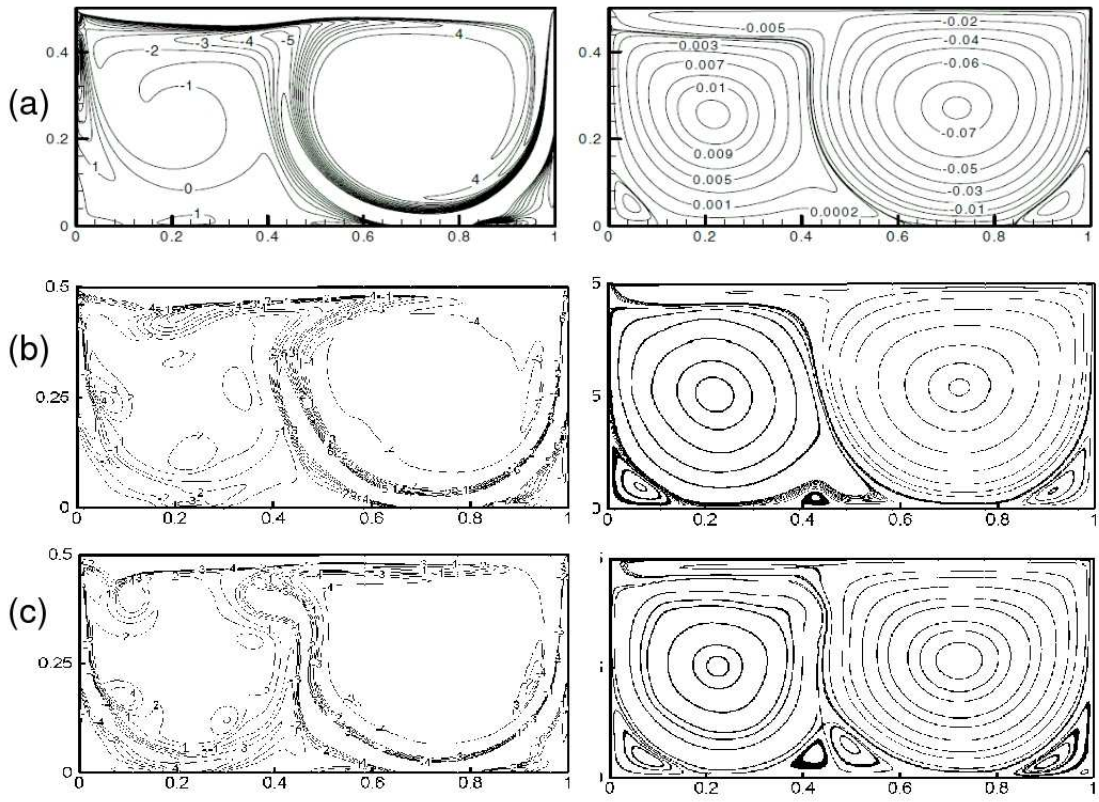

Figure 5.3: Vorticity contours (left column) and streamlines (right column)for $D_c = 0.5$ and (a)$Re = 5000$ (from [4]), (b) $Re = 7500$ and (c) $Re = 10000$.

Finally, flow is examined for $D_c = 3.2$. For $D_c > 1$ the trend reported in [4] sees the cavity occupied by a succession of three counterotating vortical structures disposed regularly from top to bottom, each of them extending for the whole width of the cavity. These vortices have centres almost aligned on the vertical symmetry axis and their intensity decreases as the distance from the top wall increases. Corner

vortices are negligible. Once again, raising Re breaks the symmetry of this configuration: other vortices appear at the boundaries of bigger structures, as showed in Figure 5.4, which reports the streamlines related to cases $Re = 1000$, $Re = 7500$ and finally $Re = 10000$; these new vortices interact with the three bigger structures and either at $Re = 7500$ or at $Re = 10000$ the cavity is occupied by four big vortices, as can be seen in figures 5.4b and 5.4c. It is interesting to note that the bottom vortex moved rightwards leaving space to the upper one. A further increase of Re is likely to split the upper vortex in 2 new structures. The vorticity contours for $Re = 7500$ and $Re = 10000$ are also reported in figures 5.5a and 5.5b. It is important to underline that in [4] the case $D_c = 3.2$ is tested only at $Re = 1000$.

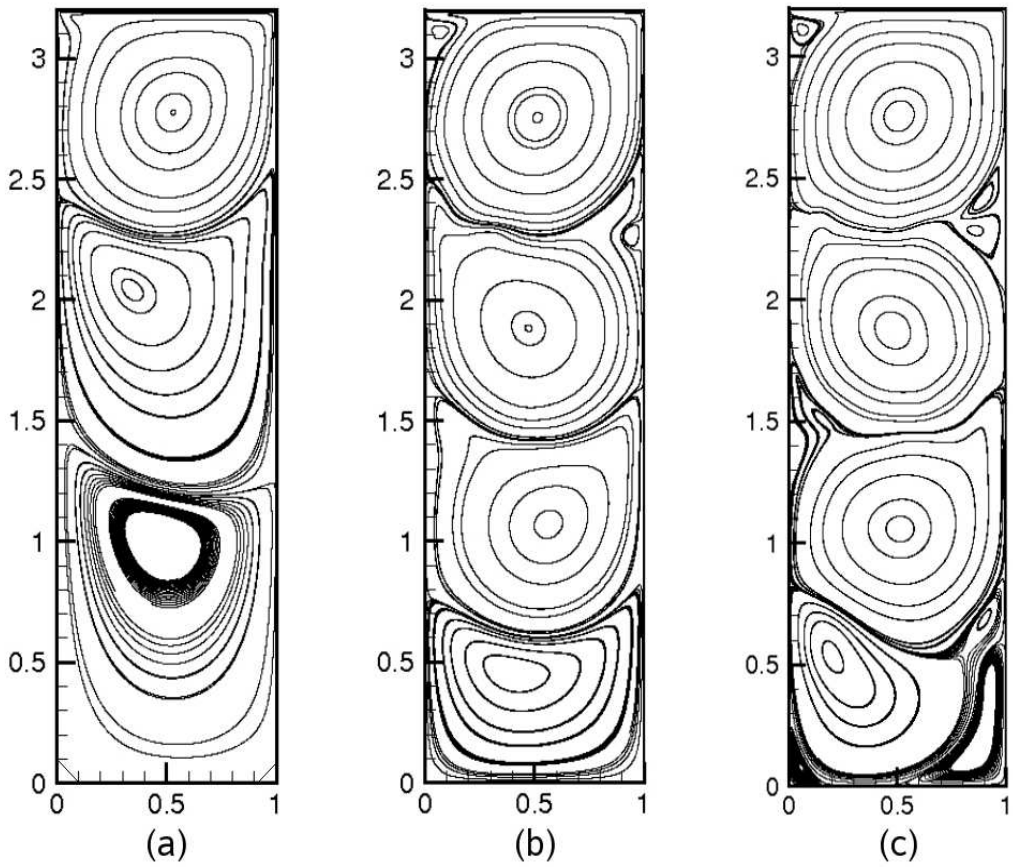

Figure 5.4: Streamlines for the case $D_c = 3.2$ at (a) $Re = 1000$, (a) $Re = 7500$ and (c) $Re = 10000$.

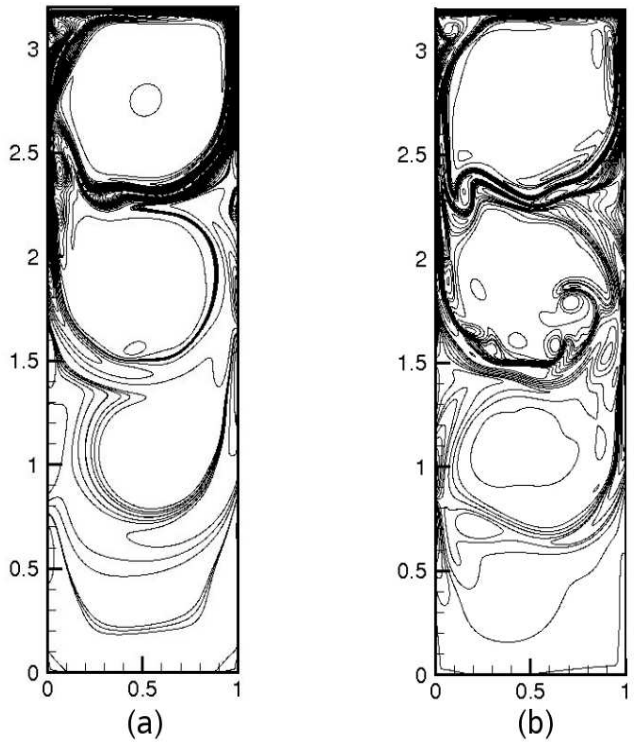

Figure 5.5: Vorticity for the case $D_c = 3.2$ at (a) $Re = 7500$ and (b) $Re = 10000$.

5.2.2 Square cavity at high Re

In [86] the flow in a square cavity was simulated with LB for Re up to $Re = 1E6$. This limit has been further increased here, up to $Re = 2.5E6$ (Figure 5.9). Flow regimes at $Re = 1.25E6$ (Figure 5.6), $Re = 1.5E6$ (Figure 5.7) and $Re = 2E6$ (Figure 5.8) are also reported. The grid size is 513×513; tests with a finer grid, 1025×1025 did not demonstrate signficant differencies. Once again, each case is described via the corresponding streamlines and vorticity contours. The relaxation time τ was varied in the range [0.50012288, 0.50006144]. Obviously, since there are no experimental or numerical works at similar Re, the accuracy of these results is questionable; what matters here is that they prove the superior stability of MRT-LB, which allowed stable direct numerical simulations of quite a complex flow.

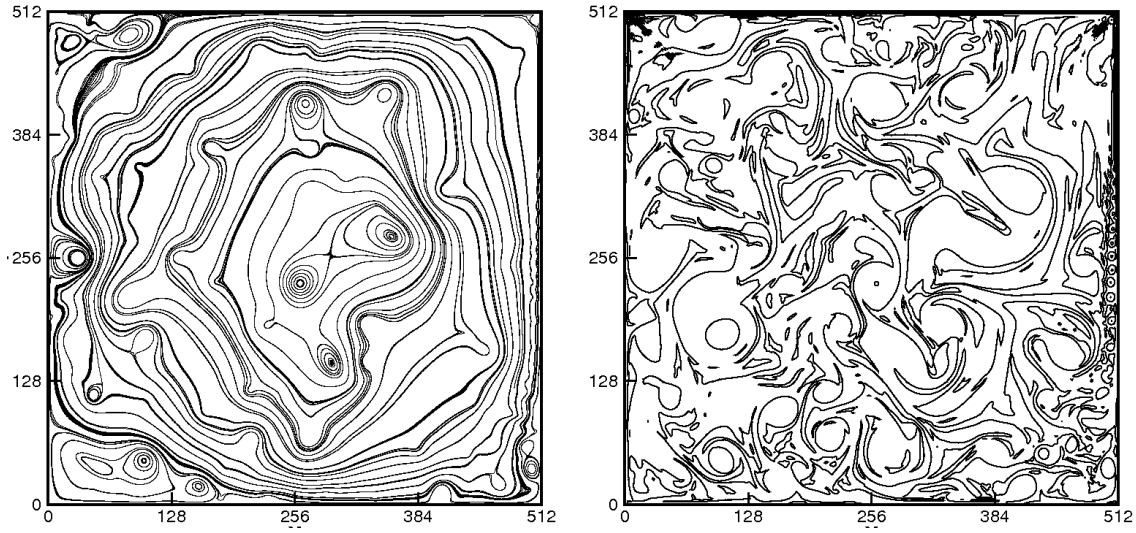

(a) (b)

Figure 5.6: Streamlines (a) and vorticity contours (b) for $D_c = 1$ and $Re = 1.25E6$.

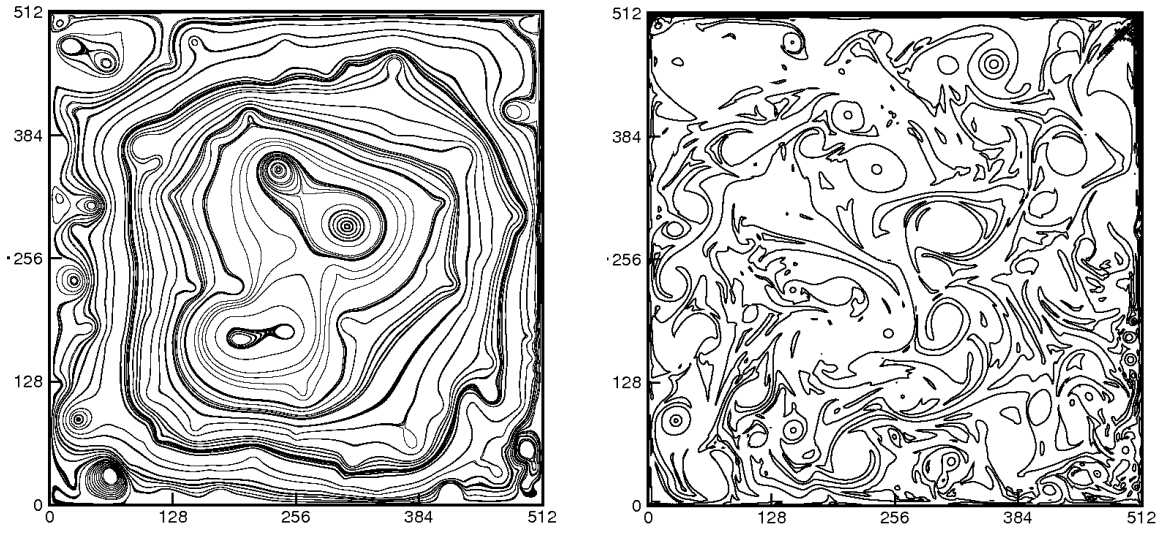

(a) (b)

Figure 5.7: Streamlines (a) and vorticity contours (b) for $D_c = 1$ and $Re = 1.5E6$.

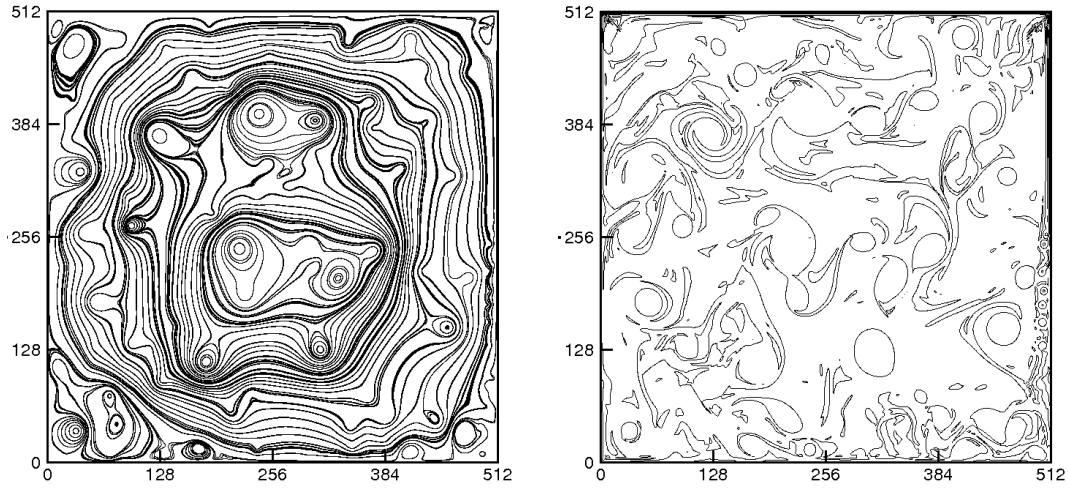

(a) (b)

Figure 5.8: Streamlines (a) and vorticity contours (b) for $D_c = 1$ and $Re = 2E6$.

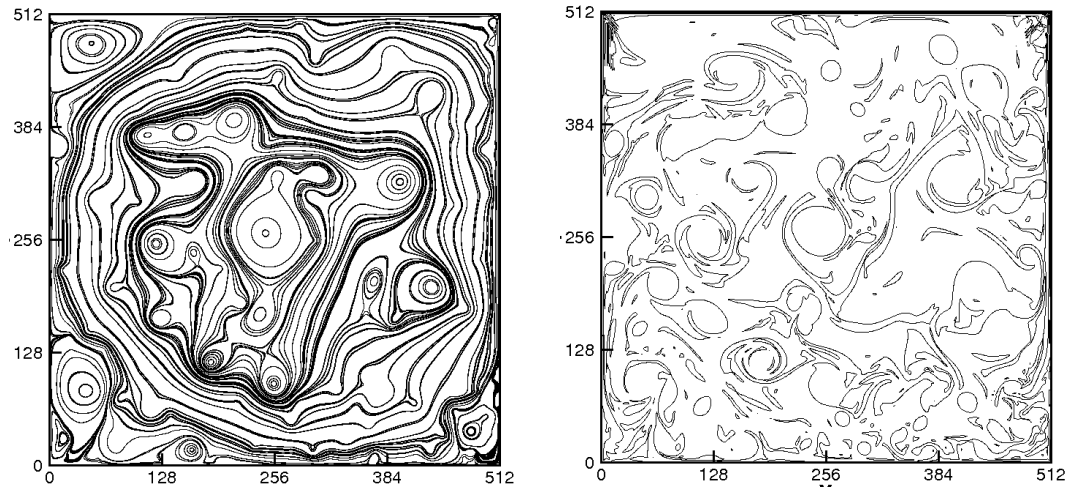

(a) (b)

Figure 5.9: Streamlines (a) and vorticity contours (b) for $D_c = 1$ and $Re = 2.5E6$.

5.3 Other MRT formulations

A further MRT formulation is the Two-Relaxation-Time (TRT) [89], [90]. Having defined *link* as a pair of opposite lattice velocities, a link-wise collision operator is introduced as an alternative to the MRT scheme previously defined. This formulation can be applied to any kind of lattice structure $\mathcal{L}$. The projections are the symmetric and the anti-symmetric parts of a pair of populations with opposite velocities. Link-operators and MRT collision coincide for one particular configuration of eigenvalues associated to symmetric and anti-symmetric basis vectors. This configuration, suitable for both mass and momentum conservation equations, is called the TRT operator. The TRT collision equals the BGK collision in terms of computational time and simplicity, but it benefits from additional collision freedom to improve stability, like the MRT operators.

In [91] it was noticed that the MRT-LB previously introduced is not related to kinetic theory, but rather is a numerical trick based on the weakly compressible nature of LB; a different MRT formulation was presented in [91]. The starting point is an ELB scheme: as seen in chapter 3, the ELB formulation is based on the definition of a Maxwellian equilibrium f_M (3.15) which possesses all the properties of an equilibrium distribution (conservation of mass and momentum) plus being the solution of the problem of minimizing a discrete H-function (3.16). In [91] the equilibrium function has to minimize H under the further constraint of prescribed diagonal components of stress tensor. The *generalized Maxwellian* found takes the following expression:

$$f_{G,i} = \rho \prod_{\alpha=x,y} w_i(e_{i\alpha}) \frac{3(c^2 - \Pi_{\alpha\alpha})}{2c^2} \left(\sqrt{\frac{\Pi_{\alpha\alpha} + cu_{\alpha\alpha}}{\Pi_{\alpha\alpha} - cu_{\alpha\alpha}}} \right)^{e_{i\alpha}/c} \left(\frac{2\sqrt{\Pi_{\alpha\alpha}^2 - c^2 u_{\alpha\alpha}^2}}{c^2 - \Pi_{\alpha\alpha}} \right)^{e_{i\alpha}^2/c^2} . \tag{5.20}$$

This new kind of distribution function is the lattice counterpart of the anisotropic Gaussian distribution of kinetic theory $f_G \; exp{-}(1/2)(\mathbf{e} - \mathbf{U}) \cdot \mathbf{\Pi^{-1}} \cdot (\mathbf{e} - \mathbf{U})$. Considering the plane (Π_{xx}, Π_{yy}) and having defined $T(\mathbf{\Pi}) = \Pi_{xx} + \Pi_{yy}$ as the trace of the stress tensor, it is possible to define two points M and C; the first corresponds to f_M defined by equation (3.15), while the second is the point for which a given trace corresponds to the minimum of $H_G = H(\mathbf{f}_G)$. A linear interpolation characterized

by the parameter λ between these two points determines the point E of *generalized equilibrium*:$E(\lambda) = (1-\lambda)M + \lambda E$. The collision operator is given by:

$$\mathbf{\Omega} = \omega \mathbf{I} \left(\mathbf{f_{GE}}(\lambda) - \mathbf{f} \right), \tag{5.21}$$

where $\mathbf{f}_{GE} = f_{G,i}\left(\rho, \mathbf{u}, \Pi^E_{xx}(\mathbf{u}, T), \Pi^E_{yy}(\mathbf{u}, T)\right)$. At low Mach numbers $\Pi^E_{\alpha\alpha} = \Pi^M_{\alpha\alpha} + \lambda\frac{T-T_M}{2} + \mathcal{O}(U)^4$ and after some algebra one can write:

$$\mathbf{\Omega'} = \mathbf{A} \left(\mathbf{f_M}(\lambda) - \mathbf{f} \right), \tag{5.22}$$

where $\mathbf{A} = \omega \mathbf{B} \mathbf{\Lambda} \mathbf{B}^{-1}$ and the transformation matrices expressions:

$$\mathbf{\Lambda} = \mathrm{diag}\left([0,0,0], \begin{bmatrix} r_+ & r_- \\ r_- & r_+ \end{bmatrix}, [1,1,1] \right) \tag{5.23a}$$

$$\mathbf{B} = \left(1, e_x, e_y, e_x^2, e_y^2, e_x e_y, e_x^2 e_y, e_x e_y^2, e_x^2 e_y^2\right)^T, \tag{5.23b}$$

where $r_\pm = (r \pm 1)/2$ and $r = 1 - \lambda$. Equation (5.22) defines a MRT operator $\mathbf{\Omega'}$ characterized by matrix A which possess two-relaxation times (ω and $\delta = r\omega$) which are directly related respectively to the shear and bulk viscosities:

$$\nu = \frac{c^2}{3\omega} \tag{5.24a}$$

$$\zeta = \frac{c^2}{3\delta} \tag{5.24b}$$

This model was tested in [91] on Taylor-Green vortex flow, showing its effectiveness with respect to the SRT-LB formulation in improving the stability of the algorithm. Besides, the implementation of this model is simpler than MRT formulation previously defined.

Chapter 6

Improving the SC model

As seen in the last chapter one of the main defects of the SC model is the low density ratio achievable. That is strictly coupled with the existence of spurious currents at interfaces. In this chapter some strategies for addressing this issue are presented, based on the incorporation of different EOS and on the increased accuracy of the gradient operator appearing in equation (4.4). The performance of the model at low viscosities is also investigated: the performance of the different ways of incorporating a body force like that upon which the SC model is based is also discussed.

6.1 Inserting new EOS

In [10] but most notably in [9] it was shown how to incorporate different EOS widely used in the description of nonideal fluid behaviour. To illustrate this idea we consider again the van der Waals EOS:

$$p = \frac{\rho RT}{1 - b\rho} - a\rho^2 \tag{6.1}$$

As seen in chapter 4, the constants a and b are directly related to the critical properties of the fluid via relations specific for each EOS. For the vdW EOS they are:

$$\rho_c = \frac{1}{3b}, \quad p_c = \frac{a}{27b^2}, \quad T_c = \frac{8a}{27Rb}. \tag{6.2}$$

Considering a single component case, the thermodynamic pressure computed by the SC model is given by equation (4.10) and depends on the form of the effective mass; setting the pressure computed by (4.10) equal to that computed by (6.1) means writing an equation for the effective mass ψ, that can be finally expressed as:

$$\psi = \sqrt{\frac{2\left(p - \rho c_s^2\right)}{\mathcal{G}\ c_s^2}} = \sqrt{\frac{2p^\star\left(\mathbf{x}, t\right)}{\mathcal{G} c_s^2}} \tag{6.3}$$

where $p^\star\left(\mathbf{x}, t\right)$ is the nonideal part of the EOS. Equation (6.3) is very simple, but has an important implication: it brings an explicit temperature inside the SC model, thanks to (6.1); the resulting expression for the specific force associated to SC model is therefore:

$$F_\alpha\left(\mathbf{x}, t\right) = -c_s^2 \sqrt{\frac{2p^\star\left(\mathbf{x}, t\right)}{\mathcal{G} c_s^2}} \sum_i w(|\mathbf{e}_i^2|) \mathcal{G} \sqrt{\frac{2p^\star\left(\mathbf{x} + \mathbf{e}_i, t\right)}{\mathcal{G} c_s^2}} e_{i\alpha}. \tag{6.4}$$

With this form of ψ the coupling constant is nothing but a *sign* function that has to insure the positivity of the square root argument; when computing (6.3) $\mathcal{G} = \mathrm{sgn}(p^\star)$ has to be stored in order to compute (6.4), which takes the final form:

$$F_\alpha\left(\mathbf{x}, t\right) = -c_s^2 \sqrt{\frac{2|p^\star\left(\mathbf{x}, t\right)|}{c_s^2}} \sum_i w(|\mathbf{e}_i^2|)\ \mathrm{sgn}(p^\star)\ \sqrt{\frac{2|p^\star\left(\mathbf{x} + \mathbf{e}_i, t\right)|}{c_s^2}} e_{i\alpha}. \tag{6.5}$$

This *sign saving* strategy was shown to be a potential cause of instabilities [92]. In fact, Taylor-expanding the summation in (6.5)the approximation error is given by:

$$\frac{1}{2}\sqrt{\frac{2|p^\star|}{c_s^2}} \nabla \left\{ \Delta[\mathrm{sgn}(p^\star)] \sqrt{\frac{2|p^\star|}{c_s^2}}|_{\boldsymbol{\xi}, t} \right\}, \tag{6.6}$$

where $\boldsymbol{\xi} \in [\mathbf{x}, \mathbf{x} + \mathbf{e}_i]$. Since the derivative of square root is not bounded close to zero the error expressed by (6.6) can get arbitrarily high in the case $p^\star$ has a root in the interval $[\mathbf{x}, \mathbf{x} + \mathbf{e}_i]$. This risk can be avoided by getting rid of the square root; since (5.1) can be rewritten as $\mathbf{F} = -\boldsymbol{\nabla}(0.5\mathcal{G} c_s^2 \psi^2)$ it is possible to discretize ψ^2 instead of ψ [92]:

$$F_\alpha = -\sum_i w(|\mathbf{e}_i^2|)p^\star(\mathbf{x}+\mathbf{e}_i\ ,t)e_{i\alpha}. \tag{6.7}$$

Whatever is the form of forcing adopted it is important to underline that any EOS available in the literature can be incorporated into the SC formulation using (6.3). A given EOS is characterized by the relations between constants a and b and the critical temperature, pressure and density. Following [9] other EOS which are known for being more complex but at the same time more accurate than the vdW have been considered in this study, namely:

- Redlich-Kwong (RK): EOS

$$p = \frac{\rho RT}{1-b\rho} - \frac{a\rho^2}{\sqrt{T}\,(1+b\rho)}, \tag{6.8}$$

  with

$$a = \frac{0.42748R^2T_c^{2.5}}{p_c}, \quad b = \frac{0.08664RT_c}{p_c} \tag{6.9}$$

- Redlich-Kwong-Soave (RKS):

$$p = \frac{\rho RT}{1-b\rho} - \frac{a\alpha(T)\rho^2}{1+b\rho} \tag{6.10}$$

$$\alpha(T) = \left[1+\left(0.480+1.574\omega_A - 0.17{\omega_A}^2\right)\left(1-\sqrt{T/T_c}\right)\right]^2 \tag{6.11}$$

$$a = \frac{0.42748R^2T_c^{2}}{p_c}, \quad b = \frac{0.08664RT_c}{p_c} \tag{6.12}$$

  where ω_A is termed *acentric factor* .

- Peng-Robinson (PR):

$$p = \frac{\rho RT}{1-b\rho} - \frac{a\alpha(T)\rho^2}{1+2b\rho-b\rho^2} \tag{6.13}$$

$$\alpha(T) = \left[1 + \left(0.37464 + 1.54226\omega_A - 0.26992{\omega_A}^2\right)\left(1 - \sqrt{T/T_c}\right)\right]^2 \quad (6.14)$$

$$a = \frac{0.45724R^2T_c^2}{p_c}, \quad b = \frac{0.0778RT_c}{p_c} \quad (6.15)$$

- Carnahan-Starling (CS) [93]

$$p = \rho RT\frac{1 + b\rho/4 + (b\rho/4)^2 - (b\rho/4)^3}{(1 - (b\rho/4))^3} - a\rho^2 \quad (6.16)$$

$$a = \frac{0.4963R^2T_c^2}{p_c}, \quad b = \frac{0.18727RT_c}{p_c} \quad (6.17)$$

RK, RKS and PR are all cubic EOS: when compared to the vdW they model differently the attraction term of the vdW. On the contrary, in CS the repulsive term is different. The presence of the acentric factor in RKS and PR gives these EOS more flexibility to model real fluids, because ω_A is specific for each substance. In what follows the results have been evaluated in terms of *reduced variables*:

$$\rho_R = \frac{\rho}{\rho_c}, \quad p_R = \frac{p}{p_c}, \quad T_R = \frac{T}{T_c}, \quad (6.18)$$

where the subscript "c" identifies the critical properties. In this way one may easily pass from the lattice to the physical value of a certain property. Concerning the parameters, the choice was $a = 9/49$ and $b = 2/21$ for the vdW EOS, while RK, RKS and PR EOS are evaluated with $a = 2/49$ and $b = 2/21$; finally for the CS EOS $a = 1$ and $b = 4$. The gas constant R is set equal to 1 for all the EOS. The relaxation time is 1 as well. These values are taken from [9]. The first test consists of comparing the coexistence curve obtained by numerical simulations (flat interface test) with the theoretical curve predicted by the Maxwell equal-area construction introduced in chapter 4. Equation (4.4) is evaluated either with the "sign saving strategy" (Equation (6.5)) or as proposed in [92] (Equation (6.7)). The case of CS-EOS is illustrated in Figure 6.1, from which it is possible to see an excellent agreement when (6.5) is used: the maximum density ratio achieved was about 3250

at $T_R = 0.5$. When discretizing ψ^2 instead of ψ the simulations were unstable at the density ratios higher than $\mathcal{O}(10)$ for all the EOS. This order of magnitude is more or less what can be achieved by using the vdW-EOS. In [92] just the vdW was the only EOS for which the coexistence curve was computed using $a = 9/8$, $b = 1/3$ and $R = 1$. The use of this set of parameters did not improve the results here. It is thus possible to conclude that the set of parameters used in [9] do not cause the change of sign of (6.6), while the reason for the instabilities when using equation (6.7) is coincident with the first term of the body force in [94]:

$$F_\alpha = \partial_\alpha p^\star + \rho k \partial_\alpha (\partial_\beta \partial_\beta \rho). \tag{6.19}$$

This form of the body force is referred to as *potential form* in [57]. The second contribution missing in (6.7) is associated with the interfacial stress and should balance the thermodynamic pressure gradient. The effect of this term is to avoid a step-function-like profile at the interface, which would cause instabilities [94].

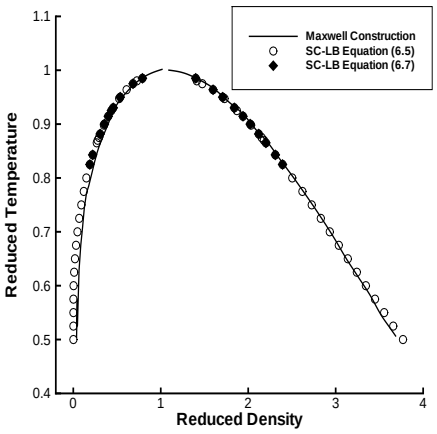

Figure 6.1: Comparison between analytical and LB-computed coexistence curve for CS-EOS using ether (6.5) or (6.7). The parameters are $a = 1$, $b = 4$ and $R = 1$.

The second test consists of taking a single spherical droplet in a fully periodic domain and in evaluating the maximum density ratio achievable and the corresponding value of the spurious current $|\mathbf{u}|_s$. The grid size is $51\times$ 51 $\times$ 51 and the initial radius is $10\Delta x$. For PR and RKS the acentric factor is $\omega_A = 0.344$, corresponding to water. Table 6.1 reports the results which are substantially coincident with those

presented in [9]. The interface thickness was measured as function of T_R in Figure 6.2 for the CS-EOS with (6.5). It is possible to observe how it diverges as $T_R \to 1$. The minimum value is instead ≈ 2.1 for $T_R = 0.55$.

EOS	$\lambda_{\max}$	$T_R^{\min}$	$\lvert\mathbf{u}\rvert_s$
SC	60.3	0.58	0.09
vdW	13.9	0.72	0.015
RK	117.65	0.65	0.0687
RKS	85.27	0.79	0.087
PR	2687.7	0.585	0.137
CS	1352.27	0.525	0.14

Table 6.1: Comparison of maximum density ratios achieved with different EOS as reported in [9] and [10]. The corresponding reduced temperatures and module of spurious currents are also reported. For SC-EOS is intended (4.10).

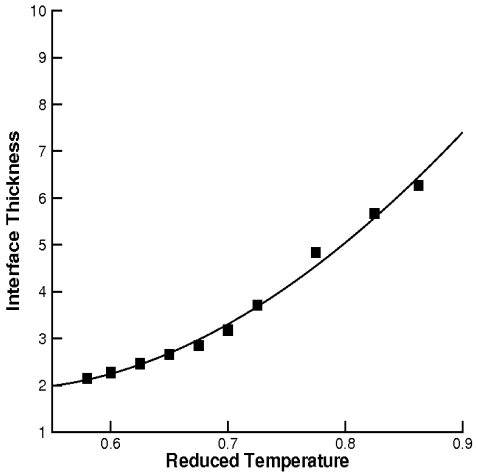

Figure 6.2: Interface thickness as function of reduced temperature for CS-EOS with $a = 1$, $b = 4$ and $R = 1$. Continuous line represent the best fitting for the computed values.

6.2 Carbon dioxide flow in microchannels

The usage of carbon dioxide, CO_2, as a refrigerating fluid in microsystems is getting more and more consideration because of its particular critical properties: since $T_c = 31°C$, CO_2 vaporization occurs at near critical pressure. That means high vapour density and low surface tension and liquid viscosity in operational conditions. In this section the CO_2 coexistence curve was taken as a benchmark to test for the SC-LB with the original effective mass expressed by equation (4.5) as well as with the new form that incorporates the previously defined EOS (equation (6.3)). In [9] the ability of the different EOS to reproduce real fluid properties were evaluated considering the system water/steam. The simulations suggested PR as the best EOS for the steam side of the coexistence curve, while RK was the best in approximating the branch of the curve related to the liquid state. The acentric factor to be used for RKS and PR EOS is CO_2 $\omega_A = 0.228$ for carbon dioxide (while for H_2O $\omega_A = 0.335$). The results can be seen in Figure 6.3 relative to the reduced temperature range $[0.85, 1]$ in which this fluid is used: the best EOS results are for the RKS for both the branches of the coexistence curve, while the PR completely fails in approximating the liquid branch; exactly the opposite behaviour can be seen for the CS-EOS (even if the error is reduced). Finally, the behaviour of vdW-EOS is the worst, confirming the low accuracy of this EOS.

In [6] the different flow regimes of liquid/gas CO_2 were observed in a microchannel at various mass flux and vapour volume fractions ϕ_V. The experiments revealed a prevalence of slug flow and annular regimes respectively at low and high ϕ_V. The slug flow regime is characterized by the aggregation of the bubbles in plugs which are often *bullet shaped*: the plugs are separated by liquid regions where small dispersed bubbles can occur. The annular flow regime consists in liquid layers at the tube walls surrounding the vapor flow in the core. In this last cases, droplet entrainment was often observed. Here a qualitative comparison has been performed, similar to what was done in [5], where an improved version of the free-energy LB with vdW-EOS was employed. The formulation reported in [5] corrects lack of Galilean invariance typical of the standard free-energy model by adding a new term to the pressure tensor which depends on the density gradient [95]; besides, this model has the peculiarity of having the coefficient of equation (6.1) dependent on temperature and it allows the extimation of the exact thickess of the LB-simulated interface.

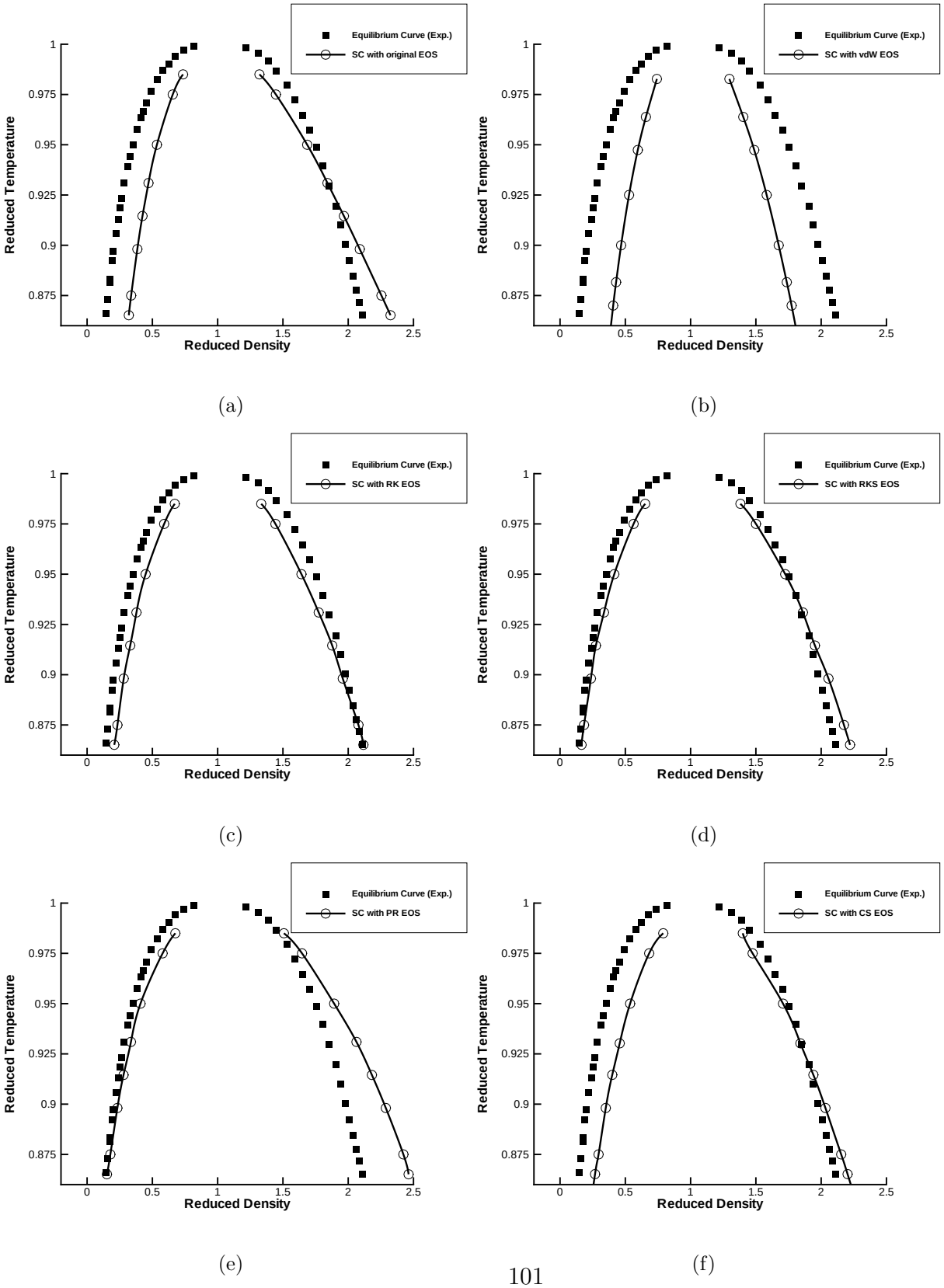

Figure 6.3: Comparison of experimental and simulated CO_2 coexistance curve for different EOS implemented into the SC model: a) Original SC EOS (Equation (4.10)). b) vdW EOS; c) RK EOS; d) RKS EOS; e)PR EOS; f) CS EOS.

The fluid simulated in [5] is CO_2 scaled with a dimensionless parameter X, so that real fluid properties are recovered when $X \to 1$. The same scaling is adopted here. Gravitational effects are ignored, and temperature is kept constant, while thermal effects are considered in [5]. A total amount of randomly distributed vapour bubbles corresponding to the desired ϕ_V is placed in a two-dimensional channel. Bounce back and Periodic BC are imposed respectively on walls and inflow/outflow sections, and the flow is assumed to be fully-developed pressure driven, with $\boldsymbol{\nabla} p$ corresponding to the desired mass flow.

The first case considered is taken from [5]: the lattice is 513×513 and the temperature, vapour volume fraction and mass flow are respectively $T = 25°\text{C}$, $\phi_V = 0.5$ and $G = 900$ kg/m^{2}s. Periodic boundaries are adopted for inflow/outflow sections, while the channel walls are modelled with the BBK scheme. Finally the scaling parameter X is set equal to 60. The evolution of the flow from bubbly to annular can be appreciated in Figure 6.4: from top to bottom, it is possible to observe the flow field at various channel locations normalized by the channel height as reported in [5], in this study [96] and in the corresponding experimental case from [6].

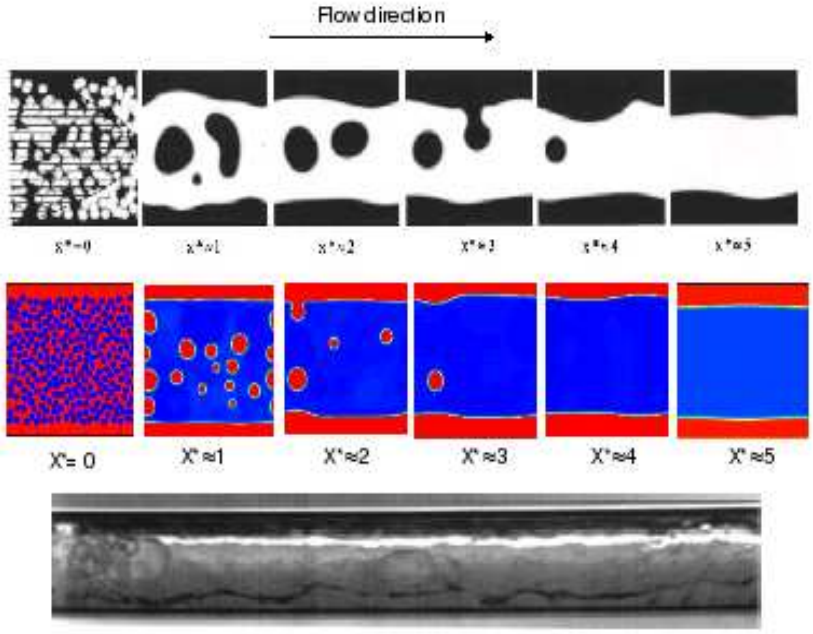

Figure 6.4: From top to bottom, the computation of CO_2 annular flow in [5], the simulation in the current study (the liquid is represented in red) and a similar experiment in [6]

It should be noted that the results of a temporal simulation at different time instants correspond to different streamwise locations in the experimental visualization. Very large liquid droplets form and then evaporate. Such features are harder to identify in experiments [6]. The annular flow regime develops quicker in the present study than in [5], but that is consistent with the random initialization of the process. The qualitative agreement with [6] is satisfactory.

The next case considered shows the development of slug flow from a low vapour volume fraction: the lattice in this case is 257×1025, and the corresponding experimental case is $T = 20°\text{C}$, $\phi_V = 0.35$ and $G = 250$ kg/m^{2}s. Once again the expected flow regime is correctly reproduced by the LB simuation, as it can be appreciated in Figure 6.5.

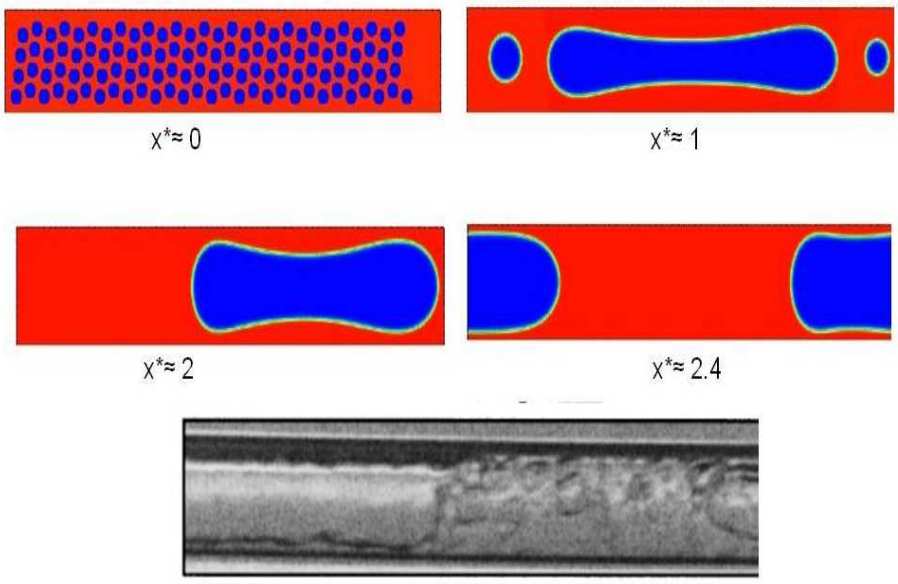

Figure 6.5: From top to bottom, the evolution from bubbly to slug flow for CO_2 in the current study (the liquid is represented in red) and a similar experiment in [6].

6.3 Origin of the spurious currents

In [97] the origin of the spurious currents compromising the stability of the SC model especially at high density ratios was showed to lay in the insufficient order of isotropy of the discretized gradient operator in equation (4.4). In fact, Taylor-expanding this equation it is possible to write:

$$F_\alpha = -\mathcal{G}c_s^2\psi(\mathbf{x})\left(E^{(2)}_{\alpha\beta}\partial_\beta\psi(\mathbf{x}) + \frac{1}{3!}E^{(4)}_{\alpha\beta\gamma\delta}\partial_{\beta\gamma\delta}\psi(\mathbf{x}) + \frac{1}{5!}E^{(6)}_{\alpha\beta\gamma\delta\theta\zeta}\partial_{\beta\gamma\delta\theta\zeta}\psi(\mathbf{x}) + \right. \\ \left. + \frac{1}{7!}E^{(8)}_{\alpha\beta\gamma\delta\theta\zeta\xi\kappa}\partial_{\beta\gamma\delta\zeta\xi\kappa}\psi(\mathbf{x}) + \dots\right), \tag{6.20}$$

with zero odd tensors because of lattice symmetry and even m-order tensors given by:

$$E^{(m)}_{\alpha_1\alpha_2..\alpha_m} = \sum_l w(|\mathbf{c}|_l)c_{l\alpha_1}c_{l\alpha_2}...c_{l\alpha_m}. \tag{6.21}$$

In order to correctly approximate the gradient the first term of left-hand side of equation (6.20) is required to be the unit tensor, $\delta_{\alpha\beta}$. As previously stated, the effective mass ψ depends on density ρ. For the case of a static droplet ρ has an axisimmetric (in 2D) or a spherical distribution (in 3D). It follows that $\boldsymbol{\nabla} f$ should possess the radial component only, which can be accomplished only if all the lattice tensors appearing in (6.20) are isotropic. Unfortunately whatever the numerical scheme used to discretize the gradient, the finite set of velocity vectors will make this constraint impossible to fulfill for higher order tensors $E^{(m)}_{i_1 i_2..i_m}$. That will *always* cause an azimuthal component to exist, which on turn will generate circulating flow around the interface like Figure 4.3b illustrates. The most commonly used scheme to discretize the gradient in equation (4.4), given by equation (4.6), insures the isotropy of the first two terms on left-hand side of (6.20). What can be done to improve the accuracy of left-hand side of (6.20) is to make higher order lattice tensors isotropic up to a certain order n. Of course that means to find a proper set of N_l lattice vectors $\mathbf{c}_l|\{l = 0 \dots N_l - 1\}$ and the corresponding set of weights $w(|\mathbf{c}|_l)$. This was done in [97] reaching isotropy up to 8th order in both 2D and 3D and extended in [73] where 16th and 10th order were reached respectively for 2D and 3D cases.

Weights	$\mathbf{E}^{(4)}$	$\mathbf{E}^{(6)}$	$\mathbf{E}^{(8)}$	$\mathbf{E}^{(10)}$	$\mathbf{E}^{(12)}$	$\mathbf{E}^{(14)}$	$\mathbf{E}^{(16)}$
$w(1)$	$\frac{1}{3}$	$\frac{4}{15}$	$\frac{4}{21}$	$\frac{262}{1785}$	$\frac{68}{585}$	$\frac{19414}{228375}$	$\frac{285860656}{3979934595}$
$w(2)$	$\frac{1}{12}$	$\frac{1}{10}$	$\frac{4}{15}$	$\frac{93}{1190}$	$\frac{68}{1001}$	$\frac{549797}{10048500}$	$\frac{2113732952}{43779280545}$
$w(4)$		$\frac{1}{120}$	$\frac{1}{60}$	$\frac{7}{340}$	$\frac{1}{45}$	$\frac{175729}{7917000}$	$\frac{940787801}{43779280545}$
$w(5)$			$\frac{2}{315}$	$\frac{6}{595}$	$\frac{62}{5005}$	$\frac{50728}{3628625}$	$\frac{124525000}{8755856109}$
$w(8)$			$\frac{1}{5040}$	$\frac{9}{9520}$	$\frac{1}{520}$	$\frac{3029}{913500}$	$\frac{15841927}{3979934595}$
$w(9)$				$\frac{2}{5355}$	$\frac{4}{4095}$	$\frac{15181}{7536375}$	$\frac{2046152}{795986919}$
$w(10)$				$\frac{1}{7140}$	$\frac{2}{4095}$	$\frac{221}{182700}$	$\frac{14436304}{8755856109}$
$w(13)$					$\frac{2}{405045}$	$\frac{68}{279125}$	$\frac{18185828}{43779280545}$
$w(16)$					$\frac{1}{480480}$	$\frac{1139}{26796000}$	$\frac{13537939}{14009369774}$
$w(17)$					0	$\frac{68}{2968875}$	$\frac{231568}{3979934595}$
$w(18)$						$\frac{17}{1425060}$	$\frac{1516472}{43779280545}$
$w(20)$						$\frac{17}{5742000}$	$\frac{18769}{1591973838}$
$w_{50}(25)$						$\frac{1}{32657625}$	$\frac{184}{315867825}$
$w_{34}(25)$						$\frac{1}{32657625}$	$\frac{464}{795986919}$
$w(26)$							$\frac{1448}{4864364505}$
$w(29)$							$\frac{148}{4864364505}$
$w(32)$							$\frac{629}{400267707840}$

Table 6.2: Weights up to the 16th order approximation for two-dimensional lattice models. The weights for velocities $|\mathbf{c}_l| = 25$ have to be chosen differently according to the direction in the two-dimensional space. The notation $w_{ab}(|\mathbf{c}_l|)$ stands for the velocity vector $(\pm a, \pm b)$ plus permutations.

Here the vectors required for each order of isotropy, as well as the corresponding weights are reported in Table 6.2 for 2D and in Table 6.3 for 3D simulations. The interested reader will find in [73] an extensive explanation on how to calculate these coefficients.

Weights	$\mathbf{E}^{(4)}$	$\mathbf{E}^{(6)}$	$\mathbf{E}^{(8)}$	$\mathbf{E}^{(10)}$
$w(1)$	$\frac{1}{6}$	$\frac{2}{15}$	$\frac{4}{45}$	$\frac{352}{5355}$
$w(2)$	$\frac{1}{12}$	$\frac{1}{15}$	$\frac{1}{21}$	$\frac{38}{1071}$
$w(3)$		$\frac{1}{60}$	$\frac{2}{105}$	$\frac{271}{14280}$
$w(4)$		$\frac{1}{60}$	$\frac{2}{105}$	$\frac{271}{14280}$
$w(5)$			$\frac{1}{315}$	$\frac{53}{10710}$
$w(6)$			$\frac{1}{630}$	$\frac{5}{2142}$
$w(8)$			$\frac{1}{5040}$	$\frac{41}{85680}$
$w_{221}(9)$				$\frac{1}{4284}$
$w_{300}(9)$				$\frac{1}{5355}$
$w(10)$				$\frac{1}{10710}$
$w(11)$				$\frac{1}{42840}$

Table 6.3: Weights up to the 10th order approximation for three-dimensional lattice models. The weights for velocities $|\mathbf{c}_l| = 9$ have to be chosen differently according to the direction in the three-dimensional space. The notation $w_{abc}(|\mathbf{c}_l|)$ stands for the velocity vector $(\pm a, \pm b, \pm c)$ plus permutations.

	$\mathbf{E}^{(4)}$	$\mathbf{E}^{(6)}$	$\mathbf{E}^{(8)}$	$\mathbf{E}^{(10)}$	$\mathbf{E}^{(12)}$	$\mathbf{E}^{(14)}$	$\mathbf{E}^{(16)}$
2D	8	12	24	36	48	80	100
3D	18	32	92	170	-	-	-

Table 6.4: Number of nodes necessary to determine gradients isotropic up to different orders for both 2 ($\mathcal{L}$ =D2Q9) and 3D ($\mathcal{L}$ =D3Q19) cases.

To check the effect of increasing the isotropy of the gradient operator, a simulation of a static 3D drop was run using CS-EOS with the usual parameters, $\tau = 1$ on a 51×51×51 grid. The initial radius was 16. Gradient schemes with isotropy of 4, 6, 8 and 10 were tested. The local Ma number representing the spurious currents was measured at the end of the simulation for $x = y = 25$ and reported in Figure 6.6. A significant reduction of the local Ma (about 2.5 times) can be observed when increasing the order of isotropy from 4 to 10, but this result has to be evaluated considering also the increased computational cost.

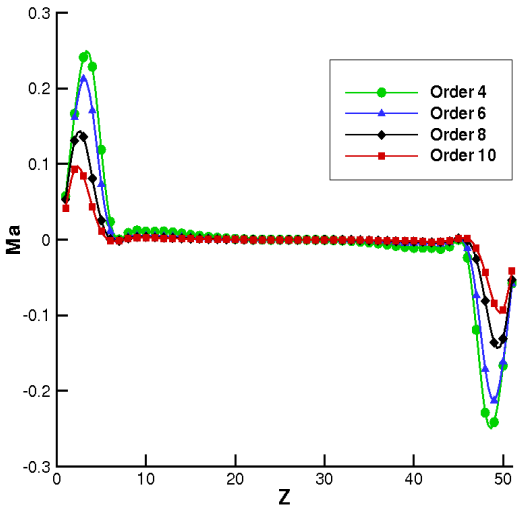

Figure 6.6: Interface thickness as function of reduced temperature for CS-EOS with $a = 1$, $b = 4$ and $R = 1$.

In fact, as can be read in Table 6.4, the number of nodes required for a gradient 10th order isotropic is almost 10 times that for the case of 4. That made the

execution time 2.73 times higher than what required for standard 4-th order isotropic scheme. Besides the presence of non-periodic boundaries make the implementation of higher-order schemes more difficult. The use of this technique has to be therefore carefully considered. This is the first time in which this strategy is applied together with effective masses different from the original SC model. In fact, in [73] equation (4.5) was used with $\rho_0 = 1$. The reduction of the local Mach number when increasing the isotropy from 4 to 10 was about the same measured here.

6.4 Combining SC, EDM and MRT schemes

So far the simulations were all conducted at $\tau = 1$. What happens when $\tau \to 0.5$? Considering always the static 3D droplet case with , the SRT-LB gets unstable already at $\tau < 0.75$ when the reduced temperature corresponds to a high density ratio. That happens for all the EOS, and it is not surprising. The MRT formulation illustrated in chapter 5 is expected to improve the situation. Considering always the CS-EOS with the usual set of parameters, this formulation allowed us to reach a minimum viscosity of 1/384 at $T_R = 0.8$, when the density ratio is about 15. A further reduction of T_R made the minimum viscosity achievable dropping down by $\mathcal{O}(10)$. As stated in chapter 4, in the standard SC formulation the application of the body force given by equation (4.7) led to a modified velocity in the f_i^{eq} according to Method I discussed in chapter 3 (Equation (3.25)). What if the EDM is applied instead? The whole LB equation takes the form:

$$\mathbf{f}\left(\mathbf{x}+\mathbf{e},t+1\right)-\mathbf{f}\left(\mathbf{x},t\right)=-\mathbf{M}^{-1}\mathbf{S}\left(\boldsymbol{\varrho}-\boldsymbol{\varrho}^{eq}(\mathbf{u})\right)+\left(\mathbf{f}^{eq}(\mathbf{u}+\Delta\mathbf{u})-\mathbf{f}^{eq}(\mathbf{u})\right), \quad (6.22)$$

where $\Delta\mathbf{u} = \frac{\mathbf{F}\Delta t}{\rho}$.

The result of the application of EDM can be seen in Figure 6.7, where the maximum Mach number is plotted as function of ν at $T_r = 0.65$, which corresponds to a density ratio of 150. The range of viscosities at which the simulations are stable is the same as those obtained by MRT with SC implemented with method I, but at a density ratio 10 times higher. The MRT-SC LB without EDM scheme allowed us to reach at this same temperature a minimum viscosity of $\approx 1/20$.

This result proves the EDM allows a more effective incorporation of a generic body force into the LB formulation than method I exposed in chapter 3, which is the standard choice for SC model. The second order accuracy in terms of velocity gradient guaranteed by the EDM is fundamental to improve stability at high density ratios, where the relevant density gradients between liquid and gaseous phases induce, especially at the beginning of the simulation, strong velocity gradients.

At the end of this chapter it is therefore possible to conclude that the basic SC model can be significantly improved. The combination of well-known cubic EOS, higher-order schemes for gradient calculation, MRT and finally EDM has been realized for the first time in this study and is the main achievement of this research.

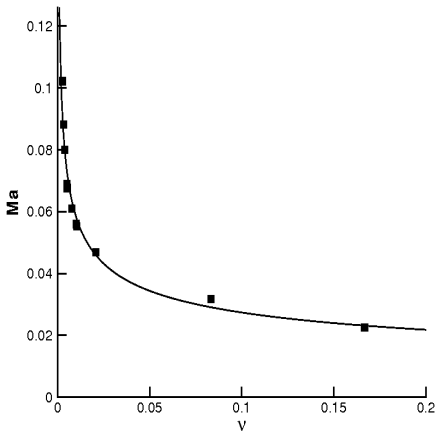

Figure 6.7: Maximum module of spurious currents as function of kinematic viscosity at $T_R = 0.65$ for the CS-EOS with $a = 1$, $b = 4$ and $R = 1$.

Chapter 7

Binary droplet collisions

In the previous two chapters it was illustrated how to address the issues of achieving low Reynolds numbers and density ratios with the combination of LBGK and SC models. The use of a more realistic EOS and the increased isotropy of the gradient operator were shown to address the first issue, while the incorporation of body forces using the EDM and the MRT scheme provided the desidered stability at low viscosities. This combination has therefore the potential to greatly extend the capabilities of LB in the field of multiphase flows. In this final chapter this improved formulation is applied to the simulation of binary droplet collision. The first part of this chapter concerns the description of the physics involved and the review of existing literature, including other works based on LB. The consistency of LB with experiments and analythical models is demonstrated in the second part of the chapter.

7.1 Introduction

Droplet collisions are encountered either in natural phenomena or in many engineering applications like for instance rain formation and engine fuel sprays. The parameters characterizing this phenomenon are the densities and viscosities of liquid and gaseous phases, respectively ρ_l, ρ_g, μ_l and μ_g, the surface tension σ, the droplets radii R_1 and R_2, their relative speed $\mathbf{U_0}$ and finally their displacement χ in the direction normal to $\mathbf{U_0}$. These quantities are reported in Figure 7.1. The whole process is therefore described by six nondimensional quantities which are the

Weber and Reynolds numbers, respectively given by $We = \rho_l U^2(R_1 + R_2)/\sigma$ and $Re = \rho_l U(R_1 + R_2)/\mu_L$, the size, density and viscosity ratios, and finally the impact factor $B = \chi/(R_1 + R_2)$.

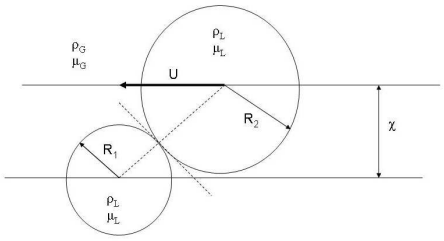

Figure 7.1: Physical and geometrical parameters characterizing binary droplet collision.

Experimental studies like [98, 99] considered water droplets in air, while in studies like [100, 101, 7] where more oriented to industrial applications, because the fluids involved where ethanol or C_4H_{30} in air or nitrogen. Five possible collisional regimes were identified in these studies: adopting the notation of [7], it is possible to observe *coalescence* (Regime I), *bouncing* (II), *coalescence with major deformation* (III), *head-on separation* (IV) and *off-centre separation* (V). These regimes can be identified by transition curves in the $B-We$ plane. Coalescence occurs at very small We, when the gas is pulled out of the gap between the approaching droplets till the thickness of this gap reduces to the order of molecular interaction. If the minimum thickness is higher than this value, the droplets will not touch, and bouncing will instead occur. Regime III occurs at intermediate We, when the initial kinetic energy is sufficient only to cause extensive deformation to the coalesced droplet, but not to break this one in two. At high We number it is possible to observe Regimes IV or V,depending on B. In these two regimes the coalesced droplet can experience either disruption, that produces again two droplets,or fragmentation, producing catastrophic break-up into many small droplets. All the different collision regimes are represented in Figure 7.2, either as regions in the plane $B-We$ or with pictures taken by the experiments reported in [7].

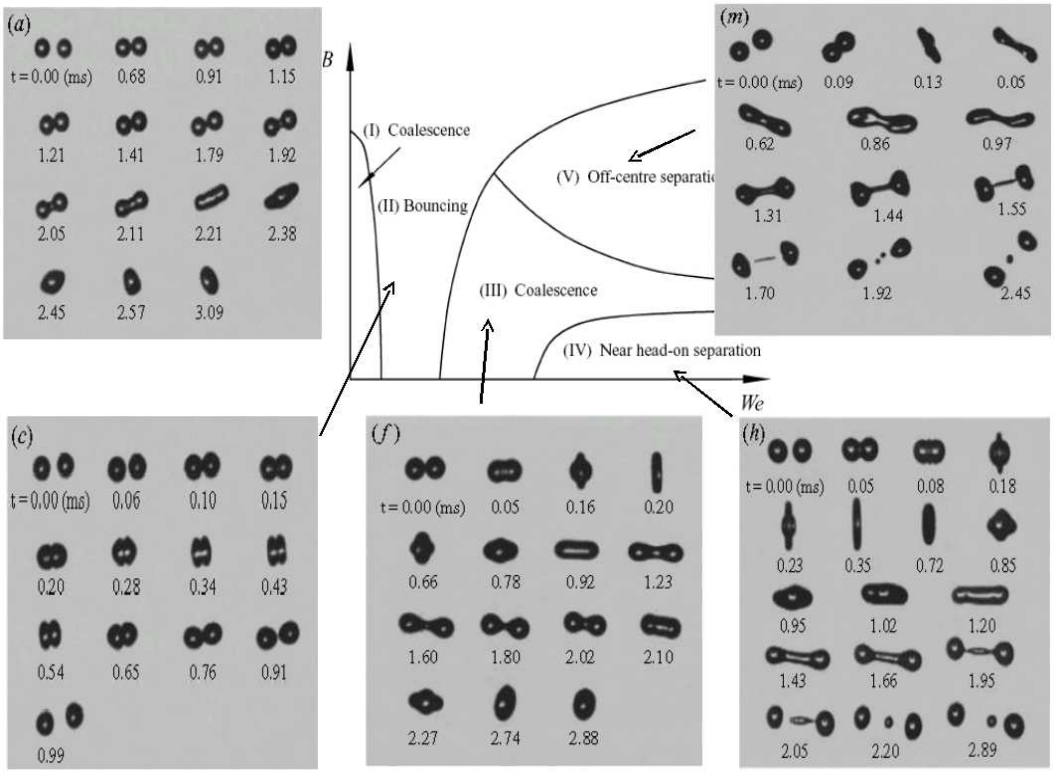

Figure 7.2: Summary of all possible collision outcomes. Pictures of post-collisional outcomes are taken from [7].

7.2 Review of other numerical studies

Droplet collisions represent a challenging case for numerical simulations, because of the necessity of following the evolution of variable interfaces. The goal of these investigations was also to provide to the CFD community a series of images of the collisional dynamics to use as benchmark for their numerical methods.

Concerning methods that are based on NS equations, one of the first works was [102] in which the head-on collision of two-dimensional droplets were studied via the marker-and-cell (MAC) method. Axisymmetric and fully three-dimensional front-tracking methods were employed in [103] and [104] to study respectively head-on and off-centre collisions; altough many interesting results are reported the authors note

that bouncing and coalescence regimes were obtained by artificially prescribing the rupture of a thin gaseous film. Volume of fluid (VOF) was instead used in [105] and [106]; this last work studies again head-on collision in an axisymmetric reference: two VOF indicator functions are used, one for each droplet, to track the interfaces, while a local grid refinement strategy is adopted in order to increase resolution around droplet interfaces. Regimes I-IV were observed in this way and compared with [7]. In [8] regime I was studied using the Galerkin finite-element method in conjunction with the spine-flux method for interface tracking. The Level-set method is instead used in [107], providing remarkable agreement either with the experiments of [7] or [99] except for regime I which was not possible to observe. All these methods require some artificial technique for interface tracking.

Droplet collision has also been simulated with LB; in [108] the original SC model was applied at a density ratio of ≈ 30; more important are the results reported in [109] and [110], relative respectively to collisions between equal- and unequal-size droplets at $Re = 2000$: the free energy method was applied in these two works, coupled with a projection method necessary to enforce a zero-divergent velocity field. The density ratio reported was 50 in both cases but the authors claim higher values can be reached, with an increase of computational cost due to the projection step. [111] coupled the MRT scheme with the HSD multiphase model to simulate head-on collisions in an axisymmetric implementation of the LB. Some fully 3D simulations where also reported. The density ratio was 4. Finally in [112] simulations of some cases from [7] were reported at density ratios varying from 50 to 70 using the SC-MRT LB.

7.3 Results

In this study, the LB method is adopted to simulate three-dimensional binary droplet with equal size colliding at different values of We , Re and B. The lattice structure $\mathcal{L}$ used is the $D3Q19$ model. The goal is to explore all the regions of $B - We$ plane in order to verify the ability of the LB in reproducing the five different collision regimes previously described. To do that, the single-component two phase SC model is adopted. The EOS used to compute ψ in equation (4.1) is the Carnahan-Starling (equation (6.16)) with the same parameters seen in the previous chapter. The sign-

saving strategy is adopted to numerically implement the SC model via equation (6.5). Finally, in (6.5), the discrete gradient operator has sixth order isotropy (all the corresponding vectors and weights are listed in Table 6.3). For each case the known quantities in lattice units are the density ratio and the corresponding surface tension obtained with the static droplet case. Once chosen the initial radii what remain to determine are the initial relative speed and the kinematic viscosity. The definitions of We and Re provide the necessary equations to calculate them. As seen in the last chapter if $\tau \leq 0.75$ the SRT formulation is usually unstable and the MRT-LB coupled with EDM is adopted (6.20). In this case the relaxation times are equal to 1 except $s_9 = s_{11} = s_{13} - s_{16} = 1/\tau$ [83] (see Appendix B). The first tests conducted reproduce the cases reported in the first part of [8] where pure coalescence was studied for equally sized droplets colliding at $B = 0$ in vacuum. The We is fixed to 1, while Re ranges from 5 to 60. Considering a cylindrical coordinate system z, r with origin fixed at the collision point and z directed along the symmetry axis, this kind of collision is characterized by essentially four steps: initial deformation, during which a radially expanding disc, called a *lamella*, is produced; the lamella expands radially since the fluid inside moves towards the extremes; depending on the amount of inertia a rim bounding the lamella can be formed. Subsequently the lamella collapses in a jet that expands along z until the deformation is a maximum; finally the extremes move back towards the origin and a new oscillation takes place till the coalesced drop reaches a spherical shape. The same kind of test was repeated here, at four Reynolds numbers: 5, 10, 30 and 60. LB would be unstable without any fluid outside the droplets, so a density ratio of 400 was chosen. The droplets are resolved with $R_1 = R_2 = 32$ lattice nodes. For $Re = 5$ and $Re = 10$ the relaxation time was close to 1 and SRT was used; that was not the case for the last two Re, in particular for $Re = 60$ where $\tau = 0.54$. The maximum deformation on both axes as well as the period of the first oscillation are reported for each Re in Figure 7.3 (a) and (b). Viscous effects act on both axes, but since they are proportional to velocity gradients it is expected a major dissipation along radial direction; that is confirmed by Figure 7.3, from which a similar elongation along the radial direction can be observed for $Re \geq 10$. The comparison with the corresponding results from [8] shows quite good agreement.

After this first test the collision reported in [7] are considered. It is important to underline that the experiments are characterized by a density ratio of ≈ 600 and

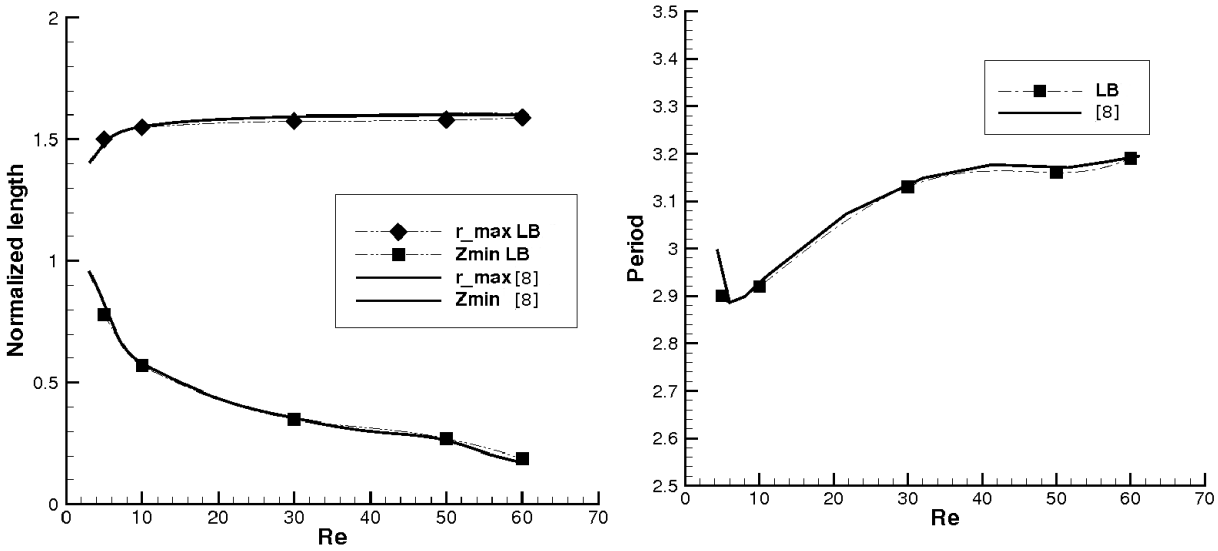

(a) (b)

Figure 7.3: Evaluation of coalesced droplet deformation at different Re: (a) Variation of minimum thickness along z, z_{min} and maximum radius r_{max} (b) Variation of first period of oscillation. In both pictures the results are compared with the corresponding cases reported in [8].

the viscosity ratio is ≈12, while here LB simulations run with a single-component model at lower density ratio, therefore the characteristic time of each simulation cannot match the value relative to the corresponding experimental case. Regime I is observed in Figure 7.4(b), corresponding to case"a" in [7], ($Re = 14.8$, $We = 0.2$ and $B = 0.2$). The grid is $201 \times 181 \times 181$ and the droplet radii are $40\Delta x$. At this regime, viscous and surface effects dominate over inertial ones and the droplets approach each other quite slowly. That holds of course also in lattice units, allowing only for this case to run the simulation at $T_R = 0.58$, corresponding to a density ratio of 1000. The coalesced drop takes a cylindrical shape, than tends to reach a spherical configuration in order to minimize surface energy, reproducing the trend observed in the experiments which is reported in Figure 7.4 (a). The following cases are always characterized by a density ratio of 150. Regime III is illustrated in Figure 7.5 and 7.6, corresponding respectively to cases "f" ($Re = 210.8$, $We = 32.8$ and $B = 0.08$) and "k" ($Re = 327.7$, $We = 70.8$ and $B = 0.25$) from [7]. The expected different behaviour under different B is clearly reproduced. In the first case, the tangential component of the impact inertia is almost zero, and a thin disk

is initially formed, that later contracts and forms a cylinder and then a dumbbell, without any rupture of the film. In the second case, the higher tangential component of the impact inertia is expected to cause an extensive rotational motion, and that is precisely what the simulation shows. In both cases the grid is $251 \times 141 \times 141$ and the droplet radii are $30\Delta x$.

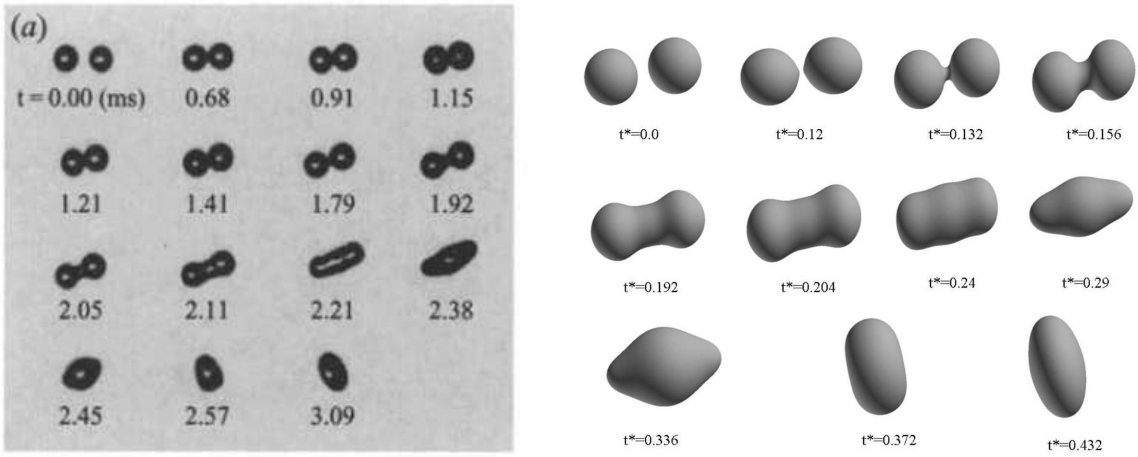

(a) (b)

Figure 7.4: Comparison between experiments from [7] (a) and LB simulation (b) for $Re = 14.8$, $We = 0.2$ and $B = 0.2$ (t*=tU/2R).

Figure 7.7 is related to case"g" (Regime IV) ($Re = 228$, $We = 37.2$ and $B = 0.01$): the evolution is similar to case "f" and previously seen, but this time initial kinetic energy is enough to overtake the surface tension force and split the coalesced drop. Again, good agreement is found with the experiments.

A further increase of B causes a reduction of the contact region: if We is high enough, like in case " m" ($Re = 302.8, We = 60.1$ and $B = 0.55$), Regime V is observed: the LB simulation in Figure 7.8 clearly reproduces the formation of a thin neck linking two main globules and its subsequent rupture by means of the so-called *end-pinching* mechanism, producing three droplets. Because of the off-centre collision a consistent rotation of the globules as well as the ligament connecting them can be observed.

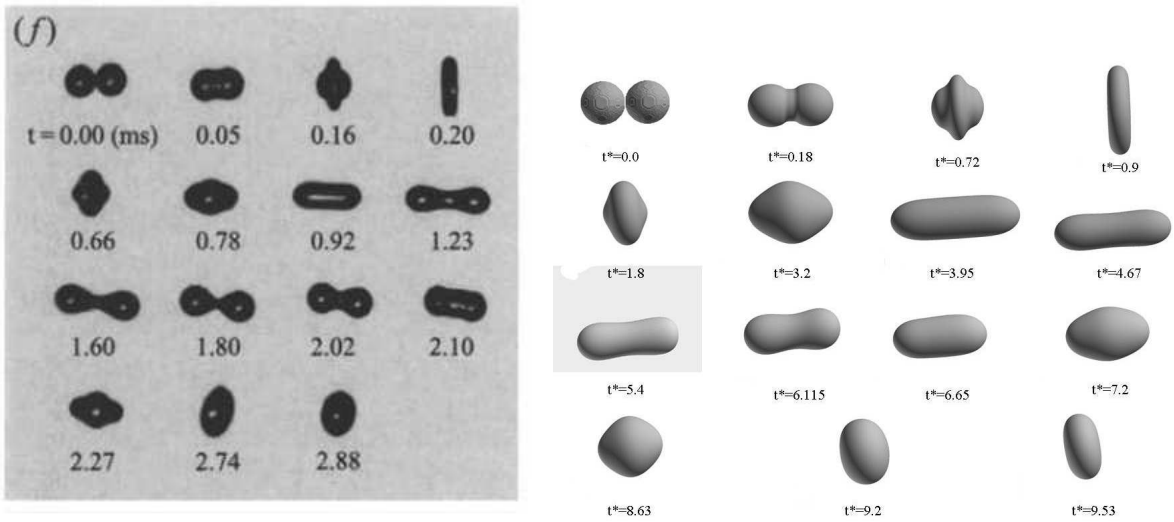

(a) (b)

Figure 7.5: Comparison between experiments from [7] (a) and LB simulation (b) for $Re = 210.8$, $We = 32.8$ and $B = 0.08$ (t*=tU/2R).

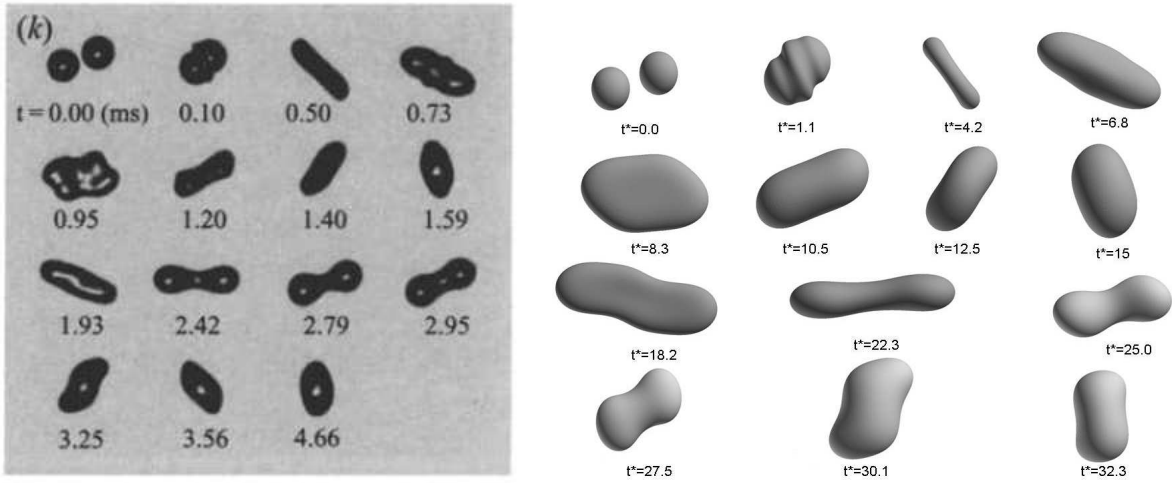

(a) (b)

Figure 7.6: Comparison between experiments from [7] (a) and LB simulation (b) for $Re = 327.7$, $We = 70.8$ and $B = 0.25$ (t*=tU/2R).

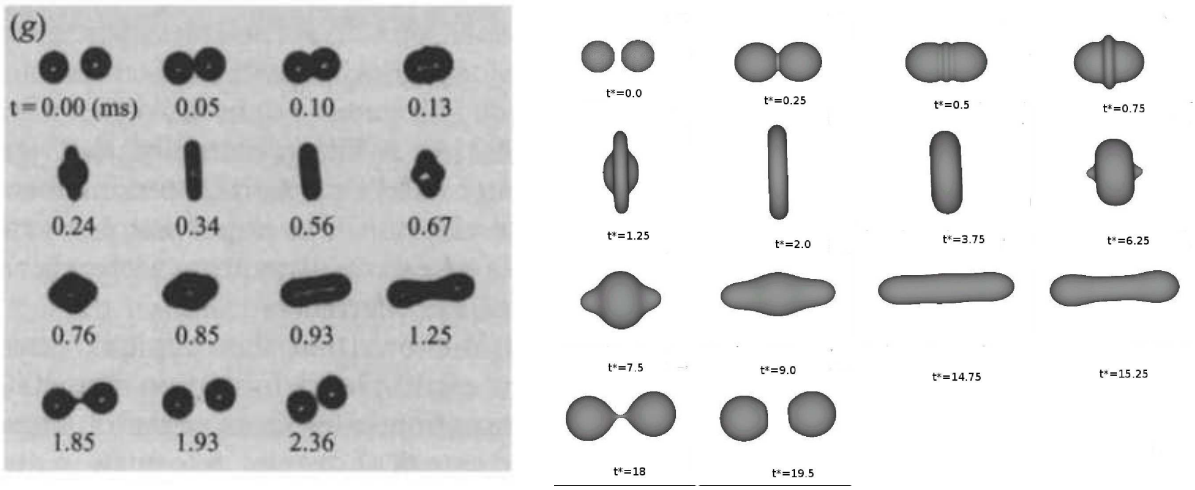

(a) (b)

Figure 7.7: Comparison between experiments from [7] (a) and LB simulation (b) for $Re = 228$, $We = 37.2$ and $B = 0.01$ (t*=tU/2R).

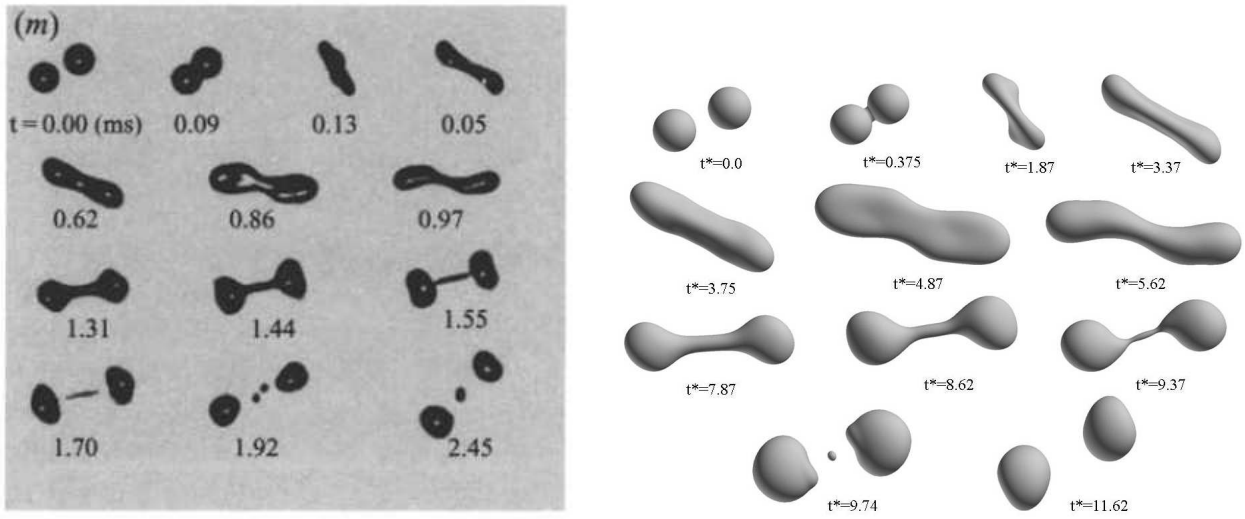

(a) (b)

Figure 7.8: Comparison between experiments from [7] (a) and LB simulation (b) for $Re = 302.8, We = 60.1$ and $B = 0.55$ (t*=tU/2R).

Considering the same geometry of the previous case but increasing the We the inertial effects are increased and the result is a further fragmentation of the first

child droplet, which splits into other 3 smaller drops with the same mechanism. Figure 7.9 summarizes this case.

Finally, case "o" from [7] is simulated. Here the impact factor reaches 0.71, so there is no rotation of the ligament, but just of the globules. That produces one elongated child droplet, which is driven by the surface tension to the minimization of its surface energy corresponding to a spherical-shaped final configuration, without any further rupture. The last row of Figure 7.10 illustrates in detail the final part of the collision process concerning the child droplet formed because of the double pinch-off at its extremes. This droplet undergoes a process similar to the last part of case "f" previously seen: the two globules formed as a consequence of the pinch-off merge in a lamella that later takes on a spherical shape. This demonstrates the ability of the model to catch complex dymanics at different scales.

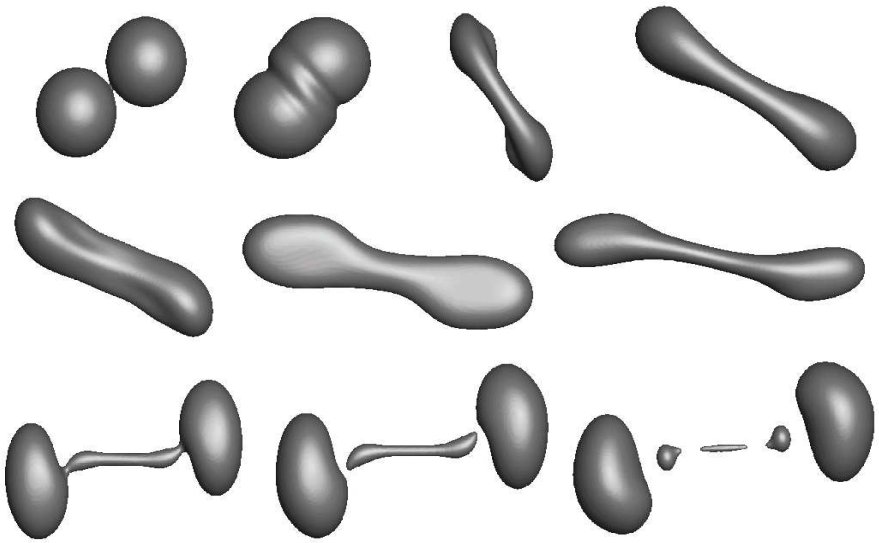

Figure 7.9: Off-centre collision at $We = 138$, $Re = 302.8$ and $B = 0.55$.

The formulation previously discussed allowed us to have stable simulations of all the cases reported in [7]. Figure 7.11 summarizes all the tests conducted. The regions of the $We - B$ plane corresponding to the expected regimes are separated by experimentally obtained curves. The different symbols represent the outcomes obtained by the LB simulations: spheres are associated to Regime I, squares to

Regime III, triangles and diamonds respectively to regimes IV and V. As can be seen in Figure 7.11 the simulations correcty predict the post-collisional regime in most of the cases. All the regimes were observed, except bouncing. The bouncing cases had always a pure coalescence outcome. In the author's opinion that may depend on insufficient resolution in the collision region, but most of all on an insufficient repulsion among the phases due to the single component scheme adopted.

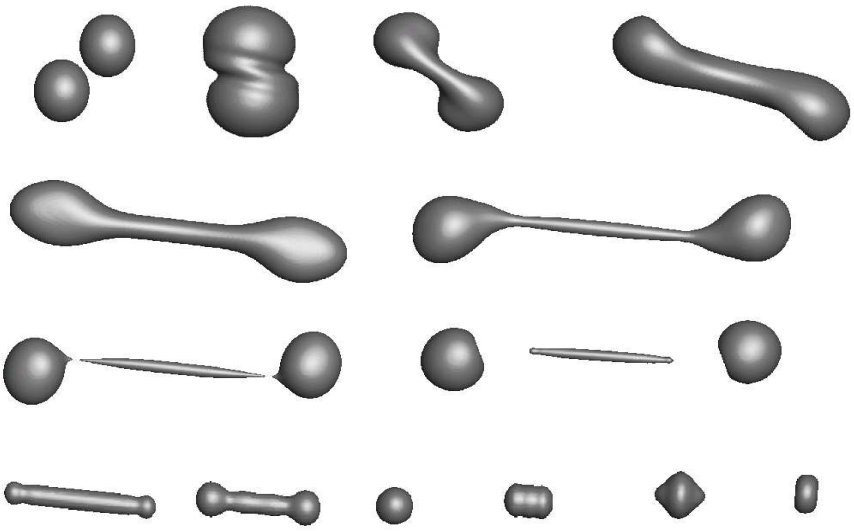

Figure 7.10: Off-centre collision at $We = 64.9$, $Re = 312.8$ and $B = 0.71$.

7.4 Discussion and Conclusions

The highest density ratio was 1000 for regime I at $Re = 14$. The low inertial regimes are the most stable at high density ratios. The next step might be to verify the LB reproduces the scaling law for the evolution of length and diameter of the bridge forming between the droplets (Figure 7.4b) proposed in [113]. Unfortunately when coming to collisions in regimes III, IV and V (high We-high Re cases) things are complicated by the overlapping of extremely high spurious currents with the imposed flow field, and it was not possible to mantain an experiment-like density ratio. For these regimes in fact it had to be decreased to 150. Investigation on how to further

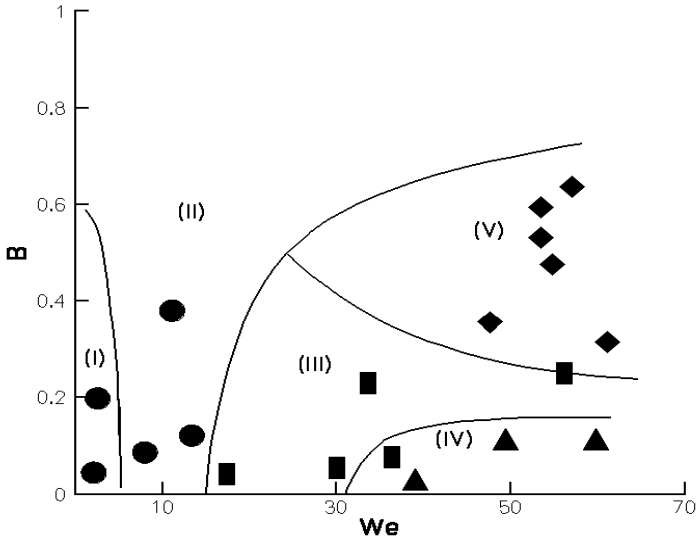

Figure 7.11: Summary of tests conducted and comparison with expected prediction by [7].

reduce the spurious currents is thus necessary. Nevertheless even at not too small reduced temperatures these regimes may prove impossible to reach, because of the low-Ma constraint of LB that might be violated by the initial relative speed U_0. In fact, as discussed before, once chosen the initial droplet diameter D_i, the definitions of We and Reynolds numbers are used as equations to determine the ν and U_0. If for instance the case with the highest We number reached (We =407,Re=134) is considered, each droplet was initialized with $U_0/2 = 0.22$, which is already well above a safe level ($U_0 \leq 0.1$). Since computational cost limits the freedom to increase the droplet diameter, a more convenient inital speed could be found if σ could be reduced. Unfortunately the impossibility of tuning the surface tension σ once fixed the density ratio is another defect of the SC model as stated in chapter 4, while this feature is instead offered by the free energy model as well as by the HSD model. Anyway the density ratios reached in this study are significantly higher than what reported in similar works by other authors [109] [110] [111]. Besides, the SC model does not require two different sets of PDFs like the models employed in the aforementioned works.

Conclusions

The simulation of complex gas-liquid flows with the lattice Boltzmann (LB) method has been the objective of this research work. During its first twenty years the LB has evolved from a simple real-value therapy to the statistical noise of the lattice gas cellular automata (LGCA) into a numerical scheme able to simulate realistic fluid dynamics. The thesis summarizes this process throughout its different chapters: what was emphasized is the different nature of LB when compared to classical Navier-Stokes based solvers. The fact that kinetic theory includes the continuum description justified the search for a numerical scheme which could not be affected by non-linearities coming from macroscopic description (chapter 2). Chapters 3 and 4 present the most simple formulations for both single- and multi-phase LB, namely the SRT-LB and the SC model. These chapters summarize, with some exceptions, the state of the method in 1994, when [52] appeared. Altough this 1994-LB was already capable to simulate flows like the deformation and breakup of a droplet under shear flow or the T-micromixer, it still was limited to highly viscous flows with low density ratios. Fifteen years are quite a long period, and many of the improvements proposed in these years for the SC model were reported in chapter 5 and in the first part of chapter 6. The last section of this chapter shows how all these new developements can be combined into a SC-type scheme possessing the following features:

- Different EOS incorporated with respect to that proposed in [52], which allow to reach high density ratios.
- Exact difference method (EDM) for a better inclusion of body force effect especially at low ν.
- Gradient operator with higher degree of isotropy to reduce spurious currents

at interfaces.

- Multiple-relaxation-time (MRT) formulation to improve the stability at high Reynolds.

This new extended SC model represents the main contribution of this research project, and has been succesfully applied in Chapter 7 to the simulation of binary droplet collision at density ratios higher than reported in other works. The qualitative and quantitative agreement respectively with the experiments reported in [7] and the with the results presented in [8] confirmed the validity of this new approach. The results related to this case, as well as those reported in chapters 4 and 6 open the possibilities for further studies. There is room for further improvement of the model too, as will be explained in the next section.

Future work

The binary droplet collision demonstrated that including EOS like the CS or PR may allow to reach realistic liquid-gas density ratios for the static droplet or flat interface cases, but it is not sufficient for rapidly moving interfaces. As seen in the previous chapter tuning the surface tension σ at a fixed density ratio may help, but this limitation has not been addressed in this study: ideally it would be preferable to mantain the SC model basic features (force term derived by a scalar potential, natural phase separation, one only set of f_i) and inserting some form of control of σ into this framework. A strategy for controlling the surface tension in a SC-like scheme was proposed for instance in [114], based on the incorporation into (4.1) of a further term $-k\boldsymbol{\nabla}\nabla^2\rho$. Another solution was proposed in [73] and consisted in the introduction of another coupling constant for this purpose. In the same paper it is shown how to significantly reduce the spurious currents by simply rescaling the effective mass. All these strategies were developed for the basic SC model with EOS given by (4.2). Their performance with different EOS like those tested in chapter 6 is unknown. As stated in chapter 6 discretizing the square of a scalar potential can be convenient, but a further term is requested at high density ratios. A solution could be given by the *stress form* of the forcing term given in [57] (Equation (12)), where this form is claimed to produce a smoother pressure profile across the interface

than the potential form (6.19). This work is based on the HSD model but this idea could be implemented into the SC model as well. Either the potential or the stress form are compatible with the EDM scheme. Finally further work is needed on the multicomponent SC model in terms of density ratio, which remains at best of $\mathcal{O}(10)$. Each of the applications presented in this thesis can be further extended. The T-micromixer for instance can be used as the starting point for examining many different problems: first of all the layouts could consist in circular obstacles with different radius, or in obstacles with totally different geometries (rectangular for example). Of course extension to three-dimensional flow should also be considered. This geometry is not limited to mixing problems, has a huge number of applications in microfluidics: for instance it is used to produce droplets in [115] a numerical investigation of the breakup dynamics of streams of immiscible fluids is conducted by using a phase-field model; another application is the *Membraneless Laminar Flow Fuel Cell* (LFFC) [116]-[117] where this geometry sees the parallel flow of fuel (hydrogen, methanol or formic acid) and oxidant streams not separated by a porous membrane as happens in conventional fuel cells. Getting rid of the membrane means not facing dryout at high temperatures (the membrane has constantly to be hydrated to work efficiently) as well as fuel crossover. Examples of LB applied to electrochemical and reactive flow problems are for instance [118] and [119], where suitable boundary conditions for modeling electrodes were defined, or [35] where the SC coupled with the EDM scheme was used to model the hydrodynamic flow, while the transport equations for charged species are solved by considering additional LB equations relative to zero-mass components (passive scalars).

Appendix A

Elements of tensor symmetry

A.1 General form of isotropic tensors

The set of orthogonal transformations O includes rotations and reflections. A tensor $T_{\alpha_1\alpha_2\ldots\alpha_n}$ is of n-th rank is defined *isotropic* if is invariant with respect to any ortogonal transformation:

$$T_{\alpha_1\alpha_2\ldots\alpha_n} = T_{\beta_1\beta_2\ldots\beta_n} O_{\alpha_1\beta_1} O_{\alpha_2\beta_2} \ldots O_{\alpha_n\beta_n}. \tag{A.1}$$

The following theorem [120] defines the forms of isotropic tensors up to 4-th rank:

- There are no isotropic tensors of rank 1 (vectors)
- Any isotropic tensor of rank 2 is proportional to $\delta_{\alpha\beta}$
- Any isotropic tensor of rank 3 is proportional to $\epsilon_{\alpha\beta\gamma}$ [1]
- There are 3 linear indipendent tensors of rank 4:

$$\delta_{\alpha\beta}\delta_{\gamma\delta}, \quad \delta_{\alpha\gamma}\delta_{\beta\delta}, \quad \delta_{\alpha\delta}\delta_{\beta\gamma}. \tag{A.2}$$

[1] *Levy-Civita* symbol $\epsilon_{\alpha\beta\gamma} : \epsilon_{123} = \epsilon_{312} = \epsilon_{231} = 1$, $\epsilon_{132} = \epsilon_{321} = \epsilon_{213} = -1$ and 0 otherwise.

It follows that the most general form for any rank 4 tensor is given by a linear combination of these 3 elementary tensors:

$$T_{\alpha\beta\gamma\delta} = A\delta_{\alpha\beta}\delta_{\gamma\delta} + B\delta_{\alpha\gamma}\delta_{\beta\delta} + C\delta_{\alpha\delta}\delta_{\beta\gamma}, \tag{A.3}$$

where A, B and C are arbitrary constants.

In three dimensions, equation (A.2) leads to the following constraints to be fulfilled by constants A, B and C:

$$\begin{cases} T_{1111} = T_{2222} = T_{3333} = A + B + C \\ T_{1122} = T_{1133} = T_{2211} = T_{3311} = T_{2233} = T_{3322} = A \\ T_{1212} = T_{2323} = T_{1313} = T_{2121} = ... = B \\ T_{1221} = T_{2332} = T_{1331} = T_{2112} = ... = C \end{cases} \tag{A.4}$$

A.2 Isotropy of lattice tensors

Given a k-dimensional space and a lattice model defined by a set of b speeds, the most general form of the n-th rank tensor $L^{DkQb}_{\alpha_1\alpha_2...\alpha_n}$ that can be built on that lattice (referred to as *lattice tensor*) is given by:

$$L^{DkQb}_{\alpha_1\alpha_2...\alpha_n} = \sum_{i=0}^{b-1} e_{i\alpha_1} e_{i\alpha_2} .. e_{i\alpha_n}. \tag{A.5}$$

As stated in Chapter 3, in order to get the correct macroscopic description of the fluid state from the LB equation it is necessary choose a lattice that allows the construction of isotropic tensors of rank 2 and 4. In what follows the isotropy of these tensors for some of the most popular lattice models is checked by using the previosly reported theorem. Either single-speed (HPP and FHP-I/FHP-II) or multi-speed ($D2Q9$ and $D3Q19$)lattice models are considered. The speeds defining all these models are reported in Chapter 3.

A.2.1 D2Q4 (HPP)

The rank 2 and 4 tensors have respectively the forms:

$$\begin{cases} L_{\alpha\beta} = 2\delta_{\alpha\beta} \\ L_{\alpha\beta\gamma\delta} = 2\delta_{\alpha\beta\gamma\delta}. \end{cases} \tag{A.6}$$

$L_{\alpha\beta}$ is thus isotropic, while $L_{\alpha\beta\gamma\delta}$ not. That explains why this lattice is not suitable for getting the NS equations.

A.2.2 D2Q6/D2Q7 models (FHP-I / FHP-II)

For both these lattice models the rank 2 and 4 tensors have respectively the forms:

$$\begin{cases} L_{\alpha\beta} = 3\delta_{\alpha\beta} \\ L_{\alpha\beta\gamma\delta} = \dfrac{3}{4}\left(\delta_{\alpha\beta}\delta_{\gamma\delta} + \delta_{\alpha\gamma}\delta_{\beta\delta} + \delta_{\alpha\delta}\delta_{\beta\gamma}\right), \end{cases} \tag{A.7}$$

therefore both tensors are isotropic.

A.2.3 D2Q9 and D3Q19 models

The rank 2 lattice tensor built on $D2Q9$ and $D3Q19$ lattices are respectively given by:

$$\begin{cases} L_{\alpha\beta}^{D2Q9} = 6\delta_{\alpha\beta} \\ L_{\alpha\beta}^{D3Q19} = 10\delta_{\alpha\beta}, \end{cases} \tag{A.8}$$

therefore both of them are isotropic. To obtain rank 4 tensors the constants A, B and C in (A.2) have to be determined according to the constraints given by (A.4). For the 2 lattice models considered, that system can be respectively written as:

$$\begin{cases} A+B+C=6 \\ A=4, \quad B=4, \quad C=4 \end{cases} \tag{A.9}$$

for the $D2Q9$ and as

$$\begin{cases} A+B+C=10 \\ A=4, \quad B=4, \quad C=4 \end{cases} \tag{A.10}$$

for the $D3Q19$ lattice. In both cases rank 4 tensors are therefore not isotropic.

A.3 Getting isotropic tensors for MSL models

In order to recover rank 4 isotropic tensors for MSL models, *weighting factors* have to be introduced for the different speeds, obtaining the general form:

$$L^{DkQb-MSL}_{\alpha_1\alpha_2...\alpha_n} = \sum_{i=0}^{b-1} w_i e_{i\alpha_1} e_{i\alpha_2} .. e_{i\alpha_n}. \tag{A.11}$$

In what follows the suffix "MSL"is omitted for the sake of simplicity.

A.3.1 D2Q9 model

In this case, choosing $w_i = 1$ for speed 1 and $w_i = 1/4$ for speed $\sqrt{2}$ leads to isotropic tensors for either rank 2 or rank 4, having the following forms:

$$\begin{cases} L^{D2Q9}_{\alpha\beta} = 3\delta_{\alpha\beta} \\ L^{D2Q9}_{\alpha\beta\gamma\delta} = \delta_{\alpha\beta}\delta_{\gamma\delta} + \delta_{\alpha\gamma}\delta_{\beta\delta} + \delta_{\alpha\delta}\delta_{\beta\gamma}. \end{cases} \tag{A.12}$$

A.3.2 D3Q19 model

By choosing $w_i = 2$ for speed 1 and $w_i = 1$ for speed $\sqrt{2}$ isotropic tensors for either rank 2 or rank 4 are obtained:

$$\begin{cases} L_{\alpha\beta}^{D3Q19} = 12\delta_{\alpha\beta} \\ L_{\alpha\beta\gamma\delta}^{D3Q19} = 4\left(\delta_{\alpha\beta}\delta_{\gamma\delta} + \delta_{\alpha\gamma}\delta_{\beta\delta} + \delta_{\alpha\delta}\delta_{\beta\gamma}\right). \end{cases} \tag{A.13}$$

Appendix B

MRT D3Q19 model

This appendix presents the implementation of the MRT scheme relative to the $D3Q19$ model. The vectors defining this $\mathcal{L}$ structure are given by (3.23). The components of the basis of orthogonal vectors are:

$$\begin{cases} v_{0i} = \|\mathbf{e}_i\|^0 \\ v_{1i} = 19\|\mathbf{e}_i\|^2 - 30 \\ v_{2i} = \left(21\|\mathbf{e}_i\|^4 - 53\|\mathbf{e}_i\|^2 + 24\right)/2 \end{cases} \tag{B.1}$$

$$\begin{cases} v_{3i} = e_{ix} \\ v_{5i} = e_{iy} \\ v_{7i} = e_{iz} \end{cases} \tag{B.2}$$

$$\begin{cases} v_{4i} = \left(5\|\mathbf{e}_i\|^2 - 9\right) e_{ix} \\ v_{6i} = \left(5\|\mathbf{e}_i\|^2 - 9\right) e_{iy} \\ v_{8i} = \left(5\|\mathbf{e}_i\|^2 - 9\right) e_{iz} \end{cases} \tag{B.3}$$

$$\begin{cases} v_{9i} = 3e_{ix}^2 - \|\mathbf{e}_i\|^2 \\ v_{11i} = e_{iy}^2 - e_{iz}^2 \end{cases} \tag{B.4}$$

$$\begin{cases} v_{13i} = e_{ix}e_{iy} \\ v_{14i} = e_{iy}e_{iz} \end{cases} \tag{B.5}$$

$$\begin{cases} v_{10i} = \left(3\|\mathbf{e}_i\|^2 - 5\right)\left(3e_{ix} - \|\mathbf{e}_i\|^2\right) \\ v_{12i} = \left(3\|\mathbf{e}_i\|^2 - 5\right)\left(e_{iy}^2 - e_{iz}^2\right) \end{cases} \tag{B.6}$$

$$\begin{cases} v_{15i} = e_{ix}e_{iz} \\ v_{16i} = \left(e_{iy}^2 - e_{iz}^2\right)e_{ix} \\ v_{17i} = \left(e_{iz}^2 - e_{ix}^2\right)e_{iy} \\ v_{18i} = \left(e_{ix}^2 - e_{iy}^2\right)e_{iz} \end{cases} \tag{B.7}$$

where $i \in \{0, 1, ..18\}$. The corresponding 19 moments are given by:

$$\boldsymbol{\varrho} = (\rho, e, \varepsilon, j_x, q_x, j_y, q_y, j_z, q_z, 3p_{xx}, 3\pi_{xx}, p_{ww}, \pi_{ww}, p_{xy}, p_{yz}, p_{xz}, m_x, m_y, m_z)^T . \tag{B.8}$$

while the matrix $\mathbf{M}$ driving the transformation between the two spaces is defined as follows:

$$\begin{bmatrix}
1 & 1 & 1 & 1 & 1 & 1 & 1 & 1 & 1 & 1 & 1 & 1 & 1 & 1 & 1 & 1 & 1 & 1 & 1 \\
-30 & -11 & -11 & -11 & -11 & -11 & -11 & 8 & 8 & 8 & 8 & 8 & 8 & 8 & 8 & 8 & 8 & 8 & 8 \\
12 & -4 & -4 & -4 & -4 & -4 & -4 & 1 & 1 & 1 & 1 & 1 & 1 & 1 & 1 & 1 & 1 & 1 & 1 \\
0 & 1 & 0 & 0 & -1 & 0 & 0 & 1 & -1 & -1 & 1 & 0 & 0 & 0 & 0 & 1 & -1 & -1 & 1 \\
0 & -4 & 0 & 0 & 4 & 0 & 0 & 1 & -1 & -1 & 1 & 0 & 0 & 0 & 0 & 1 & -1 & -1 & 1 \\
0 & 0 & 1 & 0 & 0 & -1 & 0 & 1 & 1 & -1 & -1 & 1 & -1 & -1 & 1 & 0 & 0 & 0 & 0 \\
0 & 0 & -4 & 0 & 0 & 4 & 0 & 1 & 1 & -1 & -1 & 1 & -1 & -1 & 1 & 0 & 0 & 0 & 0 \\
0 & 0 & 0 & 1 & 0 & 0 & -1 & 0 & 0 & 0 & 0 & 1 & 1 & -1 & -1 & 1 & 1 & -1 & -1 \\
0 & 0 & 0 & -4 & 0 & 0 & 4 & 0 & 0 & 0 & 0 & 1 & 1 & -1 & -1 & 1 & 1 & -1 & -1 \\
0 & 2 & -1 & -1 & 2 & -1 & -1 & 1 & 1 & 1 & 1 & -2 & -2 & -2 & -2 & 1 & 1 & 1 & 1 \\
0 & -4 & 2 & 2 & -4 & 2 & 2 & 1 & 1 & 1 & 1 & -2 & -2 & -2 & -2 & 1 & 1 & 1 & 1 \\
0 & 0 & 1 & -1 & 0 & 1 & -1 & 1 & 1 & 1 & 1 & 0 & 0 & 0 & 0 & -1 & -1 & -1 & -1 \\
0 & 0 & -2 & 2 & 0 & -2 & 2 & 1 & 1 & 1 & 1 & 0 & 0 & 0 & 0 & -1 & -1 & -1 & -1 \\
0 & 0 & 0 & 0 & 0 & 0 & 0 & 1 & -1 & 1 & -1 & 0 & 0 & 0 & 0 & 0 & 0 & 0 & 0 \\
0 & 0 & 0 & 0 & 0 & 0 & 0 & 0 & 0 & 0 & 0 & 1 & -1 & 1 & -1 & 0 & 0 & 0 & 0 \\
0 & 0 & 0 & 0 & 0 & 0 & 0 & 0 & 0 & 0 & 0 & 0 & 0 & 0 & 0 & 1 & -1 & 1 & -1 \\
0 & 0 & 0 & 0 & 0 & 0 & 0 & 1 & -1 & -1 & 1 & 0 & 0 & 0 & 0 & -1 & 1 & 1 & -1 \\
0 & 0 & 0 & 0 & 0 & 0 & 0 & -1 & -1 & 1 & 1 & 1 & -1 & -1 & 1 & 0 & 0 & 0 & 0 \\
0 & 0 & 0 & 0 & 0 & 0 & 0 & 0 & 0 & 0 & 0 & -1 & -1 & 1 & 1 & 1 & 1 & -1 & -1
\end{bmatrix}$$

As for the $D2Q9$ case it is possible to recognize the density and the components of momentum and heat flux along the cartesian axes, together with the energy and energy square terms. The moments referred to the diagonal terms of symmetric traceless viscous stress tensor are $3p_{xx}$ and $p_{ww} = p_{yy} - p_{zz}$, while the off-diagonal terms are given by p_{xy}, p_{yz} and p_{xz}. Finally there are two quadratic order terms, $3\pi_{xx}$ and π_{ww}, which possess the same simmetry of the diagonal part of the traceless tensor $p_{\alpha\beta}$ and three cubic-order moments m_x, m_y and m_z which are part of third rank tensor.

The diagonal collision matrix in $\mathbb{M}_b$ is:

$$\hat{\mathbf{S}} = \mathrm{diag}\left(0, s_1, s_2, 0, s_4, 0, s_4, 0, s_4, s_9, s_{10}, s_9, s_{10}, s_{13}, s_{13}, s_{13}, s_{16}, s_{16}, s_{16}\right), \qquad \text{(B.9)}$$

The description of this implementation is complete once the equilibrium values for the non-conserved moments are defined; like for the D2Q9 case the elements of $\boldsymbol{\varrho}^{eq}$ are functions of the conserved moments and are invariant under the symmetry group of $\mathcal{L}$:

$$e^{eq} = -11\rho + \frac{19}{\rho_0}\mathbf{j}\cdot\mathbf{j} \tag{B.10a}$$

$$\varepsilon^{eq} = \omega_\varepsilon\rho + \frac{\omega_{\varepsilon j}}{\rho_0}\mathbf{j}\cdot\mathbf{j} \tag{B.10b}$$

$$q^{eq}_{x,y,z} = -\frac{2}{3}j_{x,y,z} \tag{B.10c}$$

$$p^{eq}_{xx} = \frac{1}{\rho_0}\left(3j_x^2 - \mathbf{j}\cdot\mathbf{j}\right), \quad p^{eq}_{ww} = \frac{1}{\rho_0}\left(j_y^2 - j_z^2\right) \tag{B.10d}$$

$$\pi^{eq}_{xx} = \omega_{xx}pi^{eq}_{xx}, \quad \pi^{eq}_{ww} = \omega_{xx}pi^{eq}_{ww} \tag{B.10e}$$

$$p^{eq}_{xy} = \frac{1}{\rho_0}j_xj_y, \quad p^{eq}_{yz} = \frac{1}{\rho_0}j_yj_z, \quad p^{eq}_{xz} = \frac{1}{\rho_0}j_xj_z \tag{B.10f}$$

$$m^{eq}_x = m^{eq}_y = m^{eq}_z = 0 \tag{B.10g}$$

where w_ε, $w_{\varepsilon j}$ and w_{xx} are free parameters of the model. In order to recover the corresponding SRT-LBM these values are set respectively to $w_\varepsilon = 3$, $w_{\varepsilon j} = -5.5$ and $w_{xx} = -0.5$. The bulk ζ and the kinematic ν viscosities are respectively obtained as:

$$\zeta = \frac{5 - 9c_s^2}{27}\left(\frac{1}{s_1} - \frac{1}{2}\right) = \frac{2}{9}\left(\frac{1}{s_1} - \frac{1}{2}\right) \tag{B.11}$$

$$\nu = \frac{1}{3}\left(\frac{1}{s_9} - \frac{1}{2}\right) = \frac{1}{3}\left(\frac{1}{s_{13}} - \frac{1}{2}\right). \tag{B.12}$$

In order to reduce the density fluctuations that afflict LBM simulations of incompressible flows a different formulation of the f_i^{eq} was proposed in [45] for the SRT-LBM. The MRT-counterpart of these scheme requires a different formulation of the $\boldsymbol{\varrho}^{eq}$ vector:

$$e^{eq} = -11\delta\rho + \frac{19}{\rho_0}\mathbf{j}\cdot\mathbf{j} \tag{B.13a}$$

$$\varepsilon^{eq} = \omega_\varepsilon\delta\rho + \frac{\omega_{\varepsilon j}}{\rho_0}\mathbf{j}\cdot\mathbf{j} \tag{B.13b}$$

$$q^{eq}_{x,y,z} = -\frac{2}{3}j_{x,y,z} \tag{B.13c}$$

$$p^{eq}_{xx} = \frac{1}{\rho_0}\left(3j_x^2 - \mathbf{j}\cdot\mathbf{j}\right), \quad p^{eq}_{ww} = \frac{1}{\rho_0}\left(j_y^2 - j_z^2\right) \tag{B.13d}$$

$$\pi^{eq}_{xx} = \omega_{xx}pi^{eq}_{xx}, \quad \pi^{eq}_{ww} = \omega_{xx}pi^{eq}_{ww} \tag{B.13e}$$

$$p^{eq}_{xy} = \frac{1}{\rho_0}j_xj_y, \quad p^{eq}_{yz} = \frac{1}{\rho_0}j_yj_z, \quad p^{eq}_{xz} = \frac{1}{\rho_0}j_xj_z \tag{B.13f}$$

$$m^{eq}_x = m^{eq}_y = m^{eq}_z = 0 \tag{B.13g}$$

where ρ_0 is the average density, usually set to unity in LU, and $\delta\rho$ is the density fluctuation. The stability of the MRT scheme can be furtherly improved via an optimal choice of the adjustable parameters appearing in (B.10a) and (B.13a); in [82] a local stability analysis for a system with fully periodical boundaries gave the following set of values:

$$w_{xx} = 0 \quad w_\varepsilon = 0 \quad w_{\varepsilon j} = -\frac{475}{73} \tag{B.14a}$$

$$s_1 = 1.19 \quad s_2 = s_{10} = 1.4 \quad s_4 = 1.2 \quad s_{16} = 1.98 \tag{B.14b}$$

Appendix C

The Chapman-Enskog expansion

In this section the complete derivation of the NS equations via a multiscale expansion will be given. For the sake of simplicity the starting equation will be the BGK model with SRT, (3.4). Besides the lattice model is $D2Q9$. Analogous procedures can be followed for MRT model ([] or []), as well as SC models for both single and multi-component cases ([63]).
The starting point will be equation (3.4), here rewritten as:

$$f_i\left(\mathbf{x}+\mathbf{e}_i\Delta t, t+\Delta t\right) = (1-\omega) f_i\left(\mathbf{x}, t\right) + \omega f_i^{(0)}\left(\mathbf{x}, t\right). \tag{B.1}$$

where $\omega = \tau^{-1}$ and $f^{(0)} = f^{eq}$. The first step is to introduce two time and one spactial scale as follows:

$$\partial_t = \varepsilon\partial_{t_1} + \varepsilon^2\partial_{t_2} \tag{B.2a}$$

$$\partial_\alpha = \varepsilon\partial_{\alpha_1}. \tag{B.2b}$$

Once introduced these scales, the generic distribution function around can be expnded around its equilibrium value:

$$f_i = f_i^{(0)} + \varepsilon f_i^{(1)} + \varepsilon^2 f_i^{(2)} + \mathcal{O}(\varepsilon^3), \tag{B.3}$$

As seen in chapter 3, the first and second moment of equilibrium PDF have to

correspond to local density and momentum: therefore, the following constraints on equilibrium and non-equilibrium parts of distribution functions hold:

$$\sum_i f_i^{(0)} = \rho \tag{B.4a}$$

$$\sum_i f_i^{(0)} e_{i\alpha} = \rho u_\alpha \tag{B.4b}$$

$$\sum_i f_i^{(k)} = 0 \quad k = 1, 2, \ldots \tag{B.4c}$$

$$\sum_i f_i^{(k)} e_i = 0 \quad k = 1, 2, \ldots \tag{B.4d}$$

The left hand side of (B.1) can be Taylor-expanded up to second order terms ($\Delta \mathbf{x}_i = \mathbf{e}_i \Delta t$):

$$\begin{aligned} f_i\left(\mathbf{x} + \mathbf{e}_i \Delta t, t + \Delta t\right) = f_i\left(\mathbf{x}, t\right) + \Delta t \partial_t f_i + \Delta t e_{i\alpha} \partial_\alpha f_i \\ + \frac{(\Delta t)^2}{2} \left[\partial_t \partial_t f_i + 2 e_{i\alpha} \partial_t \partial_\alpha f_i + e_{i\alpha} e_{i\beta} \partial_\alpha \partial_\beta f_i\right] + \mathcal{O}\left(\partial^3 f_i\right). \end{aligned} \tag{B.5}$$

Substituing these expansion into (B.1) leads to:

$$\begin{aligned} 0 \quad = \quad & f_i\left(\mathbf{x}, t\right) + \Delta t \partial_t f_i + \Delta t e_{i\gamma} \partial_\gamma f_i \\ & + \frac{(\Delta t)^2}{2} \left[\partial_t \partial_t f_i + 2 e_{i\alpha} \partial_t \partial_\alpha f_i + e_{i\alpha} e_{i\beta} \partial_\alpha \partial_\beta f_i\right] \\ & + \mathcal{O}\left(\partial^3 f_i\right) - f_i\left(\mathbf{x}, t\right) + \omega \left(f_i\left(\mathbf{x}, t\right) - f_i^{(0)}\left(\mathbf{x}, t\right)\right) \\ & = \varepsilon \Delta t \left[\partial_{t_1} f_i^{(0)} + e_{i\gamma} \partial_{\gamma_1} f_i^{(0)}\right] \\ & + \varepsilon^2 \Delta t \left[\partial_{t_1} f_i^{(1)} + \partial_{t_2} f_i^{(0)} + e_{i\gamma} \partial_{\gamma_1} f_i^{(1)}\right] \\ & + \varepsilon^2 \frac{(\Delta t)^2}{2} \left[\partial_{t_1} \partial_{t_1} f_i^{(0)} + 2 e_{i\gamma} \partial_{t_1} \partial_{\gamma_1} f_i^{(0)} + e_{i\beta} e_{i\gamma} \partial_{\beta_1} \partial_{\gamma_1} f_i^{(0)}\right] \\ & + \varepsilon \omega f_i^{(1)} + \varepsilon^2 \omega f_i^{(2)} + \mathcal{O}(\varepsilon^3) \end{aligned} \tag{B.6}$$

Rearraging (B.6) in terms of orders of ε yields:

$$0 = \varepsilon E_i^{(0)} + \varepsilon^2 E_i^{(1)} + \mathcal{O}(\varepsilon^3), \tag{B.7}$$

where

$$E_i^{(0)} = \partial_{t_1} f_i^{(0)} + e_{i\gamma}\partial_{\gamma_1} f_i^{(0)} + \frac{\omega}{\Delta t} f_i^{(1)} \tag{B.8a}$$

$$E_i^{(1)} = \partial_{t_1} f_i^{(1)} + \partial_{t_2} f_i^{(0)} + e_{i\gamma}\partial_{\gamma_1} f_i^{(1)} + \Delta t \left[\frac{1}{2}\partial_{t_1}\partial_{t_1} f_i^{(0)} + e_{i\gamma}\partial_{t_1}\partial_{\gamma_1} f_i^{(0)} + \frac{1}{2} e_{i\beta} e_{i\gamma}\partial_{\beta_1}\partial_{\gamma_1} f_i^{(0)}\right] + \frac{\omega}{\Delta t} f_i^{(2)} \tag{B.8b}$$

The next step consists in calculating the zero-th and first lattice moments of the terms $E_i^{(0)}$ and $E_i^{(0)}$ in order to get Euler and NS equations.

C.1 First order terms in ε

From (B.8a) and using the relation $\sum_i e_{i\alpha} e_{i\beta} = 6c^2\delta_{\alpha\beta}$, togheter with (B.4a)-(B.4d) we have:

$$\sum_i E_i^{(0)} = \partial_{t_1}\rho + \partial_{\gamma_1} j_\gamma \tag{B.9a}$$

$$\sum_i E_i^{(0)} e_{i\alpha} = \partial_{t_1} j_\alpha + \partial_{\beta_1}\Pi_{\alpha\beta}^{(0)}. \tag{B.9b}$$

The inviscid momentum flux tensor is given by:

C.2 Second order terms

Appendix D

List of contributions

The research carried out during this PhD project generated one published paper in a peer-reviewed journal and two published conference proceedings. These contributions are listed here in chronological order:

- E. Monaco, K. H. Luo and R. S. Qin, "Lattice Boltzmann simulations for microfluidic and mesoscale phenomena". New trends in fluid mechanics research: Proceedings of the Fifth International Conference in Fluid Mechanics, Shanghai, August 2007. Tsinghua University and Springer.

- K. H. Luo, J. Xia and E. Monaco, "Multiscale modeling of multiphase flows with complex interactions". Journal of Multiscale Modeling **1** (1), 2009.

- E. Monaco, K. H. Luo and G. Brenner, "Lattice Boltzmann simulations of binary droplet collisions by a multiphase multiple relaxation time model". Proceedings of Parallel CFD conference 2008 (*in press*).

The results described in this thesis have been also presented in several meetings and conferencies. The most important are:

- E. Monaco, K. H. Luo and R. S. Qin, "A study on micromixing enhancement by optimization of the obstacles layout in a T-Shaped micromixer using the lattice Boltzmann method". Poster presentation at "Micro and Nano-scale flows: Advancing the engineering Science and Design". 7-8 December 2006. University of Strathclyde, Glasgow

- E. Monaco, K. H. Luo and R. S. Qin, "Lattice Boltzmann Simulation of Carbon Dioxide Multiphase Flow in Microchannels". Oral presentation at "ICMMES, International Conference on Mesoscopic Methods in Engineering and Sciences, 2007" conference. 16-20/ July 2007. München, Germany.

- E. Monaco, K. H. Luo and G. Brenner, "Lattice Boltzmann simulations of binary droplet collisions by a multiphase multiple relaxation time model". Oral presentation at "Parallel CFD conference 2008". 19-22 May 2008. Lyon, France.

- E. Monaco, K. H. Luo and G. Brenner "Lattice Boltzmann simulations of binary droplet collisions by a multiphase multiple relaxation time model". Oral presentation at "ICMMES, International Conference on Mesoscopic Methods in Engineering and Sciences, 2008". 16-20 June 2008. Amsterdam, The Netherlands.

- E. Monaco, K. H. Luo and G. Brenner "Numerical investigation on the efficiency of a passive micromixer with the Lattice Boltzmann method". Accepted for oral presentation at "ECCOMAS CFD 2010, The fifth European Conference on Computational Fluid Dynamics". 14-17 June 2010. Lisbon, Portugal.

Bibliography

[1] L. S. Luo. *Lattice Gas Automata and Lattice Boltzmann Equations for Two-Dimensional Hydrodynamics*. PhD thesis, Georgia Instute of Technology, 1992.

[2] M. Shapira and S. Haber. Low reynolds motion of droplet in shear flow including wall effects. *Int. J. Multiphase Flows*, 16, 1990.

[3] H. Wang, P. Iovenitti, E. Harvey, and S. Masood. Optimizing the layout of obstacles for enhanced mixing in microchannels. *Smart Mat. Struct.*, 11:662–667, 2002.

[4] M Cheng and K. C. Hung. Vortex structure of steady flow in a rectangular cavity. *Comp. Fluids*, 35:1046–1062, 2006.

[5] D. J. Holdych, J. G. Georgiadis, and R. O. Buckius. Hydrodynamic instabilities of near critical CO_2 flow in microchannels: Lattice Boltzmann simulation. *Phys. Fluids*, 16(5), 2004.

[6] J. Pettersen. Two-phase flow patterns in microchannel vaporization of CO_2 at near-critical pressure. *Heat Transfer Eng.*, 35(52), 2004.

[7] J. Qian and C.K. Law. Regimes of coalescence and phase separation in droplet collision. *J. Fluid. Mech.*, 331:59–80, 1997.

[8] F. Mashayek, N. Ashgriz, W. J. Minkowycz, and B. Shobotorban. Coalescence collision of liquid drops. *Int. J. Heat Mass Transf.*, 46:77–89, 2003.

[9] P. Yuan and L. Schaefer. Equations of state in a lattice Boltzmann model. *Phys. Fluids*, 18, 2006.

[10] R. S. Qin. Mesoscopic interparticle potentials in the lattice Boltzmann equation for multiphase flows. *Phys. Rev. E*, 73, 2006.

[11] O. Penrose. *Foundations of Statistical Mechanics*. Pergamon Press, first edition, 1970.

[12] J.P. Rivet and J.P. Boon. *Lattice Gas Hydrodynamics*. Cambridge University Press, first edition, 2001.

[13] C. Cercignani. *Mathematical methods in Kinetic theory*. London, Mc Millan, 1969.

[14] P. L. Bhatnagar, E. P. Gross, and M. Krook. A model for collision processes in gases. i. small amplitude processes in charged and neutral one-component systems. *Phys. Rev.*, 94(3):511–525, 1954.

[15] U. Frish, B. Hasslacher, and Y. Pomeau. Lattice-gas automata for the navier-stokes equations. *Phys. Rev. Lett.*, 56:1505–1508, 1986.

[16] S. Succi. *Lattice Boltzmann equation for fluid dynamic and beyond*. Oxford University Press, first edition, 2001.

[17] R. McNamara and G. Zanetti. Use of the Boltzmann equation to simulate lattice-gas automata. *Phys. Rev. Lett*, 61(20):2332–2335, 1988.

[18] D. H. Rothman and S. Zaleski. *Lattice Gas Cellular Automata*. Cambridge University Press, first edition, 1997.

[19] F. Higuera and J. Jimenez. Boltzmann approach to lattice gas simulations. *Europhys. Lett.*, 9:663, 1989.

[20] F. Higuera, S. Succi, and R. Benzi. Lattice gas hydrodynamics with enhanced collisions. *Europhys. Lett.*, 9:345, 1989.

[21] Y.H. Quian, D. d'Humieres, and P. Lallemand. Lattice bgk models for the navier-stokes equation. *Europhys. Lett.*, 17:479–484, 1992.

[22] X. He and L.S. Luo. Theory of lattice Boltzmann equation: from the Boltzmann equation to the lattice Boltzmann equation. *Phys. Rev. E*, 56:6811–6817, 1997.

[23] S. Succi, I. Karlin, and H. Chen. *Colloquium*: Role of the h theorem in lattice Boltzmann hydrodynamic simulations. *Rev. Mod. Phys*, 74:1203–1220, 2002.

[24] A. J. Chorin. A numerical method for solving incompressible viscous flow problems. *Int. J. Mod. Phys. C*, 135:118–125, 1997. Recent edition.

[25] R. R. Nourgaliev, T. N. Dinh, T. G. Theofanous, and D. Joseph. The lattice Boltzmann equation method: theoretical interpretation, numerics and implications. *Int. J. of Mult. Flow*, 29(1):117–169, 2003.

[26] J. D. Sterling and S. Chen. Stability analysis of lattice Boltzmann methods. *J. Comp. Phys.*, 123(196–206), 1996.

[27] S. Chen F. J. Alexander and J. D. Sterling. Lattice Boltzmann thermohydrodynamics. *Phys. Rev. E*, 47, 1993.

[28] A. Wagner. An H-theorem for the lattice Boltzmann approach to hydrodynamics. *Europhys. Lett.*, 44(2):144–149, 1998.

[29] S. Ansumali, I. V. Karlin, and H. C. Öttinger. Minimal entropic kinetic models for hydrodynamics. *Europhys. Lett.*, 63(6):798–804, 2003.

[30] S. Ansumali and I. V. Karlin. Entropic Lattice Boltzmann simulation of the flow past square cylinder. *Int. J. Mod. Phys. C*, 15(3):435–445, 2004.

[31] S. Ansumali and I. V. Karlin. Entropy function approach to the Lattice Boltzmann method. *J. Stat. Phys.*, 107(1/2):291–308, 2002.

[32] X. He, X. Shan, and G.D. Doolen. A discrete lattice Boltzmann model for non-ideal gases. *Phis. Rev. E*, 57, 1998.

[33] J. M. Buick and C. A. Greated. Gravity in a lattice Boltzmann model. *Phys. Rev. E*, 61(5):5307–5320, 2000.

[34] A. Kupershtokh. Calculations of the action of electric forces in the lattice Boltzmann equation method using the difference of equilibrium distribution functions. In *Proceedings of the seventh conference on modern problems of Electrophysics and Electrodynamics of liquids, St. Petersburg University, St. Petersburg, Russia*, 2003.

[35] A.L. Kupershtokh and D.A. Medvedev. Lattice Boltzmann equation method in electrodynamic problems. *J. Elstat.*, 64(581–585), 2006.

[36] J. Latt. *Hydrodynamic limits of lattice Boltzmann equations*. PhD thesis, University of Geneva, 2007.

[37] P. A. Skordos. Initial and boundary conditions for the lattice Boltzmann method. *Phys. Rev. E*, 48(6):4823–4842, 1993.

[38] S. Hou, Q. Zou, S. Chen, G. Doolen, and A. Cogley. Simulation of cavity flow by the lattice Boltzmann method. *J. Comput. Phys.*, 118:329–347, 1995.

[39] J. S. Wu and Y. L. Shao. Simulation of lid-driven cavity flows by parallel lattice Boltzmann method using multiple relaxation time scheme. *Int. J. Numer. Meth. Fluids*, 46:921–937, 2004.

[40] I. Halliday, L. A. Hammond, and C. M. Care. Enhanced closure scheme for lattice Boltzmann equation hydrodynamics. *J. Phys. A: Math. Gen.*, 35:157–166, 2002.

[41] Q. Zou and X. He. On pressure and velocity flow boundary conditions and bounceback for the lattice Boltzmann bgk model. *Phys. Fluids*, 9:1591–1598, 1997.

[42] Z. Guo, Z. Chu-Guang, and B. Shi. Non-equilibrium extrapolation method for velocity and pressure boundary conditions in the lattice Boltzmann method. *Chin. Phys.*, 11(4):366–374, 2002.

[43] C. Zheng Z. Guo and B. Shi. An extrapolation method for boundary conditions in lattice Boltzmann method. *Phys. Fluids*, 14(6), 2002.

[44] X. He, Q. Zou, L.S. Luo, and M. Dembo. Analytic solutions and analysis of non-slip boundary conditions for the lattice Boltzmann bgk model. *J. Comput. Phys.*, 87(1/2):115–136, 1997.

[45] X. He and L.S. Luo. Lattice Boltzmann model for the incompressible navier stokes equation. *J. Stat. Phys.*, 88(1/2):115–136, 1997.

[46] P. N. Shankar and M. D. Deshpande. Fluid mechanics in the driven cavity. *Ann. Rev. Fluid Mech.*, 32:93–136, 2000.

[47] U. Ghia, K.N. Ghia, and C.Y. Shin. High-re solutions for incompressible flow using the navier-stokes equations and a multigrid method. *J. Comput. Phys.*, 48:387–411, 1982.

[48] J.H. Ferziger and M. Peric. *Computational Methods for Fluid Dynamics*. Springer, New York, first edition, 1999.

[49] Y. Lai, C-L Lin, and J. Huang. Accuracy and efficiency study of lattice Boltzmann method for steady-state flow simulations. *Num. Heat Transf, Part B*, 39:23–41, 2001.

[50] R. Mei, L.S. Luo, and W. Shyy. An accurate curved boundary treatment in the lattice Boltzmann method. *J. Comput. Phys.*, 155:307–330, 1999.

[51] D.O. Martinez, W.H. Matthaeus, S. Chen, and D.C. Montgomery. Comparson of spectral methods and lattice Boltzmann simulations of two-dimentional hydrodynamics. *Phys. Fluids*, 6(3):1285, 1994.

[52] X.W. Shan and H.D. Chen. Lattice Boltzmann model for simulating flows with multiple phases and components. *Phys. Rev. E*, 47:1815, 1993.

[53] X.W. Shan and H.D. Chen. Diffusion in a multicomponent lattice-Boltzmann equation model. *Phys. Rev. E*, 54(4):3614–3620, 1996.

[54] H. B. Callen. *Thermodynamics and an introduction to thermostatistics*. John Wiley & Sons, second edition, 1985.

[55] X.W. Shan and H.D. Chen. Simulation of non-ideal gases and liquid-gas phase transition by the lattice Boltzmann equation. *Phys. Rev. E*, 49:2941–2948, 1994.

[56] F. Wolf, L. O. E. dos Santos, and P. Philippi. Fluid interfaces in phase transition problems: Lattice Boltzmann method. In *18th International Congress of Mechanical Engineering*. COBEM, 2005.

[57] T. Lee and C. L. Lin. A stable discretization of the lattice Boltzmann equation for simulation of incompressible two-phase flows at high density ratio. *J. Comp. Phys.*, 206:16–47, 2005.

[58] N. Martys and H.D. Chen. Simulation of multicomponent fluids in complex three-dimensional geometries by the lattice Boltzmann method. *Phys. Rev. E*, 53:743–750, 1996.

[59] R. Benzi, L. Biferale, M. Sbragaglia, S. Succi, and F. Toschi. Mesoscopic modeling of a two-phase flow in the presence of boundaries: The contact angle. *Phys. Rev. E*, 74, 2006.

[60] H. Huand, D. Thorne, M. G. Shaap, and M. C. Sukop. Proposed approximation for contact angle in shan-and-chen-type multicomponent multiphase lattice Boltzmann models. *Phys. Rev. E*, 76, 2007.

[61] M. C. Sukop and Jr. D. T. Thorne. *Lattice Boltzmann modeling, an introduction for scientists and engineers*. Springer, 2005.

[62] G. Máyer, Házi G, J. Páles, A. Imre, B. Fischer, and T. Kraska. On the system size of lattice Boltzmann simulations. *Int. J. Mod. Phys. C*, 15(8):1049–1060, 2004.

[63] J. Chin and P. Coveney. Lattice Boltzmann study of spinodal decomposition in two dimensions. *Phys. Rev. E*, 66, 2002.

[64] H. A. Stone, A. D. Stroock, and A. Ajdari. Engineering flows in small devices: Microfluidics toward a lab-on-a-chip. *Ann. Rev. Fluid Mech*, 36:381–411, 2004.

[65] V. Sibillo, G. Pasquariello, M. Simeone, V. Cristini, and S. Guido. Drop deformation in microconfined shear flow. *Phys. Rev. Lett.*, 97, 2006.

[66] Y. Y. Renardy and V. Cristini. Effect of inertia on drop breakup under shear. *Phys. Fluids*, 13(1):7–13, 2001.

[67] A. Einstein. On the motion of small particles suspended in liquids. *Ann. Phys. Lpz.*, 17:549–560, 1905.

[68] E. M. Purcell. Life at low reynolds number. *Am. J. Phys.*, 45:3–11, 1977.

[69] V. Hessel, H. Löwe, and F. Schönfeld. Micromixers-a review on passive and active mixing principle. *Chem. Eng. Sci.*, 60:2478–2501, 2005.

[70] N. L. Jeon, S. K. W. Dertinger, D. T. Chiu, I. S. Choi, A. D. Strook, and G. M. Whitesides. Generation of solution and surface gradients using microfluidic systems. *Langmuir*, 16:8311–8316, 2000.

[71] D. Gobby, P. Angeli, and A. Gavriilidis. Mixing characteristics on t-type microfluidic mixers. *J. Micromech. Microeng.*, 11:126–132, 2001.

[72] E. G. Flekkøy. Lattice bgk models for miscible fluids. *Phys. Rev. E*, 47:4247–4258, 1993.

[73] M. Sbragaglia, R. Benzi, L. Biferale, S. Succi, K. Sugiyama, and F. Toschi. Generalized lattice Boltzmann method with multirange pseudopotential. *Phys. Rev. E*, 75, 2007.

[74] A.K. Gunstensen, D.H. Rothman, S.Zaleski, and G. Zanetti. Lattice Boltzmann model of immiscible fluids. *Phys. Rev. A*, 43:4320–4327, 1991.

[75] D. Grunau, S. Chen, and K. Eggert. A lattice Boltzmann model for multiphase flows. *Phys. Flu. A*, 5:2557, 1993.

[76] M.R. Swift, W.R. Osborn, and J.M. Yeomans. Lattice Boltzmann simulation of nonideal fluids. *Phys. Rev. Lett.*, 75(5):830–834, 1995.

[77] M.R. Swift, E. Orlandini, W.R. Osborn, and J.M. Yeomans. Lattice Boltzmann simulation of liquid-gas and binary fluid systems. *Phys. Rev. E*, 54(5):5041–5051, 1996.

[78] A. Lamura, G. Gonnella, and J. M. Yeomans. A lattice Boltzmann model of ternary fluid mixtures. *Europhys. Lett.*, 99:314–320, 1999.

[79] A. J. C. Ladd. Numerical simulation of particulate suspensions via a discretized Boltzmann equation, part i. theoretical foundation. *J. Fluid Mech.*, 271:285–310, 1994.

[80] A. J. C. Ladd. Numerical simulation of particulate suspensions via a discretized Boltzmann equation, part ii. numerical results. *J. Fluid Mech.*, 271:285–310, 1994.

[81] N. Q. Nguyen and A. J. C. Ladd. Lubrification corrections for lattice-Boltzmann simulations of particle suspensions. *Phys. Rev. E*, 66, 2002.

[82] P. Lallemand and L.S. Luo. Theory of the lattice Boltzmann method: Dispersion, dissipation, isotropy, galilean invariance and stability. *Phys. Rev. E*, 61(6):6546–6562, 2000.

[83] D. D'Humieres, I. Guinzburg, M. Krafczyk, P. Lallemand, and L.S. Luo. Multiple relaxation time lattice Boltzmann models in three dimensions. *Phil. Trans. R. Soc. Lond. A*, 360:437–451, 2002.

[84] I. Ginzbourg and P. M. Adler. Boundary flow conditions analysis for the three-dimensional lattice Boltzmann model. *J. Physique II France*, 4:191–214, 1994.

[85] H. Yu. *Lattice Boltzmann equation simulations of turbulence, mixing and combustion*. PhD thesis, Texas A&M University, 2004.

[86] Z. H. Chau, B. C. Shi, and L. Zheng. Simulating high re number flows in 2d lid-driven cavity by multiple-relaxation-time lattice-Boltzmann method. *Chin. Phys.*, 15(8):1855–1863, 2006.

[87] M. Dembo X. He, L. S. Luo. Some progress in lattice Boltzmann method. part i: Nonuniform mesh grids. *J. Comput. Phys.*, 129:357–363, 1996.

[88] M. Cheng and K. C. Hung. Lattice Boltzmann method on non-uniform mesh. *Int. J. Comput. Eng Sci.*, 5:291–302, 2004.

[89] Irina Ginzburg. Generic boundary conditions for lattice boltzmann models and their application to advection and anisotropic dispersion equations. *Advances in Water Resources*, 28(11):1196 – 1216, 2005.

[90] Irina Ginzburg. Equilibrium-type and link-type lattice boltzmann models for generic advection and anisotropic-dispersion equation. *Advances in Water Resources*, 28(11):1171 – 1195, 2005.

[91] P. Asinari and I. V. Karlin. Generalized Maxwell state and H-theorem for the lattice Boltzmann method. *Phys. Rev. E*, 79(3), 2009.

[92] A. Márkus and G. Házi. Determination of the pseudopotential gradient in multiphase lattice Boltzmann models. *Phys. Fluids*, 20, 2008.

[93] N. Carnahan and K. Starling. Equation of state for non attracting rigid spheres. *J. Chem. Phys.*, 51(2):635–636, 1969.

[94] T. Lee and P. Fischer. Eliminating parasitic currents in the lattice Boltzmann equation method for nonideal gases. *Phys. Rev. E*, 74, 2006.

[95] D. J. Holdych, D. Rovas, J. G. Georgiadis, and R. O. Buckius. An improved hydrodynamics formulation for multiphase flow lattice-Boltzmann models. *Int. J. Mod. Phys. C*, 9(8):1393–1404, 1998.

[96] E. Monaco, K. H. Luo, and R. S. Qin. Lattice Boltzmann simulations for microfluidic and mesoscale phenomena. In *Proceedings of the Fifth International Conference in Fluid Mechanics*, New trends in fluid mechanics research. Tsinghua University and Springer, August 2007.

[97] X. Shan. Analysis and reduction of spurious currents in a class of multiphase lattice Boltzmann models. *Phys. Rev. E*, 73, 2006.

[98] P.R. Brazier-Smith, S.G. Jennings, and J. Latham. The interaction of falling water drops: coalescence. *Proc. R. Soc. Lond. A*, 326:393–408, 1972.

[99] N. Ashgriz and Y. Poo. Coalescence and separation in binary collisions of liquid drops. *J. Fluid. Mech.*, 221:183–204, 1990.

[100] Y.J. Jiang, A. Umemura, and C.K. Law. An experimental investigation on the collision behaviour of hydrocarbon droplets. *J. Fluid. Mech.*, 234:171–190, 1992.

[101] J. P. Estrade, H. Carentz, G. Lavergne, and Y. Biscos. Experimental investigation of dynamic binary collision of ethanol droplests-a model for droplet coalescence and bouncing. *J. Heat Fluid Flow*, 20:486–491, 1999.

[102] G. Foote. The water drop rebound problem: Dynamics of collision. *J. Atmos. Sci.*, 32, 1975.

[103] Y.J. Jan M. Nobari and G. Tryggvason. Head-on collision of drops-a numerical investigation. *Phys. Fluids*, 29, 1996.

[104] M. Nobari and G. Tryggvason. Numerical simulation of three-dimensional drop collision. *AIAA J.*, 34:750–755, 1996.

[105] B. Lafaurie, C. Nardone, R. Scardovelli, S. Zaleski, and G. Zanetti. Modeling merging and fragmentation in multiphase flows with surfer. *J. Comput. Phys.*, 113(1):134–147, 1994.

[106] N. Nikolopoulos, K.-S. Nikas, and G. Bergeles. A numerical investigation of central binary collision of droplets. *Computers & Fluids*, 38(6):1191 – 1202, 2009.

[107] Y. Pan and K. Suga. Numerical simulations of binary liquid droplet collision. *Phys. Fluids*, 17, 2005.

[108] M. Schelkle and A. Frohn. Three-dimensional lattice Boltzmann simulations of binary collisions between equal droplets. *J. Aerosol Sci*, 26:145–146, 1995.

[109] T. Inamuro, S. Tajima, and F. Ogino. Lattice Boltzmann simulation of droplet collision dynamics. *Int. J. Heat Mass Transfer*, 47(21):4649–4657, 2004.

[110] B. Sakakibara and T. Inamuro. Lattice Boltzmann simulation of collision dynamics of unequal-size droplets. *Int. J. Heat Mass Transfer*, 51:3207–3216, 2008.

[111] K.N. Premnath and J. Abraham. Simulations of binary drop collisions with a multiple-relaxation-time lattice-Boltzmann model. *Phys. Fluids*, 17, 2005.

[112] K. H. Luo, J. Xia, and E. Monaco. Multiscale modeling of multiphase flows with complex interactions. *J. Multiscale Model.*, 1(1):125–156, 2009.

[113] J. Eggers, J. R. Lister, and H. A. Stone. Coalescence collision of liquid drops. *J. Fluid Mech*, 401:293–310, 1999.

[114] P.Yuan. *Thermal lattice-Boltzmann two-phase flow model for fluid dynamics*. PhD thesis, School of Engineering, University of Pittsburg, 2005.

[115] M. De Menech, P. Garteski, F. Jousse, and A. H. Stone. Transition from squeezing to dripping in a microfluidic t-shaped junction. *J. Fluid Mech.*, 595:141–161, 2008.

[116] E.R. Choban, L.J. Markowski, A. Wieckowski, and P.J.A. Kenis. Microfluidic fuel cell based on laminar flow. *J. Power Sources*, 128:54–60, 2004.

[117] E.R. Choban, J.S. Spendelow, L. Gancs, A. Wieckowski, and P.J.A. Kenis. Membraneless laminar flow-based micro fuel cells operating in alkaline, acidic, and acidic/alkaline media. *Electrochimica Acta*, 50:5390–5398, 2005.

[118] X. He and N. Li. Lattice Boltzmann simulations of electrochemical systems. *Computer Physics Communications*, 129:158–166, 2000.

[119] S. Succi, G. Smith, and E. Kaxiras. Lattice Boltzmann simulation of reactive microflows over catalytic surfaces. *Jou. Stat. Phys.*, 107(112):343–366, 2002.

[120] H. Jeffries. *Cartesian Tensors*. Cambridge University Press, first edition, 1965.